

Timing and Evolution of Structures within the Southeastern Greater Caucasus and Kura Fold-Thrust Belt from Multiproxy Sediment Provenance Records

Adam M. Forte¹ (aforte8@lsu.edu), Eric S. Cowgill² (escowgill@ucdavis.edu), Dawn Y. Sumner² (dysumner@ucdavis.edu) Dominique I. Garello¹ (dgarello1@lsu.edu), Nathan A. Niemi³ (naniemi@umich.edu), K. Colton Fowler¹ (kfowl11@lsu.edu)

¹Department of Geology & Geophysics, Louisiana State University, Baton Rouge, LA, USA

²Department of Earth and Planetary Sciences, University of California, Davis, CA, USA

³Department of Earth & Environmental Sciences, University of Michigan, Ann Arbor, MI, USA

This paper is a revised version of a preprint submitted to EarthArXiv. This paper has been re-submitted to Geosphere for peer review and has gone through two rounds of revision.

1 **Timing and Evolution of Structures within the Southeastern Greater Caucasus and Kura Fold-**
2 **Thrust Belt from Multiproxy Sediment Provenance Records**

3

4 Adam M. Forte¹, Eric S. Cowgill², Dawn Y. Sumner², Dominique I. Garello¹, Nathan A. Niemi³, K.
5 Colton Fowler¹

6

7 ¹Department of Geology & Geophysics, Louisiana State University, Baton Rouge, LA, USA

8 ²Department of Earth and Planetary Sciences, University of California, Davis, CA, USA

9 ³Department of Earth & Environmental Sciences, University of Michigan, Ann Arbor, MI, USA

10

11 **ABSTRACT**

12 The Greater Caucasus (GC) mountains are the locus of post-Pliocene shortening within
13 the north central Arabia-Eurasia collision. Although recent low-temperature thermochronology
14 constrains the timing of orogen formation, the evolution of major structures remains enigmatic
15 - particularly regarding the internal kinematics within this young orogen and the associated
16 Kura Fold-Thrust Belt (KFTB), which flanks its southeastern margin. Here we use a multiproxy
17 provenance analysis to investigate the tectonic history of both the southeastern GC and KFTB
18 by presenting new data from a suite of sandstone samples from the KFTB, including sandstone
19 petrography, whole-rock geochemistry, and detrital zircon (DZ) U-Pb geochronology. To define
20 source terranes for these sediments, we integrate additional new whole-rock geochemical
21 analyses with published DZ results and geological mapping. Our analysis reveals an apparent
22 discrepancy in up-section changes in provenance from the different methods. Sandstone

23 petrography and geochemistry both indicate a systematic up-section evolution from a
24 volcanic/volcaniclastic source, presently exposed as a thin strip along the southeastern GC, to
25 what appears similar to an interior GC source. Contrastingly, DZ geochronology suggests less
26 up-section change. We interpret this apparent discrepancy to reflect the onset of sediment
27 recycling within the KFTB, with the exhumation, weathering, and erosion of early thrust sheets
28 in the KFTB resulting in the selective weathering of unstable mineral species that define the
29 volcaniclastic source, but left DZ signatures unmodified. Using the timing of sediment recycling
30 as a proxy for structural initiation of the central KFTB implies that the thrust belt initiated nearly
31 synchronously along-strike at ~2.0-2.2 Ma.

32

33 **1. INTRODUCTION AND MOTIVATION**

34 The provenance histories of siliciclastic sedimentary rocks in foreland basins often
35 provide a robust, and in some cases, singular record of the past structural and kinematic history
36 of the flanking orogenic system (e.g., Sinclair, 1997; DeCelles et al., 1998; Lawton et al., 2010;
37 Nagel et al., 2014; Leary et al., 2016; Capaldi et al., 2020). In detail, shifts in sediment
38 provenance recorded in forelands can elucidate the order of initiation, direction of propagation,
39 and style of structures within a mountain range, thus providing crucial constraints for tectonic
40 models of orogen evolution (e.g., Carrapa et al., 2006; Panaiotu et al., 2007; Bande et al., 2012;
41 Laskowski et al., 2013; Garber et al., 2020). The resulting information on both absolute and
42 relative timing of structures can prove especially important in evaluating the extent to which
43 particular mountain ranges obey the expected behavior of critically tapered orogenic wedges
44 (e.g., Davis et al., 1983; Dahlen and Suppe, 1988; Dahlen, 1990). For example, critical wedge

45 theory suggests a direct relationship between the efficiency of climate and the width of
46 mountain ranges (e.g., Stolar et al., 2006; Whipple and Meade, 2006; Roe et al., 2008), where
47 changes in width would in part be reflected in the order of initiation of structures and degree of
48 temporal synchronicity of structural changes within the orogen and causative climatic changes.
49 A potential example of this can be found in the Greater Caucasus (GC) and associated Kura
50 Fold-Thrust Belt (KFTB; Figure 1), where some prior work suggested that initiation of the
51 fringing fold-thrust belts, including the KFTB may reflect a climatically driven widening of the
52 orogen after a shift to more arid conditions (e.g., Forte et al., 2013, 2022). Testing this
53 hypothesis has in part been hindered by the relatively poor constraint on relative timing and
54 along-strike patterns of initiation of individual structures within the range and foreland. Here
55 we consider the extent to which sediment provenance can elucidate the structural history of
56 both the southeastern GC and KFTB and help to resolve whether the growth of the KFTB was
57 largely synchronous along-strike and is thus compatible with being driven by climatically
58 induced widening of the orogen.

59 Specifically, while recent work by Trexler et al., (2022, 2023) has significantly clarified
60 the locations, geometry, and nature of many of the first-order structures within the internal GC,
61 the timing and evolution of these first-order structures remain under-constrained, with the
62 exception of very specific locations in the western GC (Vasey et al., 2020) and extreme eastern
63 GC (Tye et al., 2022). Similarly, while it is relatively well constrained that since initiation,
64 portions of the KFTB have accommodated upwards of 50% of the orogen-perpendicular
65 shortening between Arabia and Eurasia, and nearly all of the convergence between the Greater
66 and Lesser Caucasus between 45-49°E (Forte et al., 2010, 2013), the exact timing of KFTB

67 initiation and the extent to which the structures within the KFTB initiated diachronously or
68 synchronously along-strike both remain unclear.

69 The formation of the KFTB is coincident with either a reduction in activity, or largescale
70 abandonment, of the GC range front thrust(s) (e.g., Forte et al., 2010; Mosar et al., 2010) and
71 represents a southward advance of the active thrust front by ~25-100 km, implying significant
72 widening of the orogen, and simultaneous formation of the Alazani piggyback basin (Figure 1).
73 As such, the formation of the KFTB reflects a significant structural reorganization within the
74 southeastern GC (e.g., Forte et al., 2010; Mosar et al., 2010), and constraining the timing and
75 evolution of deformation within the KFTB is critical for understanding the broader structural
76 evolution of the GC and the context of this reorganization. For example, based on relatively
77 limited data, Forte et al., (2013) originally hypothesized that initiation of the KFTB, and
78 resultant widening of the GC, initiated at 1.5-1.8 Ma, coincident with regional records of an
79 increase in aridity (e.g., Kvavadze and Vekua, 1993; Gabunia et al., 2000; Kovda et al., 2008;
80 Messenger et al., 2010a, 2010b). Forte et al., (2013) considered that this shift to more arid
81 conditions could have initiated orogen widening and KFTB formation, consistent with the
82 proposal that active, doubly-vergent orogens experiencing less efficient erosion will expand
83 (Whipple and Meade, 2004, 2006). If orogenic widening driven by climatic forcing is a viable
84 mechanism to explain the formation of the KFTB, this fundamentally predicts that initiation of
85 the KFTB was synchronous along-strike.

86 While some prior work suggested a diachronous initiation of the KFTB along strike (Forte
87 et al., 2010), recent constraints suggest a more synchronous initiation is viable, although these
88 constraints come from the western and eastern termini of the belt (Figure 2; Forte et al., 2013;

89 Lazarev et al., 2019; Sukhishvili et al., 2021). The eastern KFTB initiated at ~2.1 Ma at the
90 boundary between the Akchaglyian and Apsheronian regional stages (Forte et al., 2013; Lazarev
91 et al., 2019), and the western KFTB in the Gombori range initiated sometime between 2.7-1 Ma
92 (Sukhishvili et al., 2021). To better understand the tectonic context of the KFTB it is necessary
93 to establish the timing of the central KFTB and the relationship between thrust propagation and
94 evolution of structures internal to the southeastern GC. Here we investigate these problems by
95 tracking changes in provenance in the foreland sedimentary strata now exposed within the
96 KFTB.

97 Prior work describing source terranes within the GC broadly suggest relatively distinct,
98 thrust-bounded packages that have the potential to leave diagnostic signatures within the
99 strata deformed by the KFTB (e.g., Cowgill et al., 2016; Tye et al., 2020). However, the
100 previously available provenance data within the Kura Basin and associated KFTB region are
101 limited and focused primarily on the oil-producing sandstones of the Productive Series at the
102 eastern edge of the Kura Basin (Morton et al., 2003; Allen et al., 2006; Abdullayev et al., 2018)
103 or on strata at its western and eastern ends, all of which are inferred to largely predate
104 formation of the KFTB (Tye et al., 2020).

105 To explore the tectonic history of both the southeastern GC and KFTB, we present new
106 detailed provenance analyses from Miocene-Pleistocene sedimentary rocks that are now
107 exposed within the central portion of the KFTB. A majority of prior provenance work within the
108 GC focuses on either detrital zircon (DZ) U-Pb geochronology (Allen et al., 2006; Cowgill et al.,
109 2016; Abdullayev et al., 2018; Tye et al., 2020) or sandstone/modern sediment petrography or
110 geochemistry (Vincent et al., 2013; Vezzoli et al., 2014, 2020). We build on this context and

111 consider U-Pb ages from detrital zircons, sandstone composition from petrography, and bulk-
112 sample major and trace element geochemical data. To compare source characterizations
113 between DZ and geochemical and/or framework grain compositions, we supplement our
114 foreland samples with additional geochemical analyses of both modern sediments from rivers
115 draining the southern GC and northern Lesser Caucasus and Mesozoic-aged sandstone and
116 volcanic rocks within the GC. With these data we specifically address the following questions:
117 (1) how did the provenance of the northern Kura Basin evolve during the early growth of the
118 GC; (2) what does the evolution of foreland provenance during this time suggest for structural
119 evolution of the southeastern GC; and (3) does the provenance constrain the timing of KFTB
120 initiation and along-strike evolution, and if so, did the belt initiate synchronously along-strike as
121 predicted by models of climatic modulation of a bivergent orogenic wedge?

122 The results of our multi-proxy approach reveal fundamental, and in many ways
123 confusing, disconnects between implied provenance changes from geochemistry and
124 petrography compared to detrital zircon geochronology. On the one hand, the geochemistry
125 and petrography data suggest a general up-section shift from one GC-related source to another
126 that appears to have occurred asynchronously across the basin. On the other hand, a more
127 limited dataset of detrital zircon geochronology suggests effectively static sediment sourcing
128 through time. We interpret this apparent discrepancy to result from sediment recycling, where
129 the apparent up-section change in provenance inferred from the geochemical and petrographic
130 data is a signal generated by selective weathering. Specifically, we infer that exhumation,
131 exposure, weathering, and erosion of foreland basin sediments from thrust sheets within the
132 KFTB led to selective weathering of components that are diagnostic of one of the key GC source

133 terranes, and thus producing a signal that looks like a change in provenance. As a result, we
134 argue that the onset of this sediment recycling signal is actually indicative of the timing of
135 structural initiation of portions of the KFTB and thus helps to establish the timing and along-
136 strike evolution of the KFTB and place it in tectonic context with the structural evolution of the
137 southeastern GC.

138

139 **2. BACKGROUND**

140 **2.1 Tectonic Setting**

141 The GC are the main locus of Arabia-Eurasia convergence at their longitude and form
142 the northern structural margin of the collision (Figure 1; e.g., Philip et al., 1989; Jackson, 1992;
143 Allen et al., 2004; Dhont and Chorowicz, 2006; Reilinger et al., 2006). The range results from
144 ongoing Cenozoic shortening that partially inverted a Jurassic-Cretaceous back-arc basin, which
145 opened north of the Pontide-Lesser Caucasus (LC) island arc during north directed subduction
146 of Neotethyan oceanic lithosphere (e.g., Adamia et al., 1977; Gamkrelidze, 1986; Zonenshain
147 and Le Pichon, 1986; Cowgill et al., 2016; Vincent et al., 2016; van Hinsbergen et al., 2019;
148 Vasey et al., 2021). Significant debate has centered on the early Cenozoic geometry and
149 dimensions of the GC back-arc basin north of the LC (Cowgill et al., 2016, 2018; Vincent et al.,
150 2016, 2018), but paleogeographic reconstructions constrain the NE-SW width to being between
151 200-400 km (van der Boon et al., 2018; van Hinsbergen et al., 2019; Darin and Umhoefer, 2022),
152 similar to the dimensions of the Black Sea and South Caspian basins, which are likely remnants
153 of the same back-arc basin system (Zonenshain and Le Pichon, 1986). Timing of initiation of
154 closure and shortening of the GC back-arc basin is unclear, but had likely begun by the Eocene-

155 Oligocene (e.g., Vincent et al., 2007) and was accommodated in part by northward subduction
156 of oceanic or transitional lithosphere, based on seismic evidence of a subducted slab in the
157 eastern GC (Skolbeltsyn et al., 2014; Mumladze et al., 2015; Gunnels et al., 2020). The timing of
158 the transition from subduction to collision and beginning of significant upper plate shortening
159 and exhumation has also proven controversial, but recent new results from, and syntheses of,
160 low-temperature thermochronology data have largely confirmed the original suggestion by
161 Avdeev and Niemi (2011) of initiation of rapid exhumation between 10-5 Ma throughout much
162 of the range (e.g., Vincent et al., 2020; Forte et al., 2022; Tye et al., 2022; Cavazza et al., 2023).
163 Subsequently, active deformation and the locus of shortening at the surface has largely shifted
164 to a series of fringing foreland fold-thrust belts in the northcentral and northwestern
165 (Sobornov, 1994, 1996, 2021; Forte et al., 2014), southwestern (Banks et al., 1997; Tsereteli et
166 al., 2016; Tibaldi et al., 2017, 2018, 2021; Trexler et al., 2020; Alania et al., 2021b), southcentral
167 (Alania et al., 2021a), and southeastern (Forte et al., 2010, 2013, 2014; Alania et al., 2015) GC.
168 The initiation of the majority of these fold-thrust belts are broadly constrained to occurring
169 during the Plio-Pleistocene. Our focus here is on clarifying the initiation age of the southeastern
170 fold thrust-belt, i.e., the KFTB.

171

172 **2.2 Regional Geology**

173 The geology of the central and eastern GC (Figure 1c) is dominated by Jurassic to
174 Cretaceous shallow-marine carbonate rocks along the northern flank, Jurassic to Cretaceous
175 flysch to molasse within much of the core of the orogen, and Jurassic to Cretaceous volcanic
176 and volcanoclastic rocks along the southern flank (e.g., Saintot et al., 2006; Adamia et al., 2011a;

177 Forte et al., 2014; Cowgill et al., 2016; Tye et al., 2020). Three observations of the regional
178 geology are particularly important with respect to sediment provenance and potential source
179 terranes for sediments within the Kura foreland basin. First, within the GC, intrusive,
180 metamorphic, and metasedimentary rocks predating Jurassic rifting in the GC back-arc basin are
181 only exposed in the western GC (Undifferentiated Basement in Figure 1c; Saintot et al., 2006;
182 Adamia et al., 2011a). Second, there are two geographically distinct sequences of
183 predominantly Jurassic to Cretaceous volcanic and/or volcanoclastic rocks exposed along the
184 southern margin of the GC, with the one in the west being more extensively exposed and
185 having a wider cross-strike width than the one in the east; the latter is sometimes referred to as
186 the Vandam zone and both are considered to be genetically linked with the similarly aged
187 Pontide-Lesser Caucasus Arc (e.g., Kopp and Shcherba, 1985). Third, and finally, there are
188 various small exposures of Paleozoic to Precambrian crystalline rocks within the Dzirula Massif
189 (Zakariadze et al., 1998; Mayringer et al., 2011; Shengelia et al., 2012) and Lesser Caucasus
190 (e.g., Khrami & Loki Massifs - Gamkrelidze et al., 2011; Rolland et al., 2011).

191 Structurally, the interior of the GC is dominated by south-directed thrusts and reverse
192 faults that progressively steepen toward the interior of the range (Figure 1; Philip et al., 1989;
193 Saintot et al., 2006; Mosar et al., 2010; Adamia et al., 2011b; Somin, 2011; Trexler et al., 2022,
194 2023). While many prior works describe the structural architecture of the internal GC in the
195 context of a single master structure or structures, often referred to as the Main Caucasus
196 Thrust (e.g., Philip et al., 1989; Mosar et al., 2010), recent work has suggested that the majority
197 of thrusts along the southern margin of the range accommodate similar amounts of
198 displacement (Vasey et al., 2020; Trexler et al., 2022) and especially in the eastern GC it's

199 actually unclear which structure(s) should be considered the MCT (e.g., Forte et al., 2015b and
200 discussions therein). More critical to our efforts are that many of these structures juxtapose
201 rocks of different composition and/or detrital zircon age populations, so that initiation and
202 activity of these structures during deformation of the GC is expected to have produced
203 diagnostic provenance changes in the foreland basin (Figure 1). Of particular importance is the
204 Vandam zone (Figure 1c), a thrust-bounded terrane of predominantly Mesozoic-aged volcanic
205 and volcanoclastic rocks that is likely a continuation of, or at least genetically linked to, the LC
206 Arc (Kopp and Shcherba, 1985). The Vandam zone was accreted into the range between 13-3
207 Ma and subsequently deformed (Tye et al., 2022).

208

209 **2.3 Prior Work on Source Terranes**

210 Potential source terranes and their expected provenance signatures in foreland strata of
211 the Caucasus region are relatively well characterized in terms of U-Pb ages of zircons (Allen et
212 al., 2006; Wang et al., 2011; Cowgill et al., 2016; Vasey et al., 2020; Tye et al., 2020; Forte et al.,
213 2022; Trexler et al., 2022) and to a lesser extent, heavy mineral assemblages (Morton et al.,
214 2003; Morton and Yaxley, 2007; Vezzoli et al., 2014, 2020). Prior work by Tye et al. (2020)
215 integrated both modern sediments and bedrock samples (Allen et al., 2006; Wang et al., 2011;
216 Cowgill et al., 2016; Vasey et al., 2020; Trexler et al., 2022) to define a suite of 7 distinct source
217 terranes distinguishable in detrital zircon U-Pb age populations within the Caucasus region:
218 Eurasian interior, Pre-Jurassic sedimentary rocks, GC basement, GC siliciclastic strata, eastern
219 GC volcanoclastics, western GC volcanoclastics, and Transcaucasus basement and LC arc. While
220 these individual sources do not correspond to single mapped units (Tye et al., 2020), they do

221 define three broad geographic groups: those that reflect a source from the East European
222 Craton to the north of the GC (Eurasian interior), a GC source (Pre-Jurassic sedimentary, GC
223 basement, GC siliciclastic strata, eastern GC volcanics, western GC volcanics), or a LC
224 source (Transcaucasus basement and LC arc). In more detail, the GC sources roughly
225 correspond to distinct tectonostratigraphic and, in part, geographic zones within the GC itself,
226 with the Pre-Jurassic sedimentary and GC basement reflecting exposures in the core of the
227 western orogen, the GC siliciclastics corresponding to the Jurassic to Cretaceous flysch exposed
228 throughout the range, and the western and eastern GC volcanics corresponding to the two
229 volcanic packages along the southern range front, the latter of which is also effectively the same
230 as the Vandam zone (Figure 1). The 7 source terranes defined by Tye et al. (2020) largely reflect
231 differences in the relative proportions of 6 different distinct age populations within given
232 samples, specifically: (1) grains < 90 Ma associated with the LC arc, (2) grains 90-200 Ma
233 associated with the LC arc or GC rifting, (3) grains 200-380 Ma associated with the Variscan
234 orogeny, (4) grains 380-500 Ma associated with an earlier arc that formed along, and then
235 rifted from, the former northern margin of Gondwana prior to accretion onto the southern
236 margin of Eurasia (Laurussia), (5) grains 500-900 Ma associated with the Pan-African orogeny,
237 and (6) >900 Ma grains associated with East European craton. Recently, alternative
238 characteristic age divisions within GC and LC detrital zircon ages have been presented by Vasey
239 et al., (2024) that clarify details of the Mesozoic and Paleozoic history of the region, but as the
240 exact interpretations of these age divisions are not critical for our understanding of the recent
241 (i.e., late Cenozoic) structural history of the GC or KFTB, we elect to maintain the somewhat
242 simpler divisions of Tye et al., (2020).

243 A relatively smaller amount of work in terms of geographic area covered has considered
244 the heavy mineral assemblage of potential source terranes within the Caucasus region (e.g.,
245 Morton et al., 2003; Morton and Yaxley, 2007; Vincent et al., 2007; Vezzoli et al., 2014, 2020).
246 Here we focus on results from Morton et al. (2003) and Morton & Yaxley (2007) because Vezzoli
247 et al. (2014, 2020) focus on sources in the far western and northern GC, and so do not appear
248 to be relevant for provenance within the Kura Basin. Morton et al. (2003) and Morton & Yaxley
249 (2007) consider heavy mineral assemblages from the modern Volga (which represents
250 contributions from the East European Craton), the modern Kura River (which drains both the
251 GC and LC), and several smaller rivers draining the eastern tip of the GC. Broadly, the results
252 highlight relatively distinct provenance signatures between all three sources. The Volga is
253 dominated by primarily stable, more evolved and felsic components. In contrast, the Kura River
254 is dominated by more unstable components like clinopyroxene and amphibole sourced from
255 extensive volcanic deposits in the LC. Finally, the GC reflects a mixture of both stable and
256 unstable components, including species like clinopyroxene, but generally in lower abundances
257 than in the Kura River (Morton et al., 2003; Morton and Yaxley, 2007).

258

259 **2.4 Kura Basin Framework and Regional Timescale**

260 Here we focus primarily on the stratigraphic framework of the Kura Basin, a foreland
261 basin to the southeast of the GC and subbasin of the South Caspian (Figure 1, e.g., Khain, 1975;
262 Philip et al., 1989; Kremenetskiy et al., 1990). Although at present the GC is separated from the
263 Kura Basin by the KFTB and piggy-back Alazani Basin to the north, all three components formed
264 a single continuous basin prior to the formation of the KFTB. Thus, we consider the stratigraphy

265 exposed within the KFTB to largely represent deposition within this former, larger version of the
266 Kura Basin. Results from deep-boreholes drilled during the 1970s reveal that the stratigraphic
267 fill of the central Kura Basin, which spans the Cenozoic, is deposited on top of Jurassic-
268 Cretaceous volcanic rocks thought to be associated with the Lesser Caucasus (LC) arc (Agabekov
269 et al., 1976; Shikalibeily et al., 1988). Seismic velocities within the Kura Basin suggests that the
270 Cenozoic sediment thicknesses exceed 10 km through much of the basin, with thickness likely
271 exceeding 15 km at the western and eastern ends of the KFTB (Gunnels et al., 2020). The
272 seismic velocity of the Mesozoic floor of the Kura Basin is consistent with it either being oceanic
273 crust or highly attenuated continental crust (McKenzie et al., 2019; Gunnels et al., 2020),
274 consistent with it representing a still-subducting portion of the former GC back-arc basin.

275 Depositional environments represented by strata exposed in the KFTB vary from shallow
276 marine to terrestrial and the strata are predominantly siliciclastic, with general coarsening-
277 upward trends observed throughout most stratigraphic sections (e.g., Agustí et al., 2009; Forte
278 et al., 2013, 2015a; van Baak et al., 2013; Lazarev et al., 2021). Strata exposed in the KFTB were
279 deposited in environments influenced by both the development of the GC and KFTB (e.g., Forte
280 et al., 2013, 2015) and large-magnitude (~1000 m) base level changes of the Caspian Sea during
281 the late Cenozoic (e.g., Popov et al., 2006; Forte and Cowgill, 2013; van Baak et al., 2017;
282 Krijgsman et al., 2019; Lazarev et al., 2021). Variations in Caspian Sea base level, along with
283 potentially related intermittent connections between the Black and Caspian Sea along the
284 southern rangefront of the GC (e.g., Popov et al., 2010; Forte and Cowgill, 2013; van der Boon
285 et al., 2018; van Hinsbergen et al., 2019) are often considered a first-order driver of stratigraphy
286 within the Kura Basin. As such, the stratigraphy of the Kura Basin and surrounding regions is

287 classified in terms of regional stages associated with transgressions and regressions of the
288 Caspian Sea, and associated changes in biota (e.g., Zubakov and Borzenkova, 1990; Jones and
289 Simmons, 1996).

290 We primarily place our provenance and resulting structural interpretations into the
291 temporal context of the regional Caspian timescale as opposed to a global timescale. We do
292 this for two reasons. First, this approach helps insulate our results from the disruption of future
293 revisions to Caspian timescale and its correlation with the global timescale. Establishing the
294 absolute ages of the boundaries between Caspian stages, their correspondence with stages in
295 the Paratethyan realm more broadly, and their correlation to the global timescale have all
296 proven extremely controversial, with significant revisions and/or shifts numerous times over
297 the past several decades (see review in Krijgsman et al., 2019). Some of these changes were
298 significant enough to shift a regional stage from one global stage to another. While
299 concentrated magneto- and biostratigraphic work has significantly clarified the temporal
300 extents of individual Caspian and related Paratethyan stages, disagreements remain, likely
301 because (1) specific stage-bounding transgressive or regressive surfaces may have formed at
302 different times in different Paratethyan basins and/or (2) the individual stage-bounding
303 surfaces may be time-transgressive within individual basins and their subbasins (e.g., Vasiliev et
304 al., 2011; van Baak et al., 2013, 2017, 2019; Forte et al., 2015a; Richards et al., 2018; Krijgsman
305 et al., 2019; Lazarev et al., 2019, 2021). Because of the long-standing and ongoing problems
306 with correlation of the regional stages to standard international geological epochs, nearly all
307 prior international literature on the stratigraphy of this region has used regional stage names
308 (e.g., Mamedov, 1973; Jones and Simmons, 1996; Vincent et al., 2010, 2013; Vasiliev et al.,

309 2011, 2022; van Baak et al., 2013; Van Baak et al., 2016; van Baak et al., 2017, 2019; Richards et
310 al., 2018; Krijgsman et al., 2019; Lazarev et al., 2019, 2021; Palcu et al., 2019; Aghayeva et al.,
311 2023). Thus, our second reason for using regional stage names is to follow this prior work.

312 The regional age divisions of primary relevance to the measured stratigraphic sections
313 presented here are, from oldest to youngest: Meotian (base 7.65 Ma - Palcu et al., 2019),
314 Pontian (base 6.12 Ma - Van Baak et al., 2016), Productive Series (base 5.33 Ma - Aghayeva et
315 al., 2023), Ackgahylian (base 2.7 Ma - Krijgsman et al., 2019; base 2.95 Ma - Lazarev et al.,
316 2021), Apsheronian (base 2.1 Ma - Lazarev et al., 2019), and Bakunian (base 0.8 Ma - van Baak
317 et al., 2013) (Figure 2).

318 In the present study, we use Caspian timescales derived from magnetostratigraphy of
319 several sections in the Apsheron Peninsula and eastern Kura Basin (Krijgsman et al., 2019 and
320 references therein) and the Kvabebi section within the western KFTB (Figure 1; Lazarev et al.,
321 2021). The timescales are equivalent except for the age of the base of the Akchagylian regional
322 stage (Figure 2), which represents a transgressive surface reflecting a ~200 meter base level rise
323 of the Caspian following an extreme (~600 m below modern base level) regression during the
324 preceding Productive Series time (e.g., van Baak et al., 2017, 2019; Lazarev et al., 2021). In the
325 composite timescale of Krijgsman et al., (2019), the Akchagylian spans from 2.7 to 2.1 Ma,
326 whereas in the timescale of Lazarev et al., (2021) the Akchagylian is longer and spans from 2.95
327 to 2.1 Ma. Lacking a basis on which to choose between these two alternate timescales, we
328 consider both when correlating the KFTB stratigraphy to the global timescale.

329

330 **2.5 Prior Work on Foreland Provenance**

331 Published studies of provenance in the foreland basins of the GC are limited. Existing
332 results (Figure 1) include isolated data from the Rioni Fold-Thrust Belt and related Cenozoic
333 stratigraphy of the western GC (Vincent et al., 2013, 2014; Tye et al., 2020), the extreme
334 western and eastern termini of the KFTB (Tye et al., 2020), and an expansive dataset focused on
335 exposures of Productive Series strata on the Apsheron Peninsula and in the eastern Kura Basin
336 (Morton et al., 2003; Allen et al., 2006; Morton and Yaxley, 2007; Abdullayev et al., 2018).
337 Those from the KFTB, Kura Basin, and Apsheron Peninsula are the most relevant here.

338 Results of heavy mineral analysis of Productive Series sandstones sampled on the
339 Apsheron Peninsula are similar to those of the modern Volga River and rivers draining the
340 eastern tip of the GC (Morton et al., 2003; Morton and Yaxley, 2007). This is consistent with the
341 suggestion that during the extreme Caspian Sea low-stand coeval with Productive Series
342 deposition, the paleo-Volga River mouth migrated southwards and entered the Caspian near
343 the modern day position of the Apsheron Peninsula (e.g., Reynolds et al., 1998; Aliyeva, 2005;
344 Kroonenberg et al., 2005; Vincent et al., 2010). Contrastingly, samples of Productive Series
345 sandstones from the eastern margin of the Kura Basin, near the modern Kura River, contain a
346 decidedly different heavy mineral assemblage, more consistent with samples from the modern
347 Kura River taken near its outlet into the Caspian Sea (Morton et al., 2003; Morton and Yaxley,
348 2007). Generally, both modern Volga River samples and Apsheron Peninsula Productive Series
349 rocks are characterized by more evolved, felsic heavy mineral assemblages when compared
350 with samples from the Kura River or Kura Basin Productive Series rocks (Morton and Yaxley,
351 2007). In general, Morton et al., (2003) and Morton & Yaxley, (2007) suggest that the presence
352 of distinctive unstable species like clinopyroxene and calcic amphiboles in sediments are

353 strongly suggestive of LC sourcing. However, Trexler et al. (2022) report both of these phases in
354 Jurassic volcanic and volcanoclastic rocks of the western GC in Georgia.

355 The heavy mineral results from the Apsheron Peninsula exposures of Productive Series
356 sediments are largely reinforced by detrital zircon age populations (Allen et al., 2006;
357 Abdullayev et al., 2018), which are dominated by >900 Ma grains characteristic of the East
358 European Craton and rivers draining this terrane (Safonova et al., 2010; Wang et al., 2011; Tye
359 et al., 2020) and which are encapsulated into the Eurasian Interior DZ source defined by Tye et
360 al., (2020). In contrast, detrital zircon data from the extreme eastern GC and KFTB and western
361 KFTB sampled from sedimentary strata ranging in age from Paleogene to Quaternary record
362 mixtures of source terranes indicative of sourcing from either the GC or LC, with minimal input
363 from the Eurasian Interior (Tye et al., 2020). The majority of foreland samples from Tye et al.,
364 (2020) show affinity with one or more of the GC-associated sources, but some samples (e.g.,
365 sample CF-1), even those extremely proximal to or within the modern GC (e.g., sample EF-6),
366 show affinity with the Transcaucas basement and LC arc source. Where such provenance
367 affinities are present, Tye et al., (2020) largely follow Morton et al., (2003) in considering these
368 samples to reflect deposition of sediment delivered by a paleo-Kura river system,
369 predominantly draining the LC, requiring a paleo-Kura river that is in part shifted northward and
370 much closer to the GC range front relative to its modern position. Ultimately, with respect to
371 the questions we consider here, the majority of existing detrital zircon data within the
372 southeastern foreland; (1) are derived from strata that are largely pre-tectonic with respect to
373 both rapid exhumation of the GC and possible formation of the KFTB and (2) also lack detailed
374 stratigraphic or structural context (Tye et al., 2020), and as such, interpreting either unroofing

375 patterns from the GC or details of the KFTB are challenging. We address these difficulties
376 directly in this work. We begin by describing the stratigraphic context of the provenance
377 samples we analyze (section 3). Next, we introduce methods and results to establish
378 correlations between the sampled measured sections and the regional timescale (section 4).
379 Finally, we present the methods and results of a diverse suite of provenance techniques
380 (section 5).

381

382 **3 SAMPLE DESCRIPTION AND CONTEXT**

383 The samples that form the basis for this work mainly represent either A) samples of
384 foreland basin deposits with unknown provenance sampled from five Mio-Pleistocene
385 measured stratigraphic sections exposed within the KFTB or B) samples to characterize
386 potential sources for these foreland-basin deposits. The sample types can be further divided
387 into four groups (Tables 1, 2, and 3). In group A there is (1) volcanic ash from within the five
388 measured stratigraphic sections or adjacent regions to enable stratigraphic correlations, and (2)
389 sandstone with unknown provenance from the same stratigraphic sections. Within group B
390 there are (3) modern stream sediments with catchments in adjacent mountains to characterize
391 potential source areas for the KFTB sandstones, and (4) Mesozoic volcanic and volcanoclastic
392 rocks of the Vandam zone now exposed within the GC to further clarify aspects of potential
393 source areas for the KFTB sandstones. The majority of KFTB sandstone samples of unknown
394 provenance were 2-4 kilograms of medium to coarse-grained sandstone whereas sample
395 volume of ash horizons varied depending on thickness of the particular deposits.

396 **3.1 Stratigraphic Context of KFTB Sandstone and Ash Samples**

397 The five measured sections are at Vashlovani and Sarica (Forte et al., 2015a), Xocashen
398 (van Baak, 2010; Forte, 2012; van Baak et al., 2013), Bozdagh (Forte, 2012), and Goy (Forte et
399 al., 2013; Lazarev et al., 2019) and we refer readers to the source publications for detailed
400 stratigraphic descriptions, logs, and ancillary data such as biostratigraphy (Figure 1, 2). To
401 facilitate placing the 8 ash and 27 sandstone samples that come from these sections into
402 stratigraphic context, we provide brief descriptions of the stratigraphy of each measured
403 section in the supplement (Section S1). Sandstone sample names indicate both the name of the
404 measured section and stratigraphic height above base at which the sample was collected. Thus,
405 sample V-15 is from the Vashlovani section, 15 meters above the section base. Original (field)
406 sample names are reported in Table 2. Summary geologic maps showing the detailed locations
407 and geological context of the sections are provided in the supplement (Figures S1-S5).

408 To interpret the provenance records from the measured sections, it is necessary to
409 correlate them to each other and the regional timescale. Forte (2012) proposed an initial set of
410 correlations between the five measured sections considered here. However, that correlation
411 lacked detailed tephra glass geochemistry reported below (Section 4) and predated both new
412 magnetostratigraphic work (Lazarev et al., 2019) and significant revisions to the regional
413 timescale (e.g., van Baak et al., 2017; Krijgsman et al., 2019; Lazarev et al., 2021). In section 4
414 we present an updated correlation based on these new data sources and prior
415 magnetostratigraphy (e.g., van Baak et al., 2013) and mapping (Abdullaev et al., 1957; Ali-Zade,
416 2005; Forte et al., 2015a).

417 **3.2 Context of Samples of Known Provenance**

418 The 13 samples of modern stream sediment (Figure 1) typically comprised >4 kg of
419 medium- to coarse-grained modern river sand collected from the active channel at locations
420 chosen to characterize particular source terranes within the adjacent mountain ranges. The
421 source areas include the Greater Caucasus Paleozoic core (Enguri), Jurassic-Cretaceous Greater
422 Caucasus Basin sediments (Aragvi, Zaqatala, Kumuk, Kish, and Damiraparan), Dzirula Massif
423 (Kvirila), Achara-Trialet and western Lesser Caucasus (Mtkvari, which is the upstream
424 equivalent of the Kura), and Lesser Caucasus Arc (Tovuz, Shamkir, and Zayam). Where
425 applicable, samples were collected up-stream of major dams (e.g., Enguri). For these samples,
426 we present bulk geochemistry as described in the methods section below. Detrital zircon U-Pb
427 age populations for four of these rivers (Enguri, Kumuk, Mtkvari, and Tovuz) were presented by
428 Cowgill et al., (2016). For the 11 volcanoclastic samples from the Vandam, we analyzed bulk
429 geochemistry for all and sandstone petrography for a subset (6). A detrital zircon population
430 was published for one of these samples (AB0862 = SEGC) by Cowgill et al., (2016).

431

432 **4. STRATIGRAPHIC CORRELATIONS**

433 The source publications for each of the 5 measured sections provide existing age
434 estimates (see Supplement Section S1, Figure S1-S5). In this section we use major element
435 chemistry of glass shards isolated from ash horizons (Figure S6) (Table 3) to refine stratigraphic
436 correlations between these sections, and thus their ages.

437 **4.1 Analytical Methods for Major Element Geochemistry of Volcanic Glass**

438 Major element fingerprinting of volcanic glass shards within tephra deposits is a useful
439 stratigraphic correlation tool (e.g., Lowe, 2011; Lowe et al., 2017). For this study, geochemical

440 analyses were conducted on volcanic glass shards (125-250 μm) manually separated from 8
441 tephra samples collected from locations throughout Georgia and Azerbaijan; an additional 9th
442 sample (B-A) from Bozdagh yielded no usable glass shards. Five of the samples came from
443 measured sections described previously (B-B from Bozdagh, X-2A, X-3A, X-3B from Xocashen,
444 and G-A from Goy), whereas the other three (TG, WQ-A, and WQ-B) were collected in similarly
445 aged units in the eastern KFTB mapped by Forte et al., (2013), which we include largely for
446 future work in this region. Sample locations are in Table 3. All tephra samples were separated
447 and cleaned following common tephra preparation procedures (e.g., Roman et al., 2008).
448 Specifically, samples were first wet sieved at Arizona State University (ASU) using 20-40-60-80
449 mesh sieves. The 40-60 mesh fractions were washed with 5% nitric acid to remove any
450 carbonates, rinsed with deionized (DI) water, and then washed with 5% hydrofluoric acid (HF)
451 one to three times, in 2-minute ultrasonic baths to remove clay adhering to the glass shards.
452 Glass shards were then mounted in epoxy rounds, polished, and carbon coated for analysis in
453 an electron microprobe.

454 Individual glass shards were analyzed for major element oxide abundances (SiO_2 , Al_2O_3 ,
455 K_2O , Na_2O , CaO , MgO , MnO , Fe_2O_3 and TiO_2) using a JEOL JXA-8530F Electron Probe
456 Microanalyzer (EPM) with JEOL software in the John M. Cowley Center for High Resolution
457 Electron Microscopy at ASU. Using wavelength-dispersive spectrometry (WDS), the instrument
458 was operated at 15 kV, with a 10 nA beam current and a 15 μm defocused beam to minimize
459 alkali loss (Froggatt, 1992; Lowe, 2011). All data were adjusted using atomic number (Z),
460 absorption (A), and fluorescence (F) corrections. If possible, 20 or more glass shards were
461 analyzed for each sample. To assess analytical precision, the Lipari glass INTAV standard (Kuehn

462 et al., 2011) and the Los Posos Rhyolite (RHY5) in-lab standard were run at the start and end of
463 an analysis session, and after every 40-60 unknown analyses.

464 Major element analytical results are reported as un-normalized data averages with 1σ
465 standard deviation error (Table 3). Brief descriptions of the glass and crystals (if present) are
466 also provided in Table 3. Individual shard analyses are reported in the supplement (Table S1).
467 Individual analyses with totals <90% or with otherwise anomalous values (e.g., $\text{SiO}_2 > 90\%$)
468 were not included in the averages or later statistics but are still reported in the supplement.
469 Low totals can be a result of alteration (potential leaching) or analytical issues and are not
470 viable for considering stratigraphic correlations.

471 **4.2 Statistical Methods for Major Element Geochemistry of Volcanic Glass**

472 In our treatment of the major element data for the volcanic glasses, we primarily follow
473 recommendations from Lowe et al., (2017). Specifically, we explore potential correlations with
474 plots of log-ratios of various major elements pairs and select one set ($\text{CaO}/\text{Al}_2\text{O}_3$ and
475 $\text{TiO}_2/\text{Fe}_2\text{O}_3$) that provided meaningful separation of different tephra beds or components. Prior
476 to plotting, rounded zeroes (quantities measured but present in amounts below the detection
477 limit) were replaced by nonparametric imputation as described by Martín-Fernández et al.,
478 (2003) using the CoDaPack software package (Comas-Cufí and Thió-Henestrosa, 2011). We
479 compare this with the results of a principal component analysis (PCA), a technique for reducing
480 dimensionality (Krzanowski, 2000), applied to all of the major oxides. Prior to PCA, the oxide
481 concentrations were normalized using a standard scaler so that data were normally distributed
482 with a zero mean and unit variance (Lowe, 2011; Lowe et al., 2017).

483 We also estimated the similarity of the tephra samples via a modified Euclidean distance
484 measure, D^2 , defined by Perkins et al (1995) where,

485

$$486 \quad D^2 = \sum_{k=1}^n \left[\frac{(x_{k1} - x_{k2})^2}{2\sigma_k^2} \right]$$

487

488 and x_{k1} is the concentration of element x_k in the glass of tephra 1, x_{k2} is the concentration of
489 element x_k in the glass of tephra 2, σ_k is the analytical precision of element x_k , and n is the
490 number of elements used in the comparison. We refer to this modified Euclidean distance
491 measure as the "Perkins Distance". Here we select five of the major oxides, CaO, Fe₂O₃, MgO,
492 MnO, and TiO₂, for this distance calculation. We follow Perkins et al., (1995) and do not include
493 Al₂O₃ and SiO₂ in this calculation because they do not show much variation for the majority of
494 samples and could bias the distance measures. Similarly, we exclude Na₂O and K₂O from the
495 calculation because the concentrations of these elements are sensitive to post-depositional
496 hydration of glass shards. Calculated D^2 measures have a chi-squared distribution, and thus
497 with five elements (five degrees of freedom), two tephtras can be considered statistically
498 different at the 95% and 99% confidence levels if D^2 exceeds 11.1 and 15.1, respectively.
499 Correspondingly, D^2 less than these critical values suggest that the respective tephtras may be
500 correlative. We report the D^2 values in Table 5.

501 **4.3 Ash Correlations**

502 Geochemically, 6 of the 8 analyzed ashes contain exclusively rhyolitic shards (Figure S7).

503 The other 2 samples (B-B and X-3A) both have two compositional groups, with rhyolite shards

504 (Mode 1) most abundant and a secondary population (Mode 2) that is somewhat geochemically
505 diverse and distinctly lower in silica, having trachyte to trachyandesite compositions (Figure S7).
506 Bi-plots of log ratios and PCA reveal four broad tephra groupings, one of which includes the
507 Mode 2 shards (Figure 3). Key observations from the bi-plots and PCA for correlating the
508 measured sections are: (1) tephras X-3B and X-2A within the two younger Xocashen sections
509 (plus TG at Goy, see below) are similar and likely indicate a single eruptive source, consistent
510 with other stratigraphic correlations based on the Apsheronian-Bakunian boundary in both
511 sections (van Baak, 2010; van Baak et al., 2013) and (2) tephras X-3A in Xocashen, B-B in
512 Bozdagh, and G-A in Goy are similar and likely represent a second eruptive source. Note that
513 the pairs of Mode 1 and Mode 2 shards in X-3A and B-B also appear similar to each other,
514 although the Mode 2 shards have significant scatter (Figure 3, S7). Although Mode 2 shards are
515 absent from the sample of G-A tephra, we did observe in the G-A ash a distinctively more mafic
516 interval that may represent this Mode but that we unfortunately did not sample (Figure S7).

517 Outside of the measured sections, tephras WQ-A and WQ-B were both sampled from a
518 single outcrop of unit Unit G3 in the Goy area (Forte et al., 2013), with WQ-A stratigraphically
519 below WQ-B by ~40 cm. These two samples group with each other but are distinct from all
520 other samples analyzed here, indicating they likely represent tephras from a third, distinct
521 eruptive source. Tephra TG was collected from a thrust-bounded slice of Unit 2G in the Goy
522 area and was assumed by Forte et al., (2013) to correlate with tephra G-A in the Goy section.
523 However, the new geochemical data indicate TG correlates with tephra X-3B and X-2A in
524 Xocashen, not with G-A.

525 For all the tephras, the correlations derived from the bi-plots are largely identical to
526 those interpreted from statistical distance (Table 5). In detail, the statistical distance measure
527 does not suggest that the more mafic mode 2 of tephras X-3A and B-B are correlative, but this
528 likely reflects the relatively large variability in the geochemistry and small number of shards
529 analyses, with only one shard from X-3A classified as Mode 2.

530 **4.4 Correlations**

531 The new ash geochemistry establishes new ties between Xocashen, Bozdagh, and the
532 Goy sections. Additionally, magnetostratigraphy in Xocashen (van Baak et al., 2013) and Goy
533 (Lazarev et al., 2019) strengthen the correlations between these two sections. Combining these
534 data with prior age calls from geologic mapping (Abdullaev et al., 1957; Ali-Zade, 2005; Forte,
535 2012) and biostratigraphy (Forte et al., 2013, 2015a; van Baak et al., 2013; Lazarev et al., 2019)
536 allows us to correlate the different sections both to each other and the regional timescale
537 (Figure 2). A summary of the key datasets informing our correlations are: (1) magneto- and
538 biostratigraphy allow for direct correlation between Xocashen and Goy and both the regional
539 timescale and global paleomagnetic timescale (van Baak, 2010; van Baak et al., 2013; Lazarev et
540 al., 2019), (2) new ash geochemistry allow for direct correlation between portions of the
541 Xocashen, Bozdagh, and Goy sections (Figure 3), (3) maximum depositional ages from U-Pb ages
542 of detrital zircons in Sarica and Vashlovani allow connection between the global absolute
543 timescale and the regional timescale (Forte et al., 2015a), and (4) mixtures of biostratigraphy,
544 lithostratigraphy, depositional environment interpretations derived thereof and inferred
545 relations to Caspian stages, allow for further correlation between stratigraphy in all sections
546 and the regional timescale (e.g., Abdullaev et al., 1957; Ali-Zade, 2005; Forte, 2012; Forte et al.,

547 2013, 2015a; van Baak et al., 2013; Lazarev et al., 2019). Below we consider specific correlations
548 between units within the measured sections and their respective correlations to the Caspian
549 regional timescale.

550 Based on these data, the Meotian-Pontian stage is exclusively represented by
551 Vashlovani unit V1, which does not correlate to any portions of the other sections. The
552 Productive Series stage is represented by Vashlovani unit V2 and Sarica unit S1. Note that
553 within Sarica, Forte et al., (2015a) previously used a small sub-population of zircons from
554 sample S-210 near the top of unit S1 to determine a maximum depositional age (MDA) of $2.5 \pm$
555 0.24 Ma. This MDA is consistent within uncertainty with deposition during Productive Series
556 time if the age of the Productive-Akchagylian boundary is 2.7 Ma (as reported by Krijgsman et
557 al., 2019), but it is inconsistent if the boundary is at 2.95 Ma (as reported by Lazarev et al.,
558 2021). Although resolving this question is beyond the scope of the present work, it does
559 indicate that the exact position of the Productive-Akchagylian boundary in the Sarica section
560 may be unclear. For our purposes, we assume that the entirety of S1 is within the Productive
561 Series to be consistent with Forte et al., (2015a).

562 The Akchagylian period is represented by the basal portion of unit V3 in Vashlovani, S2
563 in Sarica, X1 in Xocashen-1, and G1 in Goy, which all correlate to each other based on prior
564 results from Forte et al. (2013, 2015a). Forte et al., (2015a) previously reported a relatively
565 large population of young zircon grains in sample V-1240 from Vashlovani unit V3, which they
566 used to establish an MDA of 2.66 ± 0.046 Ma. At the time of publication of Forte et al., (2015a),
567 the maximum depositional age corresponded to a long hiatus between the Akchagylian and
568 Apsheronian (van Baak et al., 2013), making it unclear if the sample was deposited during the

569 Akchagylian or Apsheronian. Subsequent work has refined the age of the Akchagylian-
570 Apsheronian boundary to 2.1 Ma (e.g., Krijgsman et al., 2019; Lazarev et al., 2021). Thus, the
571 MDA from V-1240 is now consistent with deposition during either early- or mid-Akchagylian
572 time, depending on which timescale is chosen.

573 The Apsheronian period is represented by the upper portion of Vashlovani unit V3,
574 Sarica units S3-S5, Xocashen-2 unit X2, Bozdagh units B1-B3, and Goy units G2-A, G2-B, G2-C,
575 and G3, as well as one tephra horizon represented by X-3B, X-2A, and TG and another
576 represented by X-3A, B-B, and G-A. Our interpretation of V3 follows prior mapping from
577 Abdullaev et al., (1957), which places the upper portion of this unit within the Apsheronian.
578 However, V3 lacks a clear lithostratigraphic break, so the location of the Akchagylian-
579 Apsheronian boundary within this unit is uncertain. At first, the correlation between Xocashen
580 ash X-3A and Goy ash G-A may seem at odds with prior magnetostratigraphic results in these
581 two sections (van Baak et al., 2013; Lazarev et al., 2019), but as described in detail in the
582 supplement (see Supplement Section S1.6) are reconcilable if the different sedimentation rates
583 of these two sections are considered.

584 The Bakunian period is represented by Xocashen-2 units XB and X3 and is not directly
585 represented in other sections. Because the upper bounds of the Apsheronian in both Sarica and
586 Bozdagh are not well constrained, the upper parts of these sections may be of Bakunian age,
587 but we do not implement such a correlation here as we have no direct evidence.

588

589 **5. SEDIMENT PROVENANCE**

590 We apply a variety of methods to determine the provenance of samples taken from the
591 measured sections, including sandstone petrography, bulk sediment/rock major and trace
592 element geochemistry, and detrital zircon geochronology (Table 2). We analyze each data type
593 using several different statistical and/or visualization approaches, resulting in a varied and
594 multifaceted study. Ultimately, many of these statistical and/or visualization approaches
595 provide similar conclusions, so for the sake of clarity we present in the main text a streamlined
596 view of the methods, results, and statistical/ visualization approaches, with the additional
597 information provided in the supplement for completeness.

598 In the following sections we consider each type of provenance data separately, first
599 presenting the relevant analytical methods, then the statistical treatments/visualizations we
600 apply to the data, and finally the results and our interpretations. For the geochemistry and
601 petrography data we define new provenance sources here. In contrast, for the detrital zircon
602 geochronology data we use source characterizations previously defined by Tye et al. (2020).
603 Importantly, the two different sets of provenance sources are not the same because of
604 differences in sensitivity between the methods. As we elaborate in the discussion, exploring
605 these differences in sensitivity explains why the different methods appear to record different
606 apparent histories and sources and allows us to leverage those differences to gain deeper
607 insight into the evolution of the KFTB.

608 **5.1 Sandstone Major and Trace Element Geochemistry and Petrography**

609 Both sandstone petrography (e.g., Dickinson, 1970; Dickinson and Suczek, 1979;
610 Ingersoll et al., 1984; Ingersoll, 1990) and major and trace element geochemistry (e.g., Bonjour
611 and Dabard, 1991; Totten et al., 2000; Von Eynatten, 2003; Von Eynatten et al., 2003) are well

612 established methods for determining sediment provenance. It has been suggested that major
613 and trace element geochemistry of bulk-sediments provides a means of discerning provenance
614 that is less biased by effects of chemical alteration and weathering than traditional
615 petrographic approaches (e.g., Dickinson, 1970) and effects of hydraulic sorting that may
616 influence heavy mineral data and related geochronologic techniques (e.g., Von Eynatten et al.,
617 2003; Pe-Piper et al., 2008). However, as applied to the Kura Basin sandstones, the results and
618 implications of bulk geochemistry and sandstone petrography are effectively the same (see
619 Section 5.1.6). As such, we focus here on the use of trace elements to characterize provenance,
620 reporting the methods, results, and discussion of our sandstone petrography in the supplement
621 (Section S2.1, Figures S8 and S9).

622 ***5.1.1 Analytical Methods for Major and Trace Element Analysis***

623 We obtain major and trace element geochemical analyses for 26 of the total 27
624 sandstone samples from the KFTB (unknown provenance), 13 samples of modern river
625 sediment (known provenance), and 11 samples of Mesozoic Vandam volcanoclastic rocks
626 (known provenance), complete results for which are in Table S4. For all but one sample (G-200),
627 these were the same sample material analyzed for sandstone petrography (see Section S2.1).
628 We obtained interior sections of each sample by removing weathering rinds and then sent ~200
629 grams of each sample to Activation Laboratories Ltd. where they were crushed and analyzed
630 according to their Code 4Lithoresearch and Code 4B1 protocols, which are similar to those used
631 by Pe-Piper et al. (2008) and yield concentrations for 44 different elements in total (Table S4).
632 In particular, major-and trace element concentrations were measured using lithium
633 metaborate/tetroborate fusion ICP analysis and ICP-MS analysis, respectively.

634 **5.1.2 Statistical Methods for Major and Trace Element Analysis**

635 Numerous methodologies have been developed to use the bulk rock major and/or trace
636 element geochemistry analyses of siliciclastic sediments to establish tectonic setting (e.g.,
637 Bhatia, 1983; Bhatia and Crook, 1986; Roser and Korsch, 1986; Herron, 1988; Totten et al.,
638 2000), provenance (e.g., Roser and Korsch, 1988; Bonjour and Dabard, 1991; Pe-Piper et al.,
639 2008), or degree of chemical weathering (e.g., Nesbitt and Young, 1982; Harnois, 1988; Fedo et
640 al., 1995). In this work, we consider all three applications of the geochemical data, but in the
641 main text we primarily focus on the use of trace element geochemistry with multivariate
642 statistical techniques to characterize potential source terranes and then classify samples of
643 unknown provenance within that context. In the supplement (Section S2.2) we provide
644 additional methods and results related to both basic tectonic discrimination (Figure S10, S11)
645 and chemical weathering indices (Figure S12) that largely reinforce points that are made
646 clearest with the multivariate statistical treatment.

647 Importantly, before applying multivariate statistical techniques, it is necessary to
648 transform raw compositional data into a form that does not violate the underlying assumptions
649 of those methods, specifically that input data follows a multivariate normal distribution
650 (Aitchison, 1986; Von Eynatten et al., 2003). Several different transformations have been
651 proposed to convert compositional data into a form more appropriate for use in multivariate
652 statistics, and from these we elect to use an the isometric log-ratio (ILR) because it converts
653 compositional data into values suitable for any standard multivariate statistical approach (e.g.,
654 Egozcue et al., 2003; Egozcue and Pawlowsky-Glahn, 2005; Pawlowsky-Glahn and Egozcue,

655 2006). We provide an expanded discussion of alternate transforms in the supplement (Section
656 S2.2.1).

657 For the multivariate statistics we test two different suites of elements. The first is a suite
658 of 17 trace elements (Sc, V, Cr, Co, Ni, Rb, Sr, Y, Zr, Nb, La, Gd, Yb, Hf, Ta, Th, U) and one oxide
659 (TiO_2), which is suggested by Pe-Piper et al. (2008) to provide a good discrimination of source
660 geochemistry in detrital samples. The second suite is a set of 10 major elements (SiO_2 , Al_2O_3 ,
661 $\text{Fe}_2\text{O}_3(\text{T})$, MnO, MgO, CaO, Na_2O , K_2O , TiO_2 , and P_2O_5 and excluding LOI, loss on ignition), which
662 is another suite used by Pe-Piper et al. (2008). For both suites, we replace rounded zeroes in
663 the same manner as for the glass geochemistry using the CoDaPack software, which we also
664 use to transform the compositions into isometric log-ratios (ILR) suitable for multivariate
665 analyses (Table S5). Because our main goal is to understand the relations between the samples,
666 rather than the relations between the measured components, the ILR ratio is suitable even
667 though it is not possible to relate the ILR coordinates to specific measured values (e.g., Egozcue
668 et al., 2003). For this reason, we do not report loadings for the various multivariate analyses
669 performed as they do not provide useful information.

670 To characterize variability and evaluate potential populations within the source
671 terranes, we analyze the ILR transformed compositions for the major and trace element groups
672 of the modern river sediments and Vandam volcanoclastic rocks using both hierarchical
673 clustering analysis and principal component analysis (PCA). These methods have previously
674 been applied to geochemical investigations of provenance data and are useful for
675 understanding potential groupings (e.g., Smosna et al., 1999; Pe-Piper et al., 2008). Hierarchical
676 clustering essentially evaluates the “closeness” of given samples to each other and the results

677 are typically represented graphically on a dendrogram (Krzanowski, 2000). PCA is a technique
678 for reducing dimensionality (Krzanowski, 2000) and can also be evaluated graphically, with
679 similarity being indicated by a grouping on a plot of the principal component (Pe-Piper et al.,
680 2008). We perform both the hierarchical clustering and principal component calculations in the
681 “R” software package (Team, 2010), using the “pvclust” library (Suzuki and Shimodaira, 2009) in
682 the hierarchical clustering analysis to generate a dendrogram with boot-strapped p-values
683 (Shimodaira, 2004) to provide an estimation of the robustness of the clusters indicated on the
684 dendrogram. In detail, we use the “Ward” method of clustering and the “Euclidean” distance. In
685 both the cluster analysis and PCA, the suite of major elements does not prove useful in
686 discriminating different populations and in the case of the principal component analysis fails to
687 capture significant portions of the data variance, so these results are not presented, and the
688 major elements set are not used in future analyses.

689 We then use the results of the clustering and principal component analyses of using the
690 suite of trace element data to inform choices of groups for linear discriminant analysis to
691 classify the unknown samples from the KFTB. Unlike the PCA or hierarchical clustering analysis,
692 which do not require any a priori assumptions about the relation between samples, linear
693 discriminant analysis is a guided machine learning approach that uses a set of training data
694 divided into known groups to calculate the initial linear discriminant functions (Krzanowski,
695 2000). These functions are then used to classify unknowns as members of one of these preset
696 groups. We complete these calculations in the “R” software using the “MASS” library (Venables
697 and Ripley, 2002). We use the modern sediments and Vandam volcanoclastic rocks as the
698 training dataset to calculate the linear discriminant functions. We calculate multiple

699 discriminant functions, using the ILR transformed compositions with different group
700 assignments, which are described in more detail in the results section. To assess the robustness
701 of each set of discriminant functions, we perform cross-validation by iteratively recalculating
702 the discriminant functions with one sample from the training data excluded. This sample is then
703 classified according to the calculated discriminant function and the overall percentage of
704 correctly classified training data provides an indication of the robustness of the chosen groups
705 and the accuracy of the functions. Finally, the KFTB samples are classified using the calculated
706 linear discriminant functions.

707 ***5.1.3 Multivariate Characterization of Potential Source Areas***

708 Analyses of the ILR-transformed trace-element suite of potential source areas in terms
709 of both PCA (Figure 4a) and hierarchical clustering (Figure 4b) shows that rivers draining the GC
710 (GC, N=7) are generally geochemically distinct from both the 4 rivers draining the Lesser
711 Caucasus (LC, N=4) and the volcanic and volcanoclastic rocks in the Vandam zone (N=11). In
712 contrast, the Lesser Caucasus rivers and the Vandam zone rocks broadly overlap (Figure 4).
713 Thus, on the basis of trace element geochemistry and multivariate statistics we can define two
714 broad end-member sources. The first represents sourcing from the GC Interior and is
715 predominantly representative of the Jurassic-Cretaceous flysch, given the extent of the sampled
716 watersheds (Figure 1). The second represents sourcing from predominantly volcanic and
717 volcanoclastic rocks in either the LC arc or Vandam. Two Transcaucasus rivers plot between
718 these two end-member groups (Figure 4a): the Kvirila, which drains the Dzirula Massif (Figure
719 1), and the mid-basin Kura River, which incorporates drainages from both the GC and LC,
720 although both show more similarity with the GC Interior group than the LC arc/Vandam. Thus,

721 we consider the Transcaucasus rivers as a third broad group within the context of the PCA
722 results and return to this idea when considering the linear discriminant analysis in Section 5.1.4.

723 Both the PCA and clustering analysis reveal more subtle divisions within the two broad
724 groups and divide each into two separate sub-populations. For the LC-Vandam group, the
725 cluster analysis yields an identical subdivision into two subgroups as the PCA, for which the first
726 two principal components are able to account for ~70% of the variance (Figure 4a). For the GC
727 Interior group, the subdivision indicated by the cluster analysis (Figure 4b) is present but less
728 distinct in the PCA, with the mid-basin Kura River plotting between the main GC and LC-Vandam
729 groups (Figure 4a) as previously noted. In both PCA and the cluster analysis, Vandam sample
730 AB0863 is found to be an outlier. The subdivisions of the two main groups broadly correspond
731 to Si content with a boundary between the two being ~55 weight percent SiO₂. Thus, we refer
732 to the two sub-populations within each group as “High Si” and “Low Si”. In the GC Interior
733 group the Low Si member generally includes watersheds that drain more volcanic or
734 volcanoclastic components and/or that have significant amounts of carbonate, e.g., the Kish and
735 Aragvi rivers have CaO weight percent of 25% and 18%, respectively. We use these subdivisions
736 in the linear discriminant analysis that is considered in the next section.

737 It is important to note that while at the gross scale, the two broad geochemically
738 defined sources correspond to geographically distinct sources (i.e., the interior of the GC range
739 vs LC and Vandam), the subdivisions within each group lack a clear correlation with geographic
740 location. Specifically, for the GC affiliated rivers, there is no clear along-strike pattern in terms
741 of the two sub-populations. Likewise, for the LC-Vandam group, bedrock samples that are
742 differentiated into the two distinct groups come from outcrops only a few km from each other.

743 Thus we interpret these internal divisions to reflect geochemical heterogeneity in the sources,
744 but that this heterogeneity is not cross-correlated with either tectonic or geographic location.

745 ***5.1.4 Linear Discriminant Analysis to Classify Unknowns - Methods***

746 We use the four populations identified in the hierarchical clustering and PCA to define
747 initial groups for linear discriminant analyses (LDA) (Tables 8, 9). In detail we run 6 different
748 LDAs (LDA-1 through LDA-6), each of which use a different suite of initial groups as training
749 data. The 3 highest-performing LDAs have correct rates of classification from cross-validation of
750 >80% (Figure 5 and Table 6), similar to the methodology of Von Eynatten et al.,(2003). Here we
751 present results from 2 of these (LDA-1 and LDA-3) because there is no robust statistical or
752 geological reason to favor one over the other. We report the third high-performer (LDA-2) in
753 the supplement (Figure S13, S14) because it classifies the KFTB sandstones essentially the same
754 as LDA-1 and yields linear discriminant values that match LDA-3. We do not report the three
755 low-performing LDAs (LDA-4 to LDA-6) because they have correct classification rates from
756 cross-validation of only 40-70%. However, we note that one of the low-performing LDAs uses
757 geographically defined groups in which all Vandam volcanoclastic rocks define one group and all
758 Lesser Caucasus river sediments define another, thus highlighting that the two geographic
759 regions are not geochemically distinct.

760 The three high-performing LDAs all use groupings based on the results of the PCA and
761 clustering analysis, with the same groupings for the High and Low Si LC-Vandam groups but
762 different groupings for the GC Interior fields. Outlier Vandam sample AB0863 is excluded from
763 all LDAs (Figure 4). In LDA-1, the GC Interior group is divided as indicated by the cluster analysis
764 into the High and Low Si subgroups, with the mid-basin Kura included in the training data as

765 part of the Low Si group (Figure 5 and Table 6). In LDA-2, all of the GC Interior samples are
766 combined in a single group as indicated by the principal component analysis, with the mid-basin
767 Kura River excluded from the training dataset. LDA-3 is identical to LDA-2 except the mid-basin
768 Kura River is included as a separate group.

769 ***5.1.5 Linear Discriminant Analysis to Classify Unknowns - Results***

770 Results from applying LDA-1 and LDA-3 to the sandstone samples of unknown
771 provenance are reported in Figures 5 and 6 and Table 7. The most important observation from
772 the geochemical proxies are clear up-section changes in provenance, generally from a LC-
773 Vandam source to a GC interior source (Figure 6).

774 In LDA-1, the oldest sample in the Vashlovani section (V-15) groups with LC-Vandam
775 (High Si), with all younger samples classified as being derived exclusively from the GC Interior.
776 In contrast, all samples from the Sarica section are classified as having a predominantly LC-
777 Vandam source, except for the youngest sample (S-1735), which groups with GC Interior (Low
778 Si). In both cases there are no systematic up-section variations between High and Low Si
779 subgroups. Classification of the Xocashen section results in a LC-Vandam source for the lower
780 two samples and a GC Interior source for the upper three samples. Similarly, Bozdagh records a
781 LC-Vandam source for the lower three samples and a GC Interior source for the upper sample.
782 LDA-1 classifies the entire Goy section as being derived from the LC-Vandam source. Of note,
783 Goy is the only section where results from LDA-1 and LDA-2 differ significantly, with LDA-2
784 assigning the upper three samples to the GC Interior source (Figure S13, S14).

785 Classifying using LDA-3, which includes the mid-basin Kura River as a separate source,
786 produces similar results as LDA-1 and LDA-2 for some of the sections but dramatically different

787 results for others (Figure 5, 6, Table 7). Vashlovani and Sarica are again classified as dominantly
788 sourced from the GC Interior and LC-Vandam, respectively, although Sarica sample S-360 is
789 classified as similar to the mid-basin Kura River. In contrast, all Bozdagh samples are reclassified
790 as being similar to the mid-basin Kura River. Both Xocashen and Goy are partially reclassified,
791 resulting in alterations between GC Interior and Kura sources, although the lowest sample in
792 Xocashen remains as sourced from LC-Vandam.

793 ***5.1.6 Interpretation of Bulk Geochemistry In Context with Petrography***

794 While the bulk geochemistry is useful for both defining potential source areas and
795 classifying the KFTB sandstones within that context, it is somewhat abstract without a
796 mineralogic or petrologic context. To address this, we develop a comparison between the
797 geochemistry and the petrography of the foreland sediments by way of using the results of the
798 LDA presented in Section 5.1.4. In detail, we consider only the values of the first linear
799 discriminant (i.e., the x-axis in Figure 5) for the different LDAs. Because the decision boundaries
800 within the LDAs are nearly vertical, the first linear discriminant (LD1) is relatively effective as a
801 single numeric metric of source affinity. Specifically, we use LD1 of LDA-1 and LDA-2. We use
802 LDA-2 rather than LDA-3 because it is simplest to interpret the results of the petrography in the
803 context of LDA-2, which uses GC Interior, LC-Vandam High Si, and LC-Vandam Low Si source
804 divisions, whereas in LDA-3 the mid-basin Kura river source is effectively a mixture of the GC
805 Interior and LC-Vandam sources (Figure S13). It is possible to make this switch because the LD1
806 values of LDA-2 and LDA-3 are the same, making them largely interchangeable for this purpose.

807 To compare the LDA results to the sandstone petrography (Figure 7), we first perform a
808 random forest regression using the percentage of the point count components to predict the

809 value of LD1 for both LDA-1 and LDA-2. Random forest regression is a useful method for
810 assessing the importance of sets of multivariate data in contributing to a single variable, in this
811 case, the value of LD1 (e.g., Grömping, 2009). For each LDA, we use the results of the random
812 forest regression to identify the most important components from the sandstone petrography
813 and assess the extent to which they alone or in aggregate correlate to the LDA.

814 The random forest regression highlights that the 6 most important petrographic
815 components in LDA-1 are calcium rich plagioclase, pyroxenes & amphiboles, volcanic lithics,
816 total quartz, sedimentary lithics, and miscellaneous “other” (Figure 7a, S8). In detail, the
817 combined percentage of the first three components (calcium rich plagioclase, pyroxene &
818 amphibole, and volcanic lithics) is positively correlated with LD1, whereas the combined
819 percentage of the last three components (quartz, sedimentary lithic, and the generic “other”
820 grains) is negatively correlated with LD1 (Figure 7b, S8). This analysis is consistent with the
821 former three components broadly being associated with a LC-Vandam source and the latter
822 three components associated with a GC Interior source. For LDA-2, the random forest
823 regression is similar, but suggests that the two sources are each predominantly defined by only
824 2 components: calcium rich plagioclase and pyroxenes & amphibole for LC-Vandam source and
825 quartz and sedimentary lithic components for the GC Interior source (Figure 7c). These
826 components show the same positive and negative linear relationships with LD1 as in LDA-1, but
827 with higher correlation coefficients (Figure 7d).

828 Two details which are important to highlight in the comparison of the geochemistry and
829 petrography are that broadly; (1) the differentiation of LC-Vandam or GC Interior geochemical
830 sources reflect relative abundances of the petrographic components discussed above as

831 opposed to strict presence or absence of the relevant petrographic components and (2) the
832 petrographic components that are important in defining the two sources differ in their relative
833 chemical stability (e.g., Lasaga et al., 1994 and references therein). Specifically, the
834 petrographic components that are correlated with the LC-Vandam source (e.g., calcium
835 plagioclase, pyroxene) would be expected to weather more quickly than some of the
836 components that define the GC Interior (e.g., quartz). Thus, an apparent up-section change
837 from a LC-Vandam source to a GC Interior source could reflect a true change in sediment
838 provenance from these two broad geographic source regions or could be reflective of increased
839 weathering of a LC-Vandam like source. We consider these two options further in the
840 discussion in light of the results of detrital zircon U-Pb ages presented in the following section.

841 **5.2 U-Pb Detrital Zircon Ages**

842 ***5.2.1 Analytical Methods***

843 U-Pb geochronology of detrital zircons is a versatile tool widely used for assessing the
844 provenance of siliciclastic sediments (e.g., Fedo et al., 2003; Andersen, 2005; Gehrels, 2012).
845 We perform U-Pb geochronologic analyses of individual detrital zircons from samples of seven
846 Kura Basin sandstones via laser ablation multi-collector inductively coupled plasma mass
847 spectrometry (LA-MC-ICPMS) at the Arizona LaserChron Center. Analytical procedures relevant
848 at the time of analysis (2011) are described by Gehrels et al. (2006) and Gehrels et al. (2008).
849 Approximately 110 grains were dated per sample. Because the potential existed for observing
850 young grains (<10 Ma) in many of the samples, we used a 20 second integration time for all
851 samples. Analyses were excluded from plots and statistical treatments based on unacceptable
852 discordance, precision, or in-run fractionation. For extremely young grains (<10 Ma),

853 discordance was largely ignored in choosing whether to include or exclude particular analyses
854 because the calculated $^{206}\text{Pb}/^{207}\text{Pb}$ for these grains are subject to extremely low precision due
855 to the low concentrations of ^{207}Pb (Gehrels, 2012). Complete analyses are presented in the
856 supplement (Table S7)

857 To consider potential sources for the Kura Basin DZ samples, we also define composite
858 source populations based on the classification from Tye et al., (2020) as described in Section
859 2.3. Specifically, to define a composite source population we combined available published DZ
860 age populations from individual samples into a single, composite sample using the same set of
861 samples as Tye et al., (2020), including those from Allen et al. (2006), Wang et al., (2011),
862 Vincent et al., (2013), Cowgill et al., (2016), Trexler et al., (2022), Vasey et al., (2020), and Tye
863 et al., (2020), but supplemented with additional samples reported by Forte et al., (2022). For
864 the samples from Forte et al., (2022) not classified by Tye et al., (2020), we use
865 multidimensional scaling (Vermeesch, 2013) to assess which source samples, and by proxy
866 which composite source terrane, these newer samples are most similar to. Multidimensional
867 scaling plots suggest that all of the Forte et al., (2022) samples are best classified as part of the
868 GC siliciclastic composite source. Table 4 lists the samples used from these sources and to
869 which source terrain they are assigned. We also follow Tye et al., (2020) in tracking the 6
870 distinct age populations defined in Tye et al. and discussed in section 2.3 within both the
871 composite sources and basin samples.

872 **5.2.2 Statistical Methods**

873 For visualizing age distributions, we use both probability distribution plots (PDPs) and
874 kernel density estimates (KDEs), because both have distinct advantages and disadvantages (e.g.,

875 Saylor and Sundell, 2016). We use the “densityplotter” software (Vermeesch, 2012) to generate
876 both the PDPs and KDEs for the composite sources and our new samples. We use three
877 different methods to compare the U-Pb ages from our new basin samples with those from
878 potential source terranes: multidimensional scaling (MDS) plots (Vermeesch, 2013), Monte-
879 Carlo unmixing models (Sundell and Saylor, 2017), and Bayesian Population Correlation (BPC)
880 (Tye et al., 2019). Ultimately, the three different methods yield largely similar results, so for
881 simplicity, we focus on the results of the BPC as these are the easiest to quantitatively relate to
882 the results of classifying the sediments by their bulk geochemistry. The supplement contains
883 both methodological details and results of the MDS and Monte-Carlo unmixing models (see
884 Section S2.3). In the following we briefly review key aspects of the BPC method, with similar
885 details for the MDS and Monte-Carlo unmixing provided in supplement Section S2.3.1.

886 BPC relies on constructing probability model ensembles for each sample and then uses
887 these probability model ensembles in pairwise comparisons to calculate a degree of similarity,
888 i.e., the BPC value (Tye et al., 2019). As shown by Tye et al., (2019), BPC is relatively insensitive
889 to differences in sample size between samples being compared, removing the need for
890 subsampling as is required with unmixing techniques (e.g., Sundell and Saylor, 2017). Output
891 BPC values vary from 0 to 1, where a value near 1 implies a high degree of similarity. The BPC
892 calculation also estimates uncertainty on these values.

893 ***5.2.3 U-Pb Age Distributions***

894 We present PDPs and KDEs for both the 7 composite DZ sources (Figure 8) and 7 KFTB
895 DZ samples (Figure 9, S15) to enable visual comparison prior to statistical comparison below. It
896 is important to note that the definition of source terranes is different between the U-Pb detrital

897 zircons and the geochemical classifications, a point we return to in the discussion. The vast
898 majority of zircon ages within the thrust belt samples are Mesozoic and Paleozoic, although
899 there are some Cenozoic grains in the two Bozdagh samples (B-280 and B-875) and the lower
900 Sarica and upper Vashlovani samples (S-210 and V-1240, respectively). The only samples with
901 sizeable portions of Proterozoic and older grains are the lower Vasholvani sample (V-15) and
902 both those from Bozdagh (Figure 9, S15). Within the context of the 6 distinctive age populations
903 defined by Tye et al., (2020), the vast majority of samples are dominated by mixtures of <90 Ma
904 grains associated with the Lesser Caucasus arc, 90-200 Ma age grains associated with either the
905 Lesser Caucasus arc or GC rifting, or 200-380 Ma grains associated with the Variscan orogeny.
906 For all samples except V-15, older age populations make up less than 25% of the total grains.
907 Both S-210 and V-1240 are notable for containing statistically significant numbers of extremely
908 young grains with mean ages of 2.5 ± 0.24 Ma (n=3) and 2.66 ± 0.046 Ma (n=47), respectively,
909 which Forte et al., (2015a) used to determine maximum depositional ages. The sources of these
910 young grains are unknown, but they overlap in age with silicic volcanism in both the Lesser
911 Caucasus (Karapetian et al., 2001) and GC (Shcherbakov et al., 2022).

912 ***5.2.4 Statistical Comparisons of KFTB Sandstones with Sources***

913 We remove the populations of very young grains from samples S-210 and V-1240 prior
914 to conducting the statistical comparisons because these grains most likely reflect
915 contemporaneous, or nearly contemporaneous, regional volcanism at the time of deposition.
916 Because none of the composite sources have age populations of this age, including these grains
917 would effectively mask the provenance signature in the statistical methods we employ. That
918 problem is particularly acute for V-1240, because the young grains constitute nearly 50% of the

919 total population in this sample. We present the results of the BPC comparison (Figure 10) from
920 west to east. Results of the MDS and Monte-Carlo unmixing are presented in the supplement
921 (Figure S16)

922 In the BPC comparison (Figure 10), the two Vashlovani samples have the highest degree
923 of similarity with the GC siliciclastic source, along with elevated similarity with the eastern GC
924 volcanoclastic, GC basement, and Transcaucasus basement-LC arc sources. In detail, the second
925 highest similarity in V-15 is to the eastern GC volcanoclastic source, whereas in V-1240 it is to
926 Transcaucasus basement-LC arc. Both Sarica samples show only a strong similarity with eastern
927 GC volcanoclastic (>0.9), with the next highest similarity being Transcaucasus basement-LC arc
928 (<0.6). Both Bozdagh samples are very similar to the Transcaucasus basement-LC arc source
929 (>0.9), but also show some similarity with the GC siliciclastic source (>0.7). Finally, the G-200
930 sample from Goy is very similar to the eastern GC volcanoclastic source (0.98), with the next
931 similar sources being GC siliciclastic and Transcaucasus basement-LC arc (both <0.7).

932 Taken together, the results of BPC, MDS, and Monte-Carlo unmixing are broadly
933 consistent with each other (Figure 10, S16). All methods indicate a close correspondence
934 between samples from the same section, with samples from the top and bottom of the same
935 section being more generally similar to one another than to samples from different sections,
936 even if those samples are more closely time-equivalent (Figure S15). In addition, the three
937 methods indicate broadly consistent sources for the individual samples, although there are
938 some exceptions. Vashlovani and Bozdagh show both the most complicated sourcing and the
939 largest amount of disagreement between the methods. For Vashlovani, all methods indicate
940 significant contributions from GC siliciclastic and GC basement, but vary in the extent to which

941 they include eastern GC volcanics or Transcaucasus basement and LC arc. All three
942 methods indicate Transcaucasus basement-LC arc as the primary source for Bozdagh, with
943 some minor inputs from other sources, including GC siliciclastic, eastern GC volcanics, and
944 western GC volcanics, although the proportions or importance of these vary between
945 methods. In contrast, in both Sarica and the lower Goy sample, all methods consistently
946 indicate nearly exclusive sourcing from the eastern GC volcanics source (Figure 10, S16).

947 **6. DISCUSSION**

948 **6.1 Reconciling Differing Results of Geochemical and Detrital Zircon Provenance Methods**

949 The most fundamental result of this study is that the geochemical/petrographic and DZ-
950 based approaches yield provenance interpretations for the KFTB sandstones that diverge in
951 meaningful ways for several of the measured sections. The geochemical/petrographic proxies
952 indicate clear up-section changes in provenance from a LC-Vandam source to a GC interior
953 source (Figure 6). In contrast, DZ-based methods generally suggest limited up-section change
954 (Figure 9, 10). Thus, if taken in isolation, each method leads to a different interpreted
955 provenance - and potentially tectonic - history for the Kura basin and GC. To reconcile these
956 apparently divergent results, it is necessary to explain why the results from the two methods
957 differ.

958 Interpreting the apparent divergence in KFTB sandstone provenance is complicated by
959 the fact that the definitions of the source terranes that naturally emerge from each dataset
960 differ from one another. As a result, there is no single set of source terranes that suitably
961 explains the results from both of the different methods. Specifically, Tye et al., (2020) find that
962 5 statistically distinct sources within the GC emerge from the U-Pb DZ ages (Pre-Jurassic

963 sedimentary, GC basement, GC siliciclastic, eastern GC volcanics, western GC
964 volcanics) and that samples sourced from volcanic/volcanic rocks in the LC
965 (Transcaucasus basement-LC arc source) can be distinguished from those in the GC (eastern and
966 western GC volcanics sources, Figure 8, 10). In contrast to the 5 sources that emerge from
967 the DZ analyses, our sampling of similar regions using bulk geochemistry yields a maximum of 4
968 statistically distinct sources within the combined GC and LC and also fails to distinguish Jurassic-
969 Cretaceous volcanic/volcanic sources within the GC from those in the LC (Figure 4, S10).

970 To explore the cause underlying the apparent divergence in provenance from the
971 different methods, we first consider the relationships, commonalities, and differences within
972 the definitions of source terranes between the DZ and geochemical approaches and clarify how
973 these do, or do not, relate to each other. We then consider how the source-definitions map
974 into implications for the sourcing of the KFTB sandstones before providing a parsimonious
975 explanation for the apparent disagreement.

976 **6.1.1 Source Definitions**

977 The primary difference between the the DZ and geochemical approaches is a difference
978 in the degree of geographic specificity, with the DZ approach providing more geographic
979 granularity than the geochemical/petrographic approaches. The DZ data permit identification of
980 sediment sourcing from specific geographic areas within the Caucasus region that are not
981 distinguishable geochemically. For example, the DZ method has the ability to differentiate
982 contributions to a KFTB sandstone from the southeastern GC range front to the northeast (i.e.,
983 eastern GC volcanics source) vs. the southwestern GC range front to the northwest (i.e.,
984 western GC volcanics source) vs. from the LC to the south (i.e., Transcaucasus Basement-LC

985 Arc source) (e.g., Figure 1 - Tye et al., 2020). In contrast, contributions from these regions are
986 indistinguishable from one another geochemically or petrographically, and would all broadly
987 appear as coming from a single composite LC-Vandam source (Figure 4). The apparent
988 homogeneity of the LC-Vandam source in the geochemical data is consistent with prior
989 suggestions of a genetic link between the LC Arc and the volcanic and volcanoclastic rocks within
990 the GC, and specifically the Vandam (e.g., Kopp and Shcherba, 1985). However, in the context
991 of interpreting provenance within the adjoining foreland, this similarity limits the geographic
992 specificity of geochemical and petrographic classifications. Another example is the ability of the
993 DZ method to identify sourcing of a KFTB sandstone from the interior of the western GC, which
994 would be indicated by contributions from either the Pre-Jurassic sedimentary or GC basement
995 sources (e.g., Figure 1 - Tye et al., 2020), whereas sourcing from anywhere in the interior of the
996 range appears in the geochemical or petrographic data as a generic GC Interior source without
997 the capacity for further geographic clarification (i.e., western vs eastern GC, Figure 4).
998 Unfortunately, attempts to extract more geographic information by considering the sub-
999 populations of the geochemical sources, i.e., the High Si and Low Si sub-populations of both the
1000 GC Interior and LC-Vandam sources (Figure 4) are not successful.

1001 The non-overlapping source definitions within broad geographic regions (e.g., all of the
1002 GC associated DZ sources vs the two geochemical/petrographic GC sources) are mostly simply
1003 explained in terms of lithologic heterogeneity and the sensitivity of the different methods to
1004 that heterogeneity. For example, the Aragvi, Kish, and Damiraparan Rivers within the GC all
1005 contain, or are directly adjacent to, samples classified as being part of the GC siliciclastic DZ
1006 source, but span both GC affiliated geochemical sources, with the Aragvi and Kish Rivers being

1007 part of the Low Si GC Interior source whereas the Damiraparan River is part of the High Si GC
1008 Interior source. Much of these differences likely reflect variable geology within the source
1009 catchments, e.g., both the Aragvi and Kish rivers have high CaO (compared to the
1010 Damiraparan), suggesting that in this case the divergence in geochemical classifications may in
1011 part reflect the presence or absence of significant carbonate, a characteristic that would not be
1012 detectable with detrital zircon geochronology. Similar patterns are observed in the Lesser
1013 Caucasus and/or Vandam associated sources. At the individual river level, both the Tovuz and
1014 Mtkvari River were classified as a part of the Transcaucasus Basement and Lesser Caucasus Arc
1015 source on the basis of their U-Pb ages, and while they geochemically are both categorized as a
1016 LC-Vandam source, the Mtkvari is contained within the Low Si subpopulation whereas Tovuz is
1017 contained within the High Si subpopulation. Similarly, bedrock samples defined geochemically
1018 as either of the LC-Vandam sources are contained within watersheds of catchments from which
1019 modern sediment U-Pb age populations were used by Tye et al., (2020) to define the eastern
1020 GC volcanoclastic source. This includes bedrock sample AB0862, which geochemically is
1021 classified here as from the High Si source, but whose DZ population is part of the samples used
1022 to define the eastern GC volcanoclastic DZ source (Cowgill et al., 2016; Tye et al., 2020).

1023 Petrography on some of the samples from the Vandam region in the GC does not reveal
1024 distinguishing characteristics for interpreting geographic, or other information from the LC-
1025 Vandam sub-populations (Figure 4, Tables 4, S2). Both geochemical populations span samples
1026 that are texturally volcanic compared to volcanoclastic and the clast counts and/or modal
1027 mineralogy do not reveal systematic differences. The only clarifying detail from the sandstone
1028 petrography of the Vandam volcanoclastic samples relates to AB0863, which is an outlier in all

1029 geochemical classifications. Compared to the other bedrock samples, AB0863 is completely
1030 devoid of calcium rich plagioclase and has relatively low amounts of pyroxene or amphibole,
1031 instead being dominated by albite and potassium and/or alkali feldspar. This would broadly
1032 suggest that the calcium rich plagioclase, pyroxenes, and amphiboles that are largely absent
1033 from AB0863 are important in terms of defining both of the LC-Vandam subgroups from a bulk
1034 geochemical perspective.

1035 ***6.1.2 Intercomparison of DZ and Geochemical Methods in KFTB Samples***

1036 Given the apparent divergence between provenance trends for the KFTB sandstones
1037 from geochemistry (Figure 5, 6) and DZ (Figure 9, 10), it is instructive to consider direct
1038 comparisons between these two methods. For this purpose, we develop an approach for
1039 sample-to-sample comparison using the linear discriminant analysis of the geochemical data
1040 and the Bayesian population correlation of the DZ data (Figure 15), similar to how we compared
1041 the bulk geochemistry and petrography results (Section 5.1.5). For the geochemistry-DZ
1042 comparison, we compare the first linear discriminant of LDA-1 and LDA-2 directly to the BPC
1043 value for the eastern GC volcanoclastics, GC siliciclastic, and Transcaucasus basement and LC arc
1044 sources, as these are most diagnostic in the DZ comparison statistics we considered (e.g., Figure
1045 10, S16).

1046 Comparing the LDA results and those from detrital zircon suggests relatively little
1047 relationship between the two (Figure 11). Specifically, sample pairs from measured sections
1048 that have a large difference in their linear discriminant value (i.e., different provenance source
1049 up section) do not necessarily have large differences in their BPC values for relevant sources.
1050 Depending on the particular DZ source considered, small trends can be observed, e.g., a

1051 positive correlation between eastern GC volcanoclastic BPC and LDA-1 and a negative
1052 correlation between GC siliciclastic BPC and LDA-1 for Vashlovani, but the magnitudes of the
1053 BPC differences are small compared to differences between sections, e.g., Sarica compared to
1054 Vashlovani. This comparison also highlights a similar, and important, result from comparing the
1055 geochemical and U-Pb DZ classification of the source terranes, which is that samples can have
1056 strongly similar geochemical affinities but have different DZ sources, as is the case for the
1057 sample at the top of Sarica (S-1735) and the 2 Vashlovani samples (V-15, V-1240) (Figure 11).

1058 ***6.1.3 Mechanism for Provenance Method Divergence***

1059 While there are important nuances as discussed in the prior sections, broadly the
1060 comparisons between the bulk geochemistry and detrital zircon U-Pb geochronology from
1061 samples of both known (i.e., source areas) and unknown provenance (i.e., the KFTB sandstones)
1062 suggest that the two provenance methods indicate a potentially different history of sourcing for
1063 KFTB sandstones. Specifically, in terms of the bulk geochemistry, most of the locations exhibit
1064 an up-section shift from a predominantly LC-Vandam source to a more GC Interior dominated
1065 source. In contrast, the detrital zircon analyses from the top and bottom of select sections do
1066 not as clearly or consistently show significant changes up section (Figure 9, 10, S16). There are
1067 several possible explanations for this disagreement, including (1) sediment recycling and
1068 selective weathering within the foreland basin; (2) climatically mediated preferential
1069 weathering of unstable components; (3) the non-unique source characterizations via different
1070 methods described in the previous sections; (4) sensitivity of different provenance methods to
1071 different components within the samples; or (5) biasing of detrital zircon signatures by spatial
1072 variable erosion, fertility of source terranes, or other filtering processes. The following discusses

1073 the first option, which we favor as the primary explanation because the other four options do
1074 not fit with the available data, as the supplement explains (Section S3). In exploring the cause of
1075 the apparent discrepancy, we largely focus on understanding the variation in the Sarica section,
1076 as it is the most extreme.

1077 In detail, our preferred explanation is that the provenance signatures largely reflect an
1078 up-section increase in sediment recycling, such that the sediment source transitions from first-
1079 cycle (or initially less-recycled) material eroded from the GC to increasing fractions of recycled
1080 versions of this same material as the KFTB developed. Of particular importance is that the
1081 primary components that appear to define the LC-Vandam sources mineralogically and
1082 geochemically, e.g., calcium rich plagioclase, pyroxene, and amphibole (Figure 7, S8), are also
1083 species that are expected to weather at rates several orders of magnitude faster than
1084 components that define the flysch source, e.g., quartz (e.g., Lasaga et al., 1994 and references
1085 therein). The potential importance of chemical weathering of these components is also
1086 consistent with prior work in the GC region, where Morton (2003) highlighted the importance
1087 of dissolution of clinopyroxene and amphiboles in Productive Series sediments in terms of
1088 considering potential sourcing. Thus, in the Sarica section, we envision a scenario where the
1089 base of the section was deposited prior to fold-thrust development and was sourced from the
1090 GC with a mixture of both GC Interior and LC-Vandam sources, although the DZ-data indicate
1091 the LC-Vandam type source likely dominated, which is a point we return to in section 6.2. As
1092 portions of the fold-thrust belt north of the Sarica section began to deform they progressively
1093 became a source of recycled sediment for the Sarica region. Specifically, early thrusts within the
1094 KFTB exposed rocks of a similar provenance to what is seen at the base of Sarica, causing them

1095 to be weathered, eroded, and transported prior to deposition at the site of the Sarica section
1096 and resulting in the preferential breakdown of the unstable components that are particularly
1097 indicative of the volcanic/volcaniclastic source in the geochemical/petrographic data. As a
1098 result, fewer of these volcanic/volcaniclastic components are preserved up section, resulting in
1099 the up-section shift geochemical signatures that is mirrored in the petrography, e.g., Figure 7,
1100 S8). However, the zircon signature from these recycled sediment remains effectively the same
1101 as the original source material from the GC. Additionally, growth of KFTB topography to the
1102 north of Sarica would likely begin diverting GC sourced rivers, limiting influx of new detrital
1103 zircons into the section. This explanation is also broadly consistent with the up-section
1104 increases in chemical index of alteration (CIA – see supplement sections S2.2.3 and S2.2.5)
1105 values seen in Sarica and the majority of the other sections, although the CIA values do not
1106 suggest deep weathering even at their most extreme (Figure 6, S12). Because sandstone
1107 petrography and geochemistry data from the Xocashen and Goy sections exhibit similar up-
1108 section trends as Sarica, we infer they also record recycling and a transition from a GC source to
1109 one that is more locally derived from within the KFTB. However, without comparable DZ data in
1110 Xocashen or Goy, this hypothesis is less definitive and highlights a need for future work.

1111 While we argue that sediment recycling is important for interpreting the provenance
1112 signature in the majority of our KFTB sections, it may not be dominant in all sections, as
1113 indicated by minimal apparent provenance discrepancies between geochemical and DZ
1114 methods. In particular, we interpret both the Bozdagh and Vashlovani sections to reflect limited
1115 recycling. For Bozdagh, geochemistry, sandstone petrography, and U-Pb detrital zircon
1116 populations all combine to indicate a similar history of sourcing and no change in the degree of

1117 recycling, consistent with the relatively constant CIA values throughout the section (Figure 6, 9,
1118 10). Likewise, we interpret the Vashlovani section as recording minimal changes in the degree
1119 of recycling because in this case the geochemical and DZ-data both indicate a change up-
1120 section that reflects a progressively diminishing LC-Vandam source. These observations from
1121 Bozdagh and Vashlovani are a major reason why we prefer sediment recycling as the
1122 mechanism to explain the apparent discrepancies in provenance data as opposed to a
1123 climatically mediated, regional increase in chemical weathering rates (i.e., the second option),
1124 because this latter option predicts up-section changes in the Bozdagh and Vashlovani section
1125 that we do not observe.

1126 **6.2 Implications for Greater Caucasus and Kura Fold-Thrust Belt Tectonics**

1127 To provide a framework within which to consider the evolution of sediment provenance
1128 in the KFTB, Figure 12 presents a visualization of changes in sourcing through time and space.
1129 For this purpose, we consider the spatial distribution of indicators of sediment provenance
1130 during individual regional stages between the Meotian and Bakunian, integrating additional DZ
1131 samples from Tye et al., (2020) where relevant. For each time period in Figure 12, and for each
1132 section that has data for that time period, we show the relevant portion of the LDA
1133 classification (bars - Figure 6) and the dominant DZ sources (stars - Figure 10, S16). None of the
1134 samples from Tye et al., (2020) appear within the map area of Figure 12, but we show what DZ
1135 provenance is indicated for samples either west or east along-strike within the KFTB at relevant
1136 time periods. Where appropriate we consider the degree of BPC similarity between KFTB
1137 samples from this study and those from prior work (see Supplement Section S2.3.3 and Figure
1138 S17). Below, we summarize our preferred interpretation of the implications of the provenance

1139 for GC and KFTB tectonics, with a focus on the across-strike traverse of sections from Sarica,
1140 Xocashen, and Bozdagh (Figure 12).

1141

1142 **6.2.1 Meotian-Pontian (7.65 – 5.33 Ma)**

1143 Vashlovani is the only location within our measured sections that includes a record of
1144 the Meotian-Pontian. This portion of Vashlovani records a mixed GC Interior and LC-Vandam
1145 source, specifically with a DZ signature that reflects a mixture of the eastern GC volcanoclastic,
1146 GC siliciclastic, and GC basement. There is some indication of a potential up-section reduction
1147 of the LC-Vandam component during Meotian-Pontian time from the petrography and
1148 geochemistry. At present, exposures of volcanic or volcanoclastic rock are very limited along the
1149 GC range front directly north of Vashlovani (Figure 1). Abundant volcanic/volcanoclastic sources
1150 during deposition of the Vashlovani base may indicate that exposures of these
1151 volcanic/volcanoclastic rocks were larger during Meotian-Pontian time than at present or that
1152 concentrations of volcanic/volcanoclastic components were enhanced via either focused erosion
1153 of units with similar exposure as today or lateral transport from areas of the GC range front that
1154 expose more of these units.

1155 Outside of the sections, at the western (CF-2) and eastern (EF-5) tips of the KFTB,
1156 undifferentiated Meotian-Pontian and Pontian sediments, respectively, record a predominantly
1157 GC interior source with a GC siliciclastic DZ signature during this time period (Tye et al., 2020).
1158 Without a clear sense of where, stratigraphically, CF-2 is located with respect to the Meotian-
1159 Pontian samples within Vashlovani, it is difficult to compare the implications of the differences
1160 between the sourcing of this sample, but for EF-5, given its Pontian depositional age, suggests a

1161 more exclusively GC Interior type source compared to Vashlovani during the same approximate
1162 time period. At the western terminus of the KFTB and considering sample CF-1 from the middle
1163 Miocene that precedes the Meotian-Pontian, we see a potentially similar up-section change
1164 from a more LC-Vandam source (CF-1) to more GC Interior dominated source (CF-2) (Tye et al.,
1165 2020). Importantly however, based on BPCs presented by Tye et al., (2020), CF-1 seems more
1166 similar to a Lesser Caucasus (Transcaucasus basement and LC arc) derived source than either of
1167 the GC volcanic or volcanoclastic DZ sources (i.e., the eastern and western GC volcanoclastics).
1168 Tye et al., (2020) suggest that the presence of a Lesser Caucasus affiliated source in CF-1
1169 reflects material that was deposited more distally to the Greater Caucasus, with the present
1170 position resulting from subsequent translation toward the GC via north-directed underthrusting
1171 of Kura Basin lithosphere beneath the GC. This remains a viable and likely hypothesis. However,
1172 given the clear geochemical relationships between the Lesser Caucasus volcanics and
1173 volcanoclastics and those exposed at least in the eastern GC (e.g., Figures 4, S8), an alternative
1174 hypothesis is that there was sufficient variability in a formerly larger thrust slice of volcanic and
1175 volcanoclastic material within the GC range front that zircons sourced from this thrust sheet
1176 could in part look more like those preserved in the surficial Lesser Caucasus today. While
1177 speculative, the general expectation of a shared tectonic history between the Jurassic-
1178 Cretaceous volcanic and volcanoclastic rocks exposed in the modern LC and the modern
1179 southern GC (Kopp and Shcherba, 1985), opens the possibility that a more complete section of
1180 the LC arc-Vandam rocks might contain larger age suites than in the tectonically isolated, and
1181 geographically separated, sections we observe today. More detailed stratigraphy in the region
1182 around the Gombori Range, specifically paleo-current measurements, could help to

1183 differentiate these two mechanisms, i.e., do the strata from which the CF-1 sample comes
1184 record dominantly south-directed (GC sourced) or north-directed (LC sourced) paleocurrents?
1185 Similarly, a better sense of the volcanic stratigraphy within the Jurassic and Cretaceous Lesser
1186 Caucasus could provide an indication of whether there are regions characterized by single-age
1187 DZ peaks, similar to the volcanic and volcanoclastic sources within the GC.

1188 Deposition in Vashlovani and elsewhere during the Meotian-Pontian (~7 to 5.5 Ma) is
1189 coincident with increases in exhumation rate observed throughout the GC between ~10-5 Ma
1190 (e.g., Avdeev and Niemi, 2011; Vincent et al., 2020; Forte et al., 2022; Tye et al., 2022). This
1191 similarity of timing is broadly consistent with the idea that the onset of rapid exhumation of the
1192 GC prior to the Meotian-Pontian had established the GC as a dominant sediment source for
1193 regions within the southern foreland (e.g., Tye et al., 2020).

1194

1195 ***6.2.2 Productive Series (5.33 – 2.95/2.7 Ma)***

1196 Both the Vashlovani and Sarica sections preserve portions of the Productive Series, but
1197 they suggest relatively different sourcing at this time (Figure 12b). Vashlovani records a
1198 dominantly GC Interior source with some limited LC-Vandam input remaining. In contrast,
1199 Sarica is almost exclusively sourced from LC-Vandam with an eastern GC volcanic detrital zircon
1200 signature. Present-day catchments north of Sarica within the GC reflect mixtures of the volcanic
1201 and flysh bedrock, so the dominance of LC-Vandam input in the Productive Series within Sarica
1202 appears to require greater proportions of this source at the time of deposition than is seen
1203 today, similar to the lower part of Vashlovani. Again, explanations for this pattern are either a
1204 physically larger exposure of the volcanic and volcanoclastic source within the southern range

1205 front at the latitude of Sarica, enhanced erosion of this source during Productive Series time, or
1206 lateral transport from an area of the GC range front with larger exposures of volcanic rocks.

1207 Near the eastern terminus of the KFTB, Productive Series sample EF-6 from Tye et al.,
1208 (2020) records a mixed affinity with both Lesser (Transcaucasus basement and LC arc) and GC
1209 (GC siliciclastic) DZ sources, but here we consider whether EF-6, like its central KFTB
1210 counterparts, might instead reflect sourcing from the GC, not the LC. Tye et al., (2020)
1211 interprets the Transcaucasus basement and LC arc component to reflect eastward transport of
1212 Lesser Caucasus material, either directly from the Lesser Caucasus via an axial drainage or
1213 erosion of Kura Basin sediments, most likely related to the coincident draw down of the Caspian
1214 Sea (e.g., Popov et al., 2006, 2010; Krijgsman et al., 2010; Forte and Cowgill, 2013; van Baak et
1215 al., 2017) and resulting incision by the Kura River (e.g., Kroonenberg et al., 2005). However, at
1216 present, both Vashlovani and Sarica are at a greater distance from the GC range front than EF-6
1217 (e.g., Figure 1, 13) and thus it is strange that EF-6 would reflect transport from the Lesser
1218 Caucasus or incised Kura Basin sediments while both Vashlovani and Sarica were dominantly
1219 sourced from the GC at this same time. Tye et al., (2020) largely follows suggestions from
1220 Morton et al., (2003) of a paleo-Kura river almost exclusively sourced from the Lesser Caucasus
1221 and that was located relatively near the GC range front, but this contradicts evidence of an
1222 entrenched Kura paleo-canyon near the modern axis of the basin during Productive Series time
1223 (e.g., Kroonenberg et al., 2005). In detail, the interpretation of a LC source for eastern Kura
1224 Basin Productive Series sandstones from Morton et al., (2003) relies primarily on the presence
1225 of unstable components within the heavy mineral assemblages of these samples, including
1226 abundant clinopyroxene, amphibole, and epidote. The similarity between these assemblages

1227 and the modern and paleo-Kura River sourced Productive Series sandstones led Morton et al.,
1228 (2003) to argue that the Productive Series sandstones necessarily must be sourced from the
1229 Lesser Caucasus. Morton et al., (2003) do report heavy mineral assemblages from rivers
1230 draining the eastern tip of the GC that contain significant proportions of amphibole, epidote,
1231 and clinopyroxene, but in lesser amounts than in the modern Kura River, with more stable
1232 minerals (e.g., feldspar, quartz) dominating the extreme eastern GC assemblages. Morton et al.,
1233 (2003) attribute the higher abundance of stable minerals in the GC rivers to the presence of
1234 Jurassic and Cretaceous sediments within the catchments and suggest that the presence of the
1235 unstable minerals may be due to recycling of Paleo-Kura sourced Productive Series sediments
1236 from portions of the river catchments containing these rocks. However, our analysis suggests
1237 that the Vandam domain of the southeastern GC proper also may contribute to these heavy
1238 mineral assemblages indicative of more mafic, less evolved source terranes, as such, the
1239 underlying association of these unstable components necessarily with a LC source, at least on
1240 the basis of heavy minerals alone, is questionable.

1241 To fully reconcile the apparently contradictory results of a potential sourcing of central
1242 KFTB sandstones during Productive Series time from the southern margin of the GC coincident
1243 with eastern KFTB sandstones from the LC would require; (1) palinspastic restoration of the
1244 positions of the Sarica, Vashlovani, and EF-6 locations during Productive Series time – in turn
1245 requiring estimates of shortening within the respective regions of the GC and KFTB, (2)
1246 constraint on the location of the GC range front along-strike during Productive Series time, and
1247 (3) ideally some independent constraint on the first order drainage-network structure within
1248 the foreland basin during Productive Series time beyond the location of the trunk Kura River.

1249 Generally, none of these details are sufficiently constrained to fully resolve this question.
1250 However, we again highlight that larger-than-present exposures of a former
1251 volcanic/volcaniclastic source in the GC with more zircon age variability than observed today
1252 provides an alternative and parsimonious explanation for the provenance records from EF-6.

1253 Focusing on the Sarica and Vashlovani sections, we interpret the dominance of GC
1254 provenance and the coarseness of the Productive Series deposits to result from continued rapid
1255 exhumation of the GC and progradation of coarse clastic materials into the foreland basin (e.g.,
1256 Burbank et al., 1988; Allen and Heller, 2012). The depositional character of these deposits also
1257 likely reflects the regional context of the coincident Caspian Sea lowstand (e.g., Forte et al.,
1258 2015a). The one Productive Series sample from Vashlovani is notable for being largely devoid of
1259 lithic grains (Figure S8, S9) and a temporary increase in CIA (Figure 6), both of which are
1260 consistent with an increase in reworking or weathering. This could reflect local reworking
1261 resultant from deformation and uplift of Kura Basin sediments, i.e., initiation of the KFTB, but
1262 given that these changes are short lived and that overlying basal Akchagylian sediments look
1263 very similar to underlying upper Meotian-Pontian sediments in Vashlovani (e.g., Figure 6, S8,
1264 S9), we favor an explanation related to the unique Caspian low-stand during the Productive
1265 Series deposition and potentially increased weathering during this period.

1266

1267 **6.2.3 Akchagylian (2.7/2.95 – 2.1 Ma)**

1268 The Akchagylian is present in the Vashlovani, Sarica, Xocashen, and Goy sections (Figure
1269 12c). With the exception of Vashlovani, all sections show a strong affinity for the LC-Vandam
1270 sources near their base and with Goy specifically showing affinity to an eastern GC

1271 volcaniclastic DZ source. In both Sarica and Goy, up-section toward the Apsheronian boundary,
1272 there is a slight decrease in this LC-Vandam source as indicated by petrography and
1273 geochemistry. This is not seen within Xocashen, but the Akchagylian-Apsheronian boundary is
1274 not captured within our sampled stratigraphy there. Similar to other sections, the base of Goy
1275 shows a strong affinity with a LC-Vandam source both geochemically (Figure 6, S11) and in
1276 terms of detrital zircons (Figures 9, 10, S16), which is at odds with modern geology because the
1277 portion of the GC range front north of Goy is an embayment largely devoid of volcanic and
1278 volcaniclastic material. As noted above, possible explanations for this difference are larger past
1279 exposures of the volcanic and volcaniclastic source within the southern range front, enhanced
1280 erosion of this source during Akchagylian time, or lateral transport from an area of the GC
1281 range front with larger exposures of volcanic rocks.

1282 In Sarica, a marked decrease in LC-Vandam components that is especially noticeable in
1283 the sandstone petrography (Figure S8) but also detected geochemically (Figures 6, S11) could
1284 reflect either (1) a decrease in the contribution of volcanic and volcaniclastic inputs reflecting a
1285 decrease in the importance of this source within the GC at the longitude of Sarica or (2) the
1286 beginning of sediment recycling reflective of initiation of KFTB structures north of Sarica and
1287 reduction in the volcanic and volcaniclastic component through weathering of unstable phases
1288 as described previously. Presumably, detrital zircon ages from this horizon would help to
1289 constrain these options, i.e., if the DZ signature remained dominated by eastern GC
1290 volcaniclastic zircons this would suggest sediment recycling, whereas if the DZ signature began
1291 to reflect more GC siliciclastic or other non-volcanic GC inputs, this would support a decreasing
1292 extent of an eastern GC volcaniclastic source along the southern range front. In the absence of

1293 such data, we instead consider the regional tectonic context of the KFTB to help narrow the
1294 options. Farther west within the KFTB, the Akchagylian may reflect the initiation of deformation
1295 (e.g., Sukhishvili et al., 2021), but the potential time range also includes much of the
1296 Apsheronian (e.g., Figure 2). Similarly, Vashlovani during the Akchagylian, which is in a
1297 somewhat similar structural position within the KFTB as Sarica, seems to still record sourcing
1298 from the GC as opposed to more local KFTB, i.e., recycled GC, sources. This is exemplified by the
1299 geochemistry (Figures 6, S11) and detrital zircon (Figure 9, 10, S16) sample(s) during the
1300 Akchagylian reflecting a consistent change up-section to a reduced LC-Vandam input, and
1301 sandstone petrography that still suggest LC-Vandam clastic inputs (Figure 4). Thus, for Sarica,
1302 we favor an explanation for provenance during the Akchagylian as still recording sourcing
1303 primarily from the GC. This would imply that the timing of KFTB initiation at the longitude of
1304 Sarica likely occurs after the Akchagylian and that the change in provenance from the
1305 Productive Series to Akchagylian, reflects a reduction in flux of the LC-Vandam source area from
1306 the GC.

1307

1308 ***6.2.4 Apsheronian (2.1 – 0.8 Ma) and Bakunian***

1309 The Apsheronian is represented in all measured sections (Figure 12e), though the extent
1310 of its exposure in Vashlovani is uncertain considering the unclear boundary between the
1311 Akchagylian and Apsheronian in this location (Figure 2). Through the duration of the
1312 Apsheronian, geochemistry and sandstone petrography suggest that Sarica, Xocashen, and
1313 Bozdagh all show decreases in LC-Vandam components. This is also broadly coincident with an
1314 up-section coarsening in all three columns. However, in Xocashen much of that coarsening

1315 occurs after the Apsheronian, during the Bakunian period, and the coarsening in Bozdagh is not
1316 as pronounced as in the other two sections. For both Sarica and Xocashen, we interpret these
1317 up-section changes in the stratigraphic character as most likely reflecting initiation of the KFTB.
1318 For Sarica, this would suggest that structures north of the section location likely began to
1319 exhume sometime during the early Apsheronian (Unit S3) or possibly across the Akchaglyian-
1320 Apsheronian boundary, similar to the timing of initiation of deformation in the Goy region
1321 (Forte et al., 2013; Lazarev et al., 2019). For Xocashen, coarsening and reduction in the LC-
1322 Vandam associated component occurred later in the Apsheronian and/or into the Bakunian
1323 compared to Sarica. This later timing in Xocashen could reflect either a delay related to coarse
1324 clastic progradation or that the Sarica fold itself, which is the structure directly north of and
1325 across the Adjinour playa from Xocashen, initiated and began to exhume, providing material for
1326 southern regions. In the latter case, this would suggest in-sequence propagation, from the
1327 structure north of Sarica during the early Apsheronian followed by Sarica during the later
1328 Apsheronian and into the Bakunian (Figure 13).

1329 It is worth noting that the degree of synchronicity of significant up-section coarsening
1330 and the reduction in the LC-Vandam component vary between Xocashen and Sarica. The two
1331 events roughly correspond in Xocashen, i.e. across the Unit X2-X3 / Apsheronian-Bakunian
1332 boundary, whereas in Sarica the coarsening starts across the Unit S3-S4 boundary (roughly early
1333 to middle Apsheronian) whereas the reduction in the LC-Vandam component occurs closer to
1334 the Unit S4-S5 boundary (later Apsheronian). For Sarica, it is unclear if the up-section
1335 coarsening or the LC-Vandam reduction better times the initiation of structures within the KFTB
1336 to the north. We favor up-section coarsening as being most diagnostic of thrust belt initiation

1337 because we assume that the onset of significant weathering is likely to temporally lag behind
1338 the transition to coarse sediment arrival from the uplift of structures to the north, in which case
1339 the KFTB initiated at this latitude around the Akchagylian-Apsheronian boundary (~2.1 Ma).
1340 However, if the reduction in LC-Vandam more precisely dates initiation, then onset here is
1341 closer to ~1 Ma. Ultimately, distinguishing between these options likely requires additional
1342 detrital zircon geochronology within Sarica, additional stratigraphic observations of areas within
1343 the KFTB north of Sarica, and more precise chronologies of all strata.

1344 While Bozdagh shows a reduction in LC-Vandam source components and a slight
1345 coarsening upwards, the interpretation of a relatively constant deltaic environment with
1346 Transcaucasus basement and LC arc DZ signatures at both the top and bottom of the section do
1347 not further constrain KFTB initiation. Instead, we interpret the facies and provenance data to
1348 indicate that the Bozdagh section was likely sourced by an east-flowing, longitudinal river that
1349 drains both the GC and LC analogous to the modern Kura or other present day axial rivers
1350 (Figure 12). Thus, we interpret the reduction up-section of the LC-Vandam component at
1351 Bozdagh as likely reflecting an overall reduction in the exposed area of volcanic and
1352 volcanoclastic sources in the GC. From paleocurrent data at the western terminus of the KFTB,
1353 we know that the development of the KFTB during the Akchagylian-Apsheronian period
1354 significantly perturbed the foreland drainage network, as formerly south-flowing rivers were
1355 locally defeated and reversed to drain northwards into the piggy-back Alazani basin (Sukhishvili
1356 et al., 2021). Thus, if Bozdagh represents a paleo-Kura like drainage, then the up-section
1357 changes in provenance in the Bozdagh section could also reflect progressive sequestering in the

1358 KFTB and nascent Alazani basin of material derived from the southeastern GC during the
1359 Apsheronian.

1360 Finally, in Goy, the angular unconformity between Akcaghylian and Apsheronian
1361 sediments is thought to date the timing of initiation in the KFTB at this longitude (Forte et al.,
1362 2013; Lazarev et al., 2019). By the base of the Apsheronian, the provenance of Goy appears to
1363 be dominated by GC Interior sources, though coupled with the coarsening upward seen from
1364 unit G2-A to G2-B and unit G3 in Lazarev et al., (2019), the independent constraint on the KFTB
1365 having initiated by that time suggests the up-section change in the apparent sourcing from
1366 geochemistry could also be a recycling signature. Detrital zircon data from higher in the Goy
1367 section would likely clarify whether this is the case.

1368

1369 ***6.2.5 Summary of Tectonic Implications from Provenance***

1370 In Figure 13 we summarize our preferred sequence of events within the central KFTB at
1371 the longitude of the Sarica, Xocashen, and Bozdagh sections and based on our new provenance
1372 data and prior work. During Productive Series time, the southern range front of the eastern GC
1373 exposed a mixture of thrust-bounded sections of volcanic and volcanoclastic rocks that likely
1374 reflect slices of distal LC arc material, overlain by, and in thrust contact with GC flysch (Figure
1375 13a). We hypothesize that at this time, the range-front fault thrusting Mesozoic volcanic rocks
1376 over Cenozoic basin fill was the primary active structure in the range, prior to the development
1377 of the KFTB. We further infer that the cross-strike width of volcanic and volcanoclastic rocks
1378 along the southeastern range front of the GC was wider at this time than it is today. This model
1379 does not preclude other structures from being active at the time and our data do not directly

1380 constraint the history of any of the individual structures within the GC, but the localization of
1381 deformation near the range front is consistent with in-sequence propagation of structures and
1382 the subsequent evolution of the system as we interpret below from the provenance data.

1383 By the time of the Akchagylian-Apsheronian boundary (Figure 13b), exposure of the
1384 volcanic and volcanoclastic rocks had progressively decreased as the thrust slice(s) that
1385 contained these rocks were exhumed and eroded via south-directed thrusting along the
1386 range front fault system(s). On the basis of the provenance and stratigraphy, it is at this time,
1387 i.e., ~2.1 Ma, that we suggest deformation began to propagate into the foreland, initiating the
1388 KFTB and formation of the Alazani piggyback basin (Figure 13b). However, as discussed in
1389 Section 6.2.4, we acknowledge that available data do not precisely constrain the timing of
1390 initiation of the central KFTB and that onset could be younger and closer to ~1 Ma. We favor
1391 the interpretation of an initiation age closer to ~2 Ma because we generally assume that coarse
1392 sediment arrival from the uplift of structures to the north of Sarica would precede significant
1393 weathering and associated reduction of the LC-Vandam component of this material. However,
1394 clarifying the timing within the central KFTB should be a priority in future work. Our preferred
1395 interpretation of an ~2.1 Ma initiation for the central KFTB implies broadly synchronous timing
1396 for KFTB initiation along strike, with Akchagylian to basal Apsheronian initiation at the longitude
1397 of Sarica, Xocashen, and Bozdagh matching KFTB initiation estimated both to the west
1398 (Sukhishvili et al., 2021) and east (Forte et al., 2013; Lazarev et al., 2019). Synchronous initiation
1399 along strike is contrary to previous suggestions of east-younging diachronous initiation that was
1400 inferred from sparse data (e.g., Forte et al., 2010). Based on recent comparisons of low-
1401 temperature thermochronology and ¹⁰Be exhumation rates (Forte et al., 2022), Akchagylian to

1402 basal Apsheronian initiation of the KFTB would be coincident with a larger structural
1403 reorganization within the range that caused deformation within the interior of the GC to
1404 expand to the north, possibly related to duplexing at depth along the basal GC thrust system
1405 (Forte et al., 2015b). In addition, initiation of the KFTB likely resulted in initial slowing of activity
1406 on the rangefront fault system and the onset of increasing embayment of the rangefront via
1407 erosion and burial as the Alazani piggyback basin began to fill (e.g., Forte et al., 2010; Mosar et
1408 al., 2010).

1409 By the time of the boundary between the Apsheronian and Bakunian stages (Figure
1410 13c), we infer that the Sarica fold itself likely began to form, shedding coarser-grained and
1411 further-recycled material southward to be deposited at Xocashen (Figure 13c). Such timing
1412 implies in-sequence propagation of the KFTB at this longitude, which contrasts with the out-of-
1413 sequence propagation seen in portions of the eastern terminus of the belt (Forte et al., 2013)
1414 and GC (Tye et al., 2022). Throughout the depositional history, we suggest that Bozdagh
1415 experienced deposition from a paleo-Kura-like axial drainage. This axial drainage subsequently
1416 entrenched between the Bozdagh and Xocashen folds sometime during the Bakunian stage or
1417 later, when both the Xocashen and Bozdagh folds began to form, but our data do not constrain
1418 the timing of either of these structures more precisely than initiation during or after Bakunian
1419 time.

1420 Ultimately, our preferred sequence of events within the KFTB is consistent with recent
1421 work suggestive of more synchronous initiation of the KFTB along strike (Forte et al., 2013;
1422 Lazarev et al., 2019; Sukhishvili et al., 2021) and thus is consistent, at least in a structural sense,
1423 with widening of the orogen in response to a regional shift to more arid conditions (Whipple

1424 and Meade, 2004, 2006; Forte et al., 2013). However, it remains unclear if a climatically induced
1425 widening also explains the potentially coincident internal structural reorganization and
1426 northward shift of the locus of exhumation within the GC (Figure 13; e.g., Forte et al., 2015b,
1427 2022). Internal deformation within the orogen coincident with widening is not an unexpected
1428 response to either changes in taper angle (e.g., Whipple and Meade, 2004, 2006; Hoth et al.,
1429 2006) or as part of accretion cycles (e.g., Hoth et al., 2007), but establishing the coincidence of
1430 KFTB initiation and internal GC reorganization requires better timing of both, especially the
1431 internal reorganization. Remaining uncertainty in the exact timing of initiation of the central
1432 KFTB structures along the traverse between Sarica and Bozdagh could be reduced via infilling
1433 the detrital zircon geochronology record.

1434 Our results highlight that multiproxy sediment provenance work, paired with additional
1435 stratigraphic and structural characterization of regions within the KFTB, may be a viable method
1436 for constraining the timing of initiation throughout the thrust belt. Such additional timing
1437 information is important for clarifying the drivers of fold-thrust belt initiation and deformation
1438 front expansion within the GC. In contrast, tying the structural changes to a potential climatic
1439 trigger for initiation requires more paleoclimatic context for the KFTB sediments.

1440

1441 **6.3 Implications for Provenance Studies in Forelands**

1442 More broadly, results of our work provide some general insights for sediment
1443 provenance investigations within other foreland fold-thrust belts. Detrital zircon U-Pb
1444 geochronology is unquestionably a go-to method for sediment provenance investigations
1445 across a range of tectonic settings (e.g., Gehrels, 2014; Žák et al., 2020; Jian et al., 2022).

1446 However, this method is not without challenges in terms of uniquely interpreting the
1447 provenance history while accounting for sources of bias or other complications (e.g., Cawood et
1448 al., 2003; Amidon et al., 2005; Andersen, 2005; Link et al., 2005; Lawrence et al., 2011; Raines
1449 et al., 2013; Spencer et al., 2018; Malkowski et al., 2019). The results of our analysis echo those
1450 of other recent work (e.g., Malkowski et al., 2019), namely that interpretation of detrital zircon
1451 geochronology is the most robust when done in concert with other indicators of sediment
1452 provenance. In our particular example, the inclusion of bulk rock geochemistry and sandstone
1453 petrography is critical for recognizing the potential role of sediment recycling within the KFTB.
1454 Furthermore, exploring mechanisms to reconcile the apparent discrepancies between the
1455 geochemical/petrographic data and the DZ results leads to insights regarding the timing of
1456 onset of sediment recycling and thus initiation of the KFTB, insights that are not apparent from
1457 DZ U-Pb populations alone.

1458 One of the reasons for the propagation of DZ as an effectively default provenance
1459 method, beyond the ubiquity and durability of zircons in many sediments, is the relative ease
1460 and low cost of the analyses (e.g., Gehrels, 2012). In this respect, we emphasize that bulk rock
1461 geochemistry of either the same sandstone samples used for DZ geochronology, as we present
1462 here, and/or interbedded mudstones (e.g., Pe-Piper et al., 2008; Malkowski et al., 2019)
1463 represents a similarly easy and cost-effective provenance technique that pairs well with DZ
1464 geochronology. Simultaneous application of both techniques has the potential to reveal
1465 additional details regarding the provenance and interpreted tectonic history of a region, as our
1466 study demonstrates.

1467

1468 **7. CONCLUSIONS**

1469 The results of our multiproxy provenance analysis of Kura Fold-Thrust Belt sandstones
1470 and potential source regions within the Greater and Lesser Caucasus provide additional context
1471 and considerations for future provenance work within the Kura Basin or Fold-Thrust Belt. In
1472 addition, these data help to clarify the structural evolution of both the southeastern Greater
1473 Caucasus and Kura-Fold-Thrust Belt, and specifically add weight to the suggestion from some
1474 prior work that initiation of the Kura Fold-Thrust Belt may have been nearly synchronous along-
1475 strike. Specific notable conclusions from this work include:

- 1476 1. Source characterization, and thus resulting indications of sediment provenance
1477 within the foreland, from sandstone petrography, bulk major and trace element
1478 geochemistry, and detrital zircon geochronology broadly overlap, but have some
1479 important differences. Source terranes defined on the basis of geochemistry or
1480 framework grains span geographically broader regions than those defined by detrital
1481 zircon populations. Specifically, while prior work characterizing detrital zircon source
1482 terranes identifies 7 distinct sources within the Caucasus region (of which 5
1483 represent source from the Greater Caucasus, 1 represents a source from the Lesser
1484 Caucasus and Transcaucasus, and 1 represents a source from the Eastern European
1485 Craton), we are able to differentiate 2 main sources using sediment geochemistry,
1486 one that reflects sourcing from the GC interior (e.g., the basement and/or Jurassic-
1487 Cretaceous flysch) and another that reflects sourcing either from the Jurassic-
1488 Cretaceous volcanic and volcanoclastics along the southern margin of the GC or the
1489 similarly aged LC arc rocks. Both geochemical sources can be further refined into two

1490 subpopulations broadly reflective of their relative SiO₂ content, which convey
1491 information on the nuanced geology of the particular samples but are not
1492 geographically distinct.

1493 2. Within the Kura Fold-Thrust Belt sandstone samples, sandstone petrography and
1494 trace element geochemistry are broadly correlative and provide similar information
1495 with respect to potential provenance histories. This suggests that with respect to
1496 these two methods, future provenance work in the Kura Fold-Thrust Belt could
1497 largely focus on inclusion of bulk trace element geochemistry, which is a
1498 substantially less work intensive methodology than sandstone petrography.

1499 3. Our geochemical and petrographic data indicate that the majority of Kura Fold-
1500 Thrust Belt sections record an up-section change in apparent provenance from a
1501 more volcanic and volcanoclastic source (i.e., the LC-Vandam) to one more reflective
1502 of sourcing from the interior of the modern GC, which is dominated by Jurassic-
1503 Cretaceous flysch. In contrast, U-Pb ages from detrital zircons suggest relatively
1504 minimal changes between the bottom and top of the sections, and instead reveal
1505 different sourcing between the sections. We interpret that this apparent divergence
1506 between the provenance methods in part reflects an up-section increase in
1507 sediment recycling and local reworking related to initiation of structures within the
1508 belt. This implies that in part, the apparent up-section change evident in the
1509 geochemistry and petrography to a modern GC Interior like source is not real, but
1510 instead reflects that after weathering of unstable components of the LC-Vandam like
1511 source, sediments geochemically/petrographically will appear somewhat similar to

1512 the GC Interior source. In detail, while the onset of sediment recycling is captured by
1513 the geochemical and petrographic data, the DZ data are insensitive to this change.

1514 4. Integrating provenance changes from the different methods suggests that before
1515 the Akchagylian-Apsheronian boundary (~2.1 Ma), a progressive up-section
1516 reduction in the volcanic and volcanoclastic component observed within the Kura
1517 Fold-Thrust Belt reflects a progressive decrease in the spatial extent of this source in
1518 southeastern Greater Caucasus. We interpret this decrease over time to reflect
1519 progressive exhumation and erosion of a thrust-bounded slice(s) of the Vandam and
1520 equivalent rocks along the range-front fault system, although other mechanisms are
1521 permitted, such as changes in the spatial distribution of focused erosion or along-
1522 strike sourcing of sediment.

1523 5. Shortly after the Akchagylian-Apsheronian boundary, we interpret the diminishing
1524 volcanic and volcanoclastic component to reflect the onset of Kura Fold-Thrust Belt
1525 deformation within the central part of the belt, where the mafic to intermediate,
1526 unstable components diagnostic of the volcanic and volcanoclastic source terranes
1527 were selectively weathered during recycling and local reworking. This implies that
1528 the initiation age of the central Kura Fold-Thrust Belt overlaps with timing
1529 constrained in the western and eastern termini of the belt and further indicates that
1530 the belt initiated nearly synchronously along-strike. Synchronous initiation of the
1531 KFTB is consistent with the proposition that growth of the thrust belt represents a
1532 nearly synchronous, major structural reorganization and resultant widening of the
1533 GC orogen. Although this reorganization and widening could have been climatically

1534 driven, further tests of that hypothesis would benefit from both more complete
1535 regional paleoclimate records and refined timing of initiation of the belt, especially
1536 in the western section, near the Gombori Range.

1537 6. The structural history we interpret from sediment provenance implies broadly in-
1538 sequence, north-to-south propagation of the locus of active deformation from the
1539 southeastern margin of the Greater Caucasus into the Kura Fold-Thrust Belt.

1540 Similarly, our results imply predominantly in-sequence propagation of structures
1541 within the central Kura Fold-Thrust Belt as well. This differs from histories of out-of-
1542 sequence deformation in the eastern Kura Fold-Thrust Belt and eastern tip of the
1543 Greater Caucasus, highlighting diverse structural histories over relatively modest
1544 (~100 km) distances along-strike.

1545 7. Finally, the results from the Kura Fold-Thrust Belt highlight the utility of integrating
1546 diverse sediment provenance methods within actively deforming regions as this may
1547 allow both for better characterization of potential biases and complications that
1548 could otherwise hinder correct interpretation, but also have the potential to expand
1549 the ability to recognize important drivers of provenance change.

1550

1551 **ACKNOWLEDGEMENTS**

1552 We thank Boris Avdeev, Zak Murturzayev, Tea Mumladze, Ana Menabde, David
1553 Kandelaki, Christian van Baak, and Iuliana Vasiliev with help in collecting the samples presented
1554 here. We additionally thank Tea Godoladze, Misha Elashvili, Zurab Javakhishvili, Talat Kangarli,
1555 and Ibrahim Murturzayev for assistance in accessing the field areas and general logistic support.

1556 We thank Christopher Campisano for the use of his lab facility at ASU for processing the ash
1557 samples for tephra geochemistry, Axel Wittmann for his assistance during microprobe analyses
1558 at ASU, Sarah Roeske for her assistance during microprobe analyses at UC Davis, and the staff
1559 of the U of A LaserChron facility for their assistance during the detrital zircon analyses. We
1560 thank Charles Trexler and Alex Tye for helpful conversations regarding the provenance of
1561 sediments and their structural context within the Greater Caucasus region. Finally, we thank
1562 Associate Editor Joel Saylor, Nicholas Perez, and an anonymous reviewer for extensive
1563 comments on the manuscript. This material is based upon work originally supported by
1564 National Science Foundation grants EAR-0810285 (Cowgill), with additional funding provided to
1565 Forte by NSF grant EAR-1450970, the UC Davis Department of Geology Cordell Durrell Fund,
1566 Geological Society of America, and American Association of Petroleum Geologists. Manuscript
1567 preparation was supported by NSF grants EAR-1524631 and EAR-2050623 (Cowgill) and EAR-
1568 1524304 and EAR-2050618 (Niemi).

1569

1570 **FIGURE CAPTIONS**

1571

1572 **Figure 1** – Tectonic context, sample locations, and regional geology. a) Locations of major
1573 thrusts from Trexler et al., (2022), colored by the ages of strata they structurally juxtapose.
1574 Bottom inset shows the maximum, minimum, and mean topography within the A-A' swath
1575 profile (gray) and estimated N25E convergence rates between the Greater and Lesser Caucasus
1576 (red) as modified from Forte et al., (2022), which provides further discussion of these plots.
1577 Dashed box outlines the extent of the lower two panels. b) Map showing locations of the

1578 modern river and bedrock samples, as explained in the bottom-right legend. Also shown are the
1579 locations of samples and their respective detrital zircon U-Pb source terranes from Tye et al.,
1580 (2020) and references therein plus additional samples from Forte et al., (2022), as explained in
1581 the top-right legend. Black lines indicate watershed boundaries for modern sediment samples;
1582 bold watershed boundaries indicate catchments for which we present geochemical data and
1583 that Cowgill et al., (2016) presented detrital zircon geochronology. Note that modern river
1584 samples for Kura and Mtkvari represent samples from the same river, where the Mtkvari is
1585 sampled upstream from the Kura and reflects the Georgian (Mtkvari) and Azerbaijani (Kura)
1586 names for the river. Gray circles are other foreland provenance samples from Tye et al. (2020),
1587 Allen et al., (2006), and Abdullayev et al., (2018), including several suites from the Aphseron
1588 Peninsula (AP). Previous foreland samples from Tye et al. (2020) that we discuss in detail are
1589 labeled with their sample names (CF-#, EF-#). c) Same as panel b, but over a map showing a
1590 simplified version of the bedrock geology from Forte et al., (2014). Also highlighted is the zone
1591 of predominantly Cretaceous volcanic and volcanoclastic rocks in the eastern GC, which we refer
1592 to here as the Vandam zone, consistent with prior literature (e.g., Tye et al., 2022).

1593

1594 **Figure 2** - Stratigraphic correlations of the measured sections based on ash geochemistry (red
1595 lines), published magnetostratigraphy (van Baak et al., 2013; Lazarev et al., 2019) (gray lines),
1596 and previous mapping (Abdullaev et al., 1957; Ali-Zade, 2005; Forte, 2012; Forte et al., 2015a)
1597 (black lines). Colored symbols with numbers to the right of each column indicate samples
1598 analyzed here. Boxes containing unit names within each section are colored by depositional
1599 environment, as indicated in legend. Black lines show our correlations between the sections,

1600 the global geomagnetic polarity timescale (GPTS - Ogg, 2020), and the regional timescales of
1601 Krijgsman et al. (2019) and Lazarev et al. (2021), which differ in Akchagylian duration. In
1602 Vashlovani and Goy sections the diagonal boundaries between Akchagylian and Apsheronian
1603 indicate uncertainty in the exact location of the boundary within the measured section. Inset
1604 map shows locations of stratigraphic sections (black dots) and areas (boxes with red gradients)
1605 where timing of the Kura Fold-Thrust belt initiation is constrained to the east (Forte et al., 2013;
1606 Lazarev et al., 2019) and west (Sukhishvili et al., 2021). Vertical bars with red shading on the
1607 timeline indicate initiation ages of major structures in the region (E = Eastern KFTB).

1608

1609 **Figure 3** - Plots of tephra shard geochemistry. Samples from measured sections are indicated in
1610 the explanation and indicated at the stratigraphic positions shown on Figure 2. The three ashes
1611 marked "Other" come from outside the measured sections and are included for potential future
1612 work in this region and are not directly relevant to the main points of this effort. a) Plot of
1613 natural log of element ratios highlighting separation of different ash populations and
1614 emphasizing the existence of two modes (M1, M2) within ashes X-3A and B-B. b) Plot of
1615 principal component analysis of ash shard geochemistry suggesting similar groupings as the log
1616 ratios. Notice a significant break in the x-axis, reflecting the extreme difference between all
1617 other samples and the M2 shards in samples B-B and X-3A.

1618

1619 **Figure 4** - Source area characterization from multivariable statistics of bulk-rock trace element
1620 analyses. a) Result of principal component analysis (PCA) highlighting separation of potential
1621 source terranes into four semi-distinct zones with one outlier (AB0863); the Kura River sample

1622 plots in the middle of these fields, consistent with the expectation that it is a mixture of all 4
1623 potential sources; GC = Greater Caucasus, LC = Lesser Caucasus, TC = Transcaucasus. b) Result
1624 of hierarchical clustering analysis highlighting a similar separation as suggested by the PCA in
1625 Figure 4a.

1626

1627 **Figure 5** - Results of linear discriminant analysis considering two different source definitions
1628 (LDA-1 and LDA-3); cross-validation rates are the same for both. Results including LDA-2
1629 provided in Figure S13.

1630

1631 **Figure 6** - Results of two different LDAs (LDA-1 and LDA-3) considered as a function of
1632 stratigraphic position. Correlations and timescale are identical to that shown in Figure 2. Also
1633 shown are the chemical index of alteration (CIA - Nesbitt and Young, 1982). Comparisons of CIA
1634 to other weathering indices are shown in Figure S12 and discussed in Supplemental Text S2.2.5.
1635 Note that generally we do not have constraint on where within the sections between samples
1636 provenance would change, so the location of the changes shown here are schematic. Version of
1637 figure considering results of LDA-2 provided in Figure S14.

1638

1639 **Figure 7** - Comparison of linear discriminant analyses of bulk geochemistry and sandstone
1640 petrography. a) Results of random forest regression that assesses the ability of a given point
1641 count category to predict the value of linear discriminant 1 within LDA-1. Green and blue bars
1642 indicate components most associated with a LC-Vandam and a GC Interior source, respectively.
1643 Black bars indicate components that are less diagnostic for distinguishing between sources. b)

1644 Plots and linear regressions between summed percentages of components related to either LC-
1645 Vandam or a GC Interior source as identified in Figure 4a and linear discriminant 1 of LDA-1. c,
1646 d) Same as Figure 7a and 7b but considering linear discriminant 1 for LDA-2.

1647

1648 **Figure 8** - Composite detrital zircon populations used to define source terranes, following the
1649 definitions by Tye et al., (2020). See text for additional discussion of source terranes. Plot was
1650 generated using DensityPlotter (Vermeesch, 2012) with KDEs colored and PDEs hollow. KDEs
1651 were calculated using an adaptive bandwidth (see Vermeesch, 2012). Colors of KDEs are for
1652 reference in subsequent figures. Colored bars across the top shows 6 diagnostic age ranges
1653 identified by Tye et al., (2020). Pie charts show the proportions of these diagnostic ages within
1654 each composite sample. Both the total number of zircons that define each source (n) and total
1655 samples contributing to the source (N) are shown. Composite samples are detailed in Table 4
1656 and reported by Allen et al., (2006), Wang et al., (2011), Cowgill et al., (2016), Vasey et al.,
1657 (2020), Tye et al., (2020), Trexler et al., (2022), and Forte et al., (2022).

1658

1659 **Figure 9** - Detrital zircon populations for 7 new Kura Fold-Thrust Belt samples. Setup of figure is
1660 identical to Figure 8. DZ populations are grouped by stratigraphic section to ease comparison
1661 between the tops and bottom of sections. Alternative version of this figure with PDPs/KDEs
1662 stacked by approximate stratigraphic age is presented in Figure S15.

1663

1664 **Figure 10** - Results of Bayesian population correlation (Tye et al., 2019) between KFTB samples
1665 and composite sources. Red boxes indicate composite source and KFTB sample with the highest

1666 similarity based on BPC, thick black outlines indicate comparisons between samples from the
1667 top and bottom of individual sections; note that these BPC values are relatively high, indicating
1668 minimal up-section changes in DZ-derived provenance. To minimize bias, samples V-1240 and S-
1669 210 were modified (indicated by *) by removing the young populations of grains that define the
1670 MDAs, see text for explanation. Source terranes abbreviations are as follows: GCSL – GC
1671 siliciclastic, GCB – GC basement, PJS – Pre-Jurassic sedimentary, WGCV – western GC
1672 volcanics, EGCV- eastern GC volcanics, TBLC – Transcaucasus basement and LC arc,
1673 and EUI- Eurasian interior. Red boxes indicate composite source and KFTB sample with the
1674 highest similarity based on BPC.

1675

1676

1677 **Figure 11** - Comparisons between linear discriminant analyses of bulk geochemistry and
1678 Bayesian population correlation of detrital zircon populations. We consider BPC values for the
1679 eastern GC volcanics (EGCV), GC siliciclastic strata (GCSL), and Transcaucasus basement and
1680 LC arc (TBLC) sources, as these are the best represented in the KFTB sandstones. For each
1681 example, the vertical grey bars mark the range covered by the relevant decision boundaries
1682 within the first linear discriminant (see Figure 6 and S14). Comparison of linear discriminant 1
1683 from LDA-1 (panels a-c) or LDA-2 (panels d-f) with BPCs from a/d) the eastern GC volcanics
1684 source (EGCV), b/e) the GC siliciclastic source (GCSL), and c/f) the Transcaucasus basement and
1685 LC arc source (TBLC).

1686

1687 **Figure 12** - Summary of provenance changes through time and space as indicated by both
1688 geochemistry and detrital zircons during a) Meotian-Pontian, b) Productive Series, c)
1689 Akchagylian, d) Apsheronian, and e) Bakunian stages. Vertical colored columns for each section
1690 represent the two possible interpretations of provenance from the LDA classification of the
1691 trace element geochemistry for the portion of the stratigraphy within a given time period. Stars
1692 indicate DZ samples, either those that come from the measured sections (those adjacent to the
1693 LDA results) or from areas further afield within the KFTB from Tye et al., (2020). See explanation
1694 in bottom right for the correspondence between colors and sources. Stars containing more
1695 than one color indicate inferred mixed sources. Map is focused on central KFTB samples and
1696 sections, but results from samples from Tye et al., (2020) outside of this region are shown
1697 schematically, with original sample names from Tye et al., (2020) above each. Grayed out
1698 section locations indicate a lack of data for that time period from that section. Note that this
1699 map is not palinspastic and does not reflect that the distances between sections and the GC or
1700 LC rangefronts would have been different at the time of deposition.

1701

1702 **Figure 13** - Schematic cross-sections through the central KFTB during the a) Productive Series,
1703 b) Akchagylian-Apsheronian boundary, and c) Apsheronian-Bakunian boundary. Diagram is not
1704 to scale, but we schematically depict advection of the sections toward the GC via continued
1705 underthrusting and reduction in distance between sections as KFTB structures initiate and
1706 accommodate shortening. Grayed out section locations indicate there is no data for that time
1707 from that section. Approximate location of Bozdagh (B), Xocashen (X), and Sarica (S) measured
1708 sections are shown. Blue colors indicate flysh sources or stratigraphy that appears to be

1709 sourced from flysch, green colors indicate volcanic/volcaniclastic sources, and orange indicate
1710 sourcing from the mixed GC and LC as seen in Bozdagh or the modern Kura River. The
1711 concentric circle indicates approximate location of axial drainage (Kura River).

1712

1713 **TABLE CAPTIONS**

1714

1715 **Table 1** – Coordinates of top and bottom the measured sections.

1716

1717 **Table 2** – Coordinates of provenance samples including original sample names, sample names
1718 used in the manuscript, and the analyses performed (G – bulk geochemistry, PC – petrography,
1719 DZ – detrital zircon U-Pb geochronology).

1720

1721 **Table 3** – Coordinates of ash samples and means and standard deviations of major elements of
1722 the ash shards extracted from the ash samples.

1723

1724 **Table 4** – Samples and references for those samples used to define composite DZ sources

1725

1726 **Table 5** – Perkins statistical distance between ash samples from within measured sections

1727

1728 **Table 6** – LDA values for source samples and resultant source designations.

1729

1730 **Table 7** – LDA values for KFTB samples and resultant source classifications.

1731

1732

1733 **REFERENCES**

1734 Abdullaev, R.N., Agabekov, M.G., and Gavrilov, M.D., 1957, K-38-XXIX: Geological map of the
1735 USSR.

1736 Abdullayev, N.R., Weber, J., van Baak, C.G.C., Aliyeva, E., Leslie, C., Riley, G.W., O'Sullivan, P.,
1737 and Kislitsyn, R., 2018, Detrital zircon and apatite constraints on depositional ages,
1738 sedimentation rates and provenance: Pliocene Productive Series, South Caspian Basin,
1739 Azerbaijan: Basin Research, p. 1–28, doi:10.1111/bre.12283.

1740 Adamia, S., Alania, V., Chabukiani, A., Kutelia, Z., and Sadradze, N., 2011a, Greater Caucasus
1741 (Cavcasioni): A long-lived North-Tethyan Back-Arc Basin: Turkish Journal of Earth
1742 Sciences, v. 20, p. 611–628.

1743 Adamia, S., Lordkipanidze, M.B., and Zakariadze, G.S., 1977, Evolution of an active continental
1744 margin as exemplified by the alpine history of the Caucasus: Tectonophysics, v. 40, p.
1745 183–199.

1746 Adamia, S., Zakariadze, G.S., Chkhotua, T., Sadradze, N., Tsereteli, N., Chabukiani, A., and
1747 Gventsade, A., 2011b, Geology of the Caucasus: A Review: Turkish Journal of Earth
1748 Sciences, v. 20, p. 489–544.

1749 Agabekov, M.G., Kerimov, K.M., Moshashvili, A.B., and Khain, V.Ye., 1976, New data on the
1750 structure of the central part of the Kura trough: Geotectonics, v. 10, p. 350–354.

1751 Aghayeva, V., Sachsenhofer, R.F., van Baak, C.G.C., Bayramova, S., Ćorić, S., Frühwirth, M.J.,
1752 Rzayeva, E., and Vincent, S.J., 2023, Stratigraphy of the Cenozoic succession in eastern
1753 Azerbaijan: Implications for petroleum systems and paleogeography in the Caspian
1754 basin: Marine and Petroleum Geology, p. 106148,
1755 doi:10.1016/j.marpetgeo.2023.106148.

1756 Agustí, J., Vekua, A., Oms, O., Lordkipanidze, D., Bukhsianidze, M., Kiladze, G., and Rook, L.,
1757 2009, The Pliocene-Pleistocene succession of Kvabebi (Georgia) and the background to
1758 the early human occupation of Southern Caucasus: Quaternary Science Reviews, v. 28,
1759 p. 3275–3280.

1760 Aitchison, J., 1986, The statistical analysis of compositional data (D. R. Cox, D. V. Hinkley, D.
1761 Rubin, & B. W. Silverman, Eds.): London, Chapman and Hall, 416 p.

1762 Alania, V., Beridze, T., Enukidze, O., Chagelishvili, R., Lebanidze, Z., Maqadze, D., Razmadze, A.,
1763 Sadradze, N., and Tevzadze, N., 2021a, The geometry of the two orogens convergence

- 1764 and collision zones in Central Georgia: New data from seismic reflection profiles, *in*
1765 Bonali, F.L., Pasquaré Mariotto, F., and Tsereteli, N. eds., *Building Knowledge for*
1766 *Geohazard Assessment and Management in the Caucasus and other Orogenic Regions,*
1767 *Dordrecht, Springer Netherlands, NATO Science for Peace and Security Series C:*
1768 *Environmental Security*, p. 73–88, doi:10.1007/978-94-024-2046-3.
- 1769 Alania, V., Chabukiani, A.O., Chagelishvili, R.L., and Enukidze, O.V., 2015, Growth structures ,
1770 piggy-back basins and growth strata of the Georgian part of the Kura foreland fold –
1771 thrust belt : implications for Late Alpine kinematic evolution, *in* Sosson, M., Stephenson,
1772 R.A., and Adamia, S.A. eds., *Tectonic Evolution of the Eastern Black Sea and Caucasus,*
1773 *Geological Society of London Special Publication*, v. 428, doi:10.1144/SP428.5.
- 1774 Alania, V., Tibaldi, A., Bonali, F.L., Enukidze, O., and Russo, E., 2021b, Structural Architecture of
1775 the Western Greater Caucasus Orogen: New Data from a Crustal-Scale Structural Cross-
1776 Section, *in* Bonali, F.L., Pasquaré Mariotto, F., and Tsereteli, N. eds., *Building Knowledge*
1777 *for Geohazard Assessment and Management in the Caucasus and other Orogenic*
1778 *Regions, Dordrecht, Springer Netherlands, NATO Science for Peace and Security Series*
1779 *C: Environmental Security*, p. 59–71, doi:10.1007/978-94-024-2046-3_5.
- 1780 Aliyeva, E.G.-M., 2005, Reservoirs of the lower Pliocene Productive Series at the western flank
1781 of the South Caspian Basin: *Lithology and Mineral Resources*, v. 40, p. 267–278.
- 1782 Ali-Zade, A.A., 2005, *Geological Map of Azerbaijan Republic.*:
- 1783 Allen, P.A., and Heller, P.L., 2012, Dispersal and preservation of tectonically generated alluvial
1784 gravels in sedimentary basins, *in* Busby, C.J. and Azor, A. eds., *Tectonics of Sedimentary*
1785 *Basins: Recent Advances*, Blackwell Publishing, p. 111–130.
- 1786 Allen, M.B., Jackson, J., and Walker, R., 2004, Late Cenozoic reorganization of the Arabia-Eurasia
1787 collision and the comparison of short-term and long-term deformation rates: *Tectonics*,
1788 v. 23, p. doi:10.1029/2003TC001530-doi:10.1029/2003TC001530.
- 1789 Allen, M.B., Morton, A.C., Fanning, C.M., Ismail-Zadeh, A., and Kroonenberg, S.B., 2006, Zircon
1790 age constraints on sediment provenance in the Caspian region: *Journal of the Geological*
1791 *Society of London*, v. 163, p. 647–655.
- 1792 Amidon, W.H., Burbank, D., and Gehrels, G.E., 2005, Construction of detrital mineral
1793 populations: insights from mixing of U-Pb zircon ages in Himalayan rivers: *Basin*
1794 *Research*, v. 17, p. 463–485, doi:10.1111/j.1365-2117.2005.00279.x.
- 1795 Andersen, T., 2005, Detrital zircons as tracers of sedimentary provenance: limiting conditions
1796 from statistics and numerical simulation: *Chemical Geology*, v. 216, p. 249–270.
- 1797 Avdeev, B., and Niemi, N.A., 2011, Rapid Pliocene exhumation of the central Greater Caucasus
1798 constrained by low-temperature thermochronometry: *Tectonics*, v. 30,
1799 doi:10.1029/2010TC002808.

- 1800 van Baak, C.G.C., 2010, Glacio-Marine transgressions of the early and middle Pleistocene
1801 Caspian Basin, Azerbaijan: Utrecht University, 21 p.
- 1802 van Baak, C.G.C. et al., 2017, Paratethys response to the Messinian salinity crisis: Earth-Science
1803 Reviews, v. 172, p. 193–223, doi:10.1016/j.earscirev.2017.07.015.
- 1804 van Baak, C.G.C., Grothe, A., Richards, K., Stoica, M., Aliyeva, E., Davies, G.R., Kuiper, K.F., and
1805 Krijgsman, W., 2019, Flooding of the Caspian Sea at the intensification of Northern
1806 Hemisphere Glaciations: Global and Planetary Change, v. 174, p. 153–163,
1807 doi:10.1016/j.gloplacha.2019.01.007.
- 1808 van Baak, C.G.C., Vasiliev, I., Stoica, M., Kuiper, K.F., Forte, A.M., Aliyeva, E., and Krijgsman, W.,
1809 2013, A magnetostratigraphic time frame for Plio-Pleistocene transgressions in the
1810 South Caspian Basin, Azerbaijan: Global and Planetary Change, v. 103, p. 119–134,
1811 doi:10.1016/j.gloplacha.2012.05.004.
- 1812 Bande, A., Horton, B.K., Ramírez, J.C., Mora, A., Parra, J.L., and Stockli, D.F., 2012, Clastic
1813 deposition, provenance, and sequence of Andean thrusting in the frontal Eastern
1814 Cordillera and Llanos foreland basin of Columbia: Geological Society of America Bulletin,
1815 v. 124, p. 59–76.
- 1816 Banks, C.J., Robinson, A.G., and Williams, M.P., 1997, Structure and regional tectonics of the
1817 Achara-Trialet fold belt and the adjacent Rioni and Karli foreland basins, Republic of
1818 Georgia, *in* Robinson, A.G. ed., Regional and petroleum geology of the Black Sea and
1819 surrounding region, p. 331–346.
- 1820 Bhatia, M.R., 1983, Plate tectonics and geochemical compositions of sandstones: The Journal of
1821 Geology, v. 91, p. 611–627.
- 1822 Bhatia, M.R., and Crook, K.A.W., 1986, Trace element characteristics of graywackes and tectonic
1823 setting discrimination of sedimentary basins: Contributions to Mineralogy and
1824 Petrology, v. 92, p. 181–193.
- 1825 Bonjour, J.-L., and Dabard, M.-P., 1991, Ti/Nb ratios of clastic terrigenous sediments used as an
1826 indicator of provenance: Chemical Geology, v. 91, p. 257–267.
- 1827 van der Boon, A., van Hinsbergen, D.J.J., Rezaeian, M., Gürer, D., Honarmand, M., Pastor-Galán,
1828 D., Krijgsman, W., and Langereis, C.G., 2018, Quantifying Arabia–Eurasia convergence
1829 accommodated in the Greater Caucasus by paleomagnetic reconstruction: Earth and
1830 Planetary Science Letters, v. 482, p. 454–469, doi:10.1016/j.epsl.2017.11.025.
- 1831 Burbank, D., Beck, R.A., Reynolds, R.G.H., Hobbs, R.S., and Tahirkheli, R.A.K., 1988, Thrusting
1832 and gravel progradation in foreland basins: A test of post-thrusting gravel dispersal:
1833 Geology, v. 16, p. 1143–1146.

- 1834 Capaldi, T.N., Horton, B.K., McKenzie, N.R., Mackaman-Lofland, C., Stockli, D.F., Ortiz, G., and
1835 Alvarado, P., 2020, Neogene Retroarc Foreland Basin Evolution, Sediment Provenance,
1836 and Magmatism in Response to Flat Slab Subduction, Western Argentina: *Tectonics*, v.
1837 39, doi:10.1029/2019TC005958.
- 1838 Carrapa, B., Strecker, M.R., and Sobel, E.R., 2006, Cenozoic orogenic growth in the Central
1839 Andes: Evidence from sedimentary rock provenance and apatite fission track
1840 thermochronology in the Fiambalá Basin, southernmost Puna Plateau margin (NW
1841 Argentina): *Earth and Planetary Science Letters*, v. 247, p. 82–100.
- 1842 Cavazza, W., Gusmeo, T., Zattin, M., Alania, V., Enekidze, O., Corrado, S., and Schito, A., 2023,
1843 Two-step exhumation of Caucasian intraplate rifts: A proxy of sequential plate-margin
1844 collisional orogenies: *Geoscience Frontiers*, p. 101737, doi:10.1016/j.gsf.2023.101737.
- 1845 Cawood, P.A., Nemchin, A.A., Freeman, M., and Sircombe, K., 2003, Linking source and
1846 sedimentary basin: Detrital zircon record of sediment flux along a modern river system
1847 and implications for provenance studies: *Earth and Planetary Science Letters*, v. 210, p.
1848 259–268.
- 1849 Comas-Cufí, M., and Thió-Henestrosa, S., 2011, CoDaPack 2.0: a stand-alone, multi-platform
1850 compositional software, *in* Egozcue, J.J., Tolosana-Delgado, R., and Ortego, M.I. eds., 4th
1851 International Workshop on Compositional Data Analysis, Sant Feliu de Guixols.
- 1852 Cowgill, E., Forte, A.M., Niemi, N.A., Avdeev, B., Tye, A.R., Trexler, C.C., Javakishvirli, Z., Elashvili,
1853 M., and Godoladze, T., 2016, Relict basin closure and crustal shortening budgets during
1854 continental collision: An example from Caucasus sediment provenance: *Tectonics*, v. 35,
1855 p. 2918–2947, doi:10.1002/2016TC004295.
- 1856 Cowgill, E., Niemi, N.A., Forte, A.M., and Trexler, C.C., 2018, Reply to Comment by Vincent et
1857 al.: *Tectonics*, v. 37, p. 1017–1028, doi:10.1002/2017TC004793.
- 1858 Dahlen, F.A., 1990, Critical taper model of fold-and-thrust belts and accretionary wedges:
1859 *Annual Review of Earth and Planetary Sciences*, v. 18, p. 55–99.
- 1860 Dahlen, F.A., and Suppe, J., 1988, Mechanics, growth, and erosion of mountain belts, *in* Clark
1861 Jr., S.P., Burchfiel, B.C., and Suppe, J. eds., *Processes in Continental Lithospheric*
1862 *Deformation*, Special Paper Geological Society of America, p. 161–178.
- 1863 Darin, M.H., and Umhoefer, P.J., 2022, Diachronous initiation of Arabia–Eurasia collision from
1864 eastern Anatolia to the southeastern Zagros Mountains since middle Eocene time:
1865 *International Geology Review*, v. 64, p. 2653–2681,
1866 doi:10.1080/00206814.2022.2048272.
- 1867 Davis, D., Suppe, J., and Dahlen, F.A., 1983, Mechanics of fold-and-thrust belts and accretionary
1868 wedges: *Journal of Geophysical Research*, v. 88, p. 1153–1172.

- 1869 DeCelles, P.G., Gehrels, G.E., Quade, J., Ojha, T.P., Kapp, P.A., and Upreti, B.N., 1998, Neogene
1870 foreland basin deposits, erosional unroofing, and the kinematic history of the Himalayan
1871 fold-thrust belt, western Nepal: *Geological Society of America Bulletin*, v. 110, p. 2–21.
- 1872 Dhont, D., and Chorowicz, J., 2006, Review of the neotectonics of the Eastern Turkish-Armenian
1873 Plateau by geomorphic analysis of digital elevation model imagery: *International Journal*
1874 *of Earth Science*, v. 95, p. 34–49.
- 1875 Dickinson, W.R., 1970, Interpreting detrital modes of graywacke and arkose: *Journal of*
1876 *Sedimentary Petrology*, v. 40, p. 695–707.
- 1877 Dickinson, W.R., and Suczek, C.A., 1979, Plate tectonics and sandstone compositions: *American*
1878 *Association of Petroleum Geologists Bulletin*, v. 63, p. 2164–2182.
- 1879 Egozcue, J.J., and Pawlowsky-Glahn, V., 2005, Groups of parts and their balances in
1880 compositional data analysis: *Mathematical Geology*, v. 37, p. 795–828.
- 1881 Egozcue, J.J., Pawlowsky-Glahn, V., Mateu-Figueras, G., and Barceló-Vidal, C., 2003, Isometric
1882 logratio transformations for compositional data analysis: *Mathematical Geology*, v. 35,
1883 p. 279–300.
- 1884 Fedo, C., Nesbitt, H.W., and Young, G.M., 1995, Unraveling the effects of potassium
1885 metasomatism in sedimentary rocks and paleosols, with implications for
1886 paleoweathering conditions and provenance: *Geology*, v. 23, p. 921–924.
- 1887 Fedo, C., Sircombe, K., and Rainbird, R.H., 2003, Detrital zircon analysis of the sedimentary
1888 record, *in* Hanchar, J.M. and Hoskin, P.W.O. eds., *Zircon*, p. 277–303.
- 1889 Forte, A.M., 2012, Late Cenozoic Evolution of the Greater Caucasus Mountains and Kura
1890 Foreland Basin: Implications for Early Orogenesis: University of California, Davis.
- 1891 Forte, A.M., and Cowgill, E., 2013, Late Cenozoic base-level variations of the Caspian Sea: A new
1892 review of its history and proposed driving mechanisms: *Palaeogeography,*
1893 *Palaeoclimatology, Palaeoecology*, v. 386, p. 392–407,
1894 doi:10.1016/j.palaeo.2013.05.035.
- 1895 Forte, A.M., Cowgill, E., Bernardin, T., Kreylos, O., and Hamann, B., 2010, Late Cenozoic
1896 deformation of the Kura fold-thrust belt, southern Greater Caucasus: *Geological Society*
1897 *of America Bulletin*, v. 122, p. 465–486.
- 1898 Forte, A.M., Cowgill, E., Murtuzayev, I., Kangarli, T., and Stoica, M., 2013, Structural geometries
1899 and magnitude of shortening in the eastern Kura fold-thrust belt, Azerbaijan:
1900 Implications for the development of the Greater Caucasus Mountains: *Tectonics*, v. 32,
1901 doi:10.1002/tect.20032.

- 1902 Forte, A.M., Cowgill, E., and Whipple, K.X., 2014, Transition from a singly vergent to doubly
 1903 vergent wedge in a young orogen: The Greater Caucasus: *Tectonics*, v. 33, p. 2077–2101,
 1904 doi:10.1002/2014TC003651.
- 1905 Forte, A.M., Gutterman, K., Van Soest, M.C., and Gallagher, K., 2022, Building a Young Mountain
 1906 Range: Insight into the Growth of the Greater Caucasus Mountains from Detrital Zircon
 1907 (U-Th)/He Thermochronology and ¹⁰Be Erosion Rates: *Tectonics*,
 1908 doi:10.1029/2021TC006900.
- 1909 Forte, A.M., Sumner, D.Y., Cowgill, E., Stoica, M., Murtuzayev, I., Kangarli, T., Elashvili, M.,
 1910 Godoladze, T., and Javakishvirli, Z., 2015a, Late Miocene to Pliocene stratigraphy of the
 1911 Kura Basin, a subbasin of the South Caspian Basin: Implications for the diachroneity of
 1912 stage boundaries: *Basin Research*, doi:10.1111/bre.12069.
- 1913 Forte, A.M., Whipple, K.X., and Cowgill, E., 2015b, Drainage network reveals patterns and
 1914 history of active deformation in the eastern Greater Caucasus: *Geosphere*, v. 11,
 1915 doi:10.1130/GES01121.1.
- 1916 Froggatt, P.C., 1992, Standardization of the chemical analysis of tephra deposits. Report of the
 1917 ICCT Working Group: *Quaternary International*, v. 13–14, p. 93–96, doi:10.1016/1040-
 1918 6182(92)90014-S.
- 1919 Gabunia, L., Vekua, A., and Lordkipanidze, D., 2000, The environmental contexts of early human
 1920 occupation of Georgia (Transcaucasia): *Journal of Human Evolution*, v. 38, p. 785–802,
 1921 doi:10.1006/jhev.1999.0383.
- 1922 Gamkrelidze, I.P., 1986, Geodynamic evolution of the Caucasus and adjacent areas in alpine
 1923 time: *Tectonophysics*, v. 127, p. 261–277.
- 1924 Gamkrelidze, I., Shengelia, D., Tsutsunava, T., Chung, S.-L., and Chikhelidze, K., 2011, New Data
 1925 on the U-Pb Zircon Age of the Pre-Alpine Crystalline Basement of the Black-Sea-Central
 1926 Transcaucasian Terrane and their Geological Significance: v. 5.
- 1927 Garber, K.L., Finzel, E.S., and Pearson, D.M., 2020, Provenance of Synorogenic Foreland Basin
 1928 Strata in Southwestern Montana Requires Revision of Existing Models for Laramide
 1929 Tectonism: *North American Cordillera: Tectonics*, v. 39, doi:10.1029/2019TC005944.
- 1930 Gehrels, G.E., 2014, Detrital Zircon U-Pb Geochronology Applied to Tectonics: *Annual Review of*
 1931 *Earth and Planetary Sciences*, v. 42, p. 127–149, doi:10.1146/annurev-earth-050212-
 1932 124012.
- 1933 Gehrels, G.E., 2012, Detrital Zircon U-Pb geochronology: Current Methods and New
 1934 Opportunities, *in* Busby, C.J. and Azor, A. eds., *Recent advances in tectonics of*
 1935 *sedimentary basins*, Blackwell Publishing, p. 47–62.

- 1936 Gehrels, G.E., Valencia, V., and Pullen, A., 2006, Detrital zircon geochronology by laser-ablation
1937 multicollector icpms at the Arizona Laserchron Center, *in* Olszewski, T. ed.,
1938 Geochronology: Emerging Opportunities, Paleontological Society Short Course,
1939 Philadelphia, The Paleontological Society, v. 12.
- 1940 Gehrels, G.E., Valencia, V., and Ruiz, J., 2008, Enhanced precision, accuracy, efficiency, and
1941 spatial resolution of U-Pb ages by laser ablation-multicollector-inductively coupled
1942 plasma-mass spectrometry: *Geochemistry Geophysics Geosystems*, v. 9,
1943 doi:10.1029/2007GC001805.
- 1944 Grömping, U., 2009, Variable Importance Assessment in Regression: Linear Regression versus
1945 Random Forest: *The American Statistician*, v. 63, p. 308–319,
1946 doi:10.1198/tast.2009.08199.
- 1947 Gunnels, M., Yetrimishli, G., Kazimova, S., and Sandvol, E., 2020, Seismotectonic evidence for
1948 subduction beneath the Eastern Greater Caucasus: *Geophysical Journal International*, v.
1949 224, p. 1825–1834, doi:10.1093/gji/ggaa522.
- 1950 Harnois, L., 1988, The CIW index: A new chemical index of weathering: *Sedimentary Geology*, v.
1951 55, p. 319–322.
- 1952 Herron, M.M., 1988, Geochemical classification of terrigenous sands and shales from core or
1953 log data: *Journal of Sedimentary Petrology*, v. 58, p. 820–829.
- 1954 van Hinsbergen, D.J.J., Torsvik, T.H., Schmid, S.M., Matenco, L.C., Maffione, M., Vissers, R.L.M.,
1955 Gurer, D., and Spakman, W., 2019, Orogenic architecture of the Mediterranean region
1956 and kinematic reconstruction of its tectonic evolution since the Triassic: *Gondwana*
1957 *Research*, doi:10.1016/j.gr.2019.07.009.
- 1958 Hoth, S., Adam, J., Kukowski, N., and Oncken, O., 2006, Influence of erosion on the kinematics
1959 of bivergent orogens: Results from scaled sandbox simulations, *in* Willett, S.D., Hovius,
1960 N., Brandon, M.T., and Fisher, D. eds., *Tectonics, Climate, and Landscape Evolution*,
1961 *Geological Society of America*, v. 398, p. 201–225.
- 1962 Hoth, S., Hoffmann-Rothe, A., and Kukowski, N., 2007, Frontal accretion: An internal clock for
1963 bivergent wedge deformation and surface uplift: *Journal of Geophysical Research*, v.
1964 112, p. B06408–B06408, doi:10.1029/2006JB004357.
- 1965 Ingersoll, R.V., 1990, Actualistic sandstone petrofacies: Discriminating modern and ancient
1966 source rocks: *Geology*, v. 18, p. 733–736.
- 1967 Ingersoll, R.V., Bullard, T.F., Ford, R.L., Grimm, J.P., Pickle, J.D., and Sares, S.W., 1984, The effect
1968 of grain size on detrital modes: A test of the Gazzi-Dickinson point-counting method:
1969 *Journal of Sedimentary Petrology*, v. 54, p. 103–116.

- 1970 Jackson, J., 1992, Partitioning of strike-slip convergent motion between Eurasia and Arabia in
1971 eastern Turkey and the Caucasus: *Journal of Geophysical Research*, v. 97, p. 12,412-
1972 471,479.
- 1973 Jian, D., Williams, S.E., Yu, S., and Zhao, G., 2022, Quantifying the Link Between the Detrital
1974 Zircon Record and Tectonic Settings: *Journal of Geophysical Research: Solid Earth*, v.
1975 127, doi:10.1029/2022JB024606.
- 1976 Jones, R.W., and Simmons, M., 1996, A review of the stratigraphy of Eastern Paratethys
1977 (Oligocene-Holocene): *Bulletin of the Natural History Museum of London*, v. 52, p. 25–
1978 49.
- 1979 Karapetian, S.G., Jrbashian, R.T., and Mnatsakanian, A.Kh., 2001, Late collision rhyolitic
1980 volcanism in the north-eastern part of the Armenian Highland: *Journal of Volcanology
1981 and Geothermal Research*, v. 112, p. 189–220.
- 1982 Khain, V.Ye., 1975, Structure and Main Stages in the Tectono-Magmatic Development of the
1983 Caucasus: An Attempt at Geodynamic Interpretation: *American Journal of Science*, v.
1984 275 A, p. 131–156.
- 1985 Kopp, M.L., and Shcherba, I.G., 1985, Late alpine development of the east Caucasus:
1986 *Geotectonics*, v. 19, p. 497–507.
- 1987 Kovda, I., Mora, C.I., and Wilding, L.P., 2008, PaleoVertisols of the northwest Caucasus:
1988 (Micro)morphological, physical, chemical, and isotopic constraints on early to late
1989 Pliocene climate: *Journal of Plant Nutrition and Soil Science*, v. 171, p. 498–508.
- 1990 Kremenetskiy, A.A., Lapidus, A.V., and Voronovskiy, S.N., 1990, New data on the age and oil and
1991 gas potential of the basement of Kura depression, based on ultradeep well logs: *Doklady
1992 of the National Academy of Sciences of the USSR*, v. 312, p. 139–142.
- 1993 Krijgsman, W. et al., 2019, Quaternary time scales for the Pontocaspian domain: Interbasinal
1994 connectivity and faunal evolution: *Earth-Science Reviews*, v. 188, p. 1–40,
1995 doi:10.1016/j.earscirev.2018.10.013.
- 1996 Krijgsman, W., Stoica, M., Vasiliev, I., and Popov, V.V., 2010, Rise and fall of the Paratethys Sea
1997 during the Messinian salinity crisis: *Earth and Planetary Science Letters*, v. 290, p. 183–
1998 191.
- 1999 Kroonenberg, S.B. et al., 2005, Two deltas, two basins, one river, one sea: The modern Volga
2000 Delta as an analogue for the Neogene Productive Series, South Caspian Basin, *in River
2001 Deltas-Concepts, Models, and Examples*, p. 231–256.
- 2002 Krzanowski, W.J., 2000, *Principles of Multivariate Analysis; A user's perspective* (A. C. Atkinson,
2003 J. B. Copas, D. A. Pierce, M. J. Schervish, & D. M. Titterton, Eds.): Oxford University
2004 Press, 586 p.

- 2005 Kuehn, S.C., Froese, D.G., and Shane, P.A.R., 2011, The INTAV intercomparison of electron-
2006 beam microanalysis of glass by tephrochronology laboratories: Results and
2007 recommendations: *Quaternary International*, v. 246, p. 19–47,
2008 doi:10.1016/j.quaint.2011.08.022.
- 2009 Kvavadze, E., and Vekua, A., 1993, Vegetation and climate of the Dmanisi man period (East
2010 Georgia) from palynological data: *Acta Palaeobotanica*, v. 23, p. 343–355.
- 2011 Lasaga, A.C., Soler, J.M., Ganor, J., Burch, T.E., and Nagy, K.L., 1994, Chemical weathering rate
2012 laws and global geochemical cycles: *Geochimica et Cosmochimica Acta*, v. 58, p. 2361–
2013 2386, doi:10.1016/0016-7037(94)90016-7.
- 2014 Laskowski, A.K., DeCelles, P.G., and Gehrels, G.E., 2013, Detrital zircon geochronology of
2015 Cordilleran retroarc foreland basin strata, western North America: *CORDILLERAN
2016 FORELAND DZ GEOCHRONOLOGY: Tectonics*, v. 32, p. 1027–1048,
2017 doi:10.1002/tect.20065.
- 2018 Lawrence, R.L., Cox, R., Mapes, R.W., and Coleman, D.S., 2011, Hydrodynamic fractionation of
2019 zircon age populations: *Geological Society of America Bulletin*, v. 123, p. 295–305.
- 2020 Lawton, T.F., Hunt, G.J., and Gehrels, G.E., 2010, Detrital zircon record of thrust belt unroofing
2021 in Lower Cretaceous synorogenic conglomerates, central Utah: *Geology*, v. 38, p. 463–
2022 466.
- 2023 Lazarev, S. et al., 2021, Five-fold expansion of the Caspian Sea in the late Pliocene: New and
2024 revised magnetostratigraphic and $^{40}\text{Ar}/^{39}\text{Ar}$ age constraints on the Akchagylian Stage:
2025 *Global and Planetary Change*, v. 206, p. 103624, doi:10.1016/j.gloplacha.2021.103624.
- 2026 Lazarev, S., Jorissen, E.L., van de Velde, S., Rausch, L., Stoica, M., Wesselingh, F.P., Van Baak,
2027 C.G.C., Yanina, T.A., Aliyeva, E., and Krijgsman, W., 2019, Magneto-biostratigraphic age
2028 constraints on the palaeoenvironmental evolution of the South Caspian basin during the
2029 Early-Middle Pleistocene (Kura basin, Azerbaijan): *Quaternary Science Reviews*, v. 222,
2030 p. 105895–105895, doi:10.1016/j.quascirev.2019.105895.
- 2031 Leary, R.J., DeCelles, P.G., Quade, J., Gehrels, G.E., and Waanders, G., 2016, The Liuqu
2032 Conglomerate, southern Tibet: Early Miocene basin development related to
2033 deformation within the Great Counter Thrust system: *Lithosphere*, v. 8, p. 427–450,
2034 doi:10.1130/L542.1.
- 2035 Link, P.K., Fanning, C.M., and Beranek, L.P., 2005, Reliability and longitudinal change of detrital-
2036 zircon age spectra in the Snake River system, Idaho and Wyoming: An example of
2037 reproducing the bumpy barcode: *Sedimentary Geology*, v. 182, p. 101–142.
- 2038 Lowe, D.J., 2011, Tephrochronology and its application: A review: *Quaternary Geochronology*,
2039 v. 6, p. 107–153, doi:10.1016/j.quageo.2010.08.003.

- 2040 Lowe, D.J., Pearce, N.J.G., Jorgensen, M.A., Kuehn, S.C., Tryon, C.A., and Hayward, C.L., 2017,
2041 Correlating tephras and cryptotephras using glass compositional analyses and numerical
2042 and statistical methods: Review and evaluation: *Quaternary Science Reviews*, v. 175, p.
2043 1–44, doi:10.1016/j.quascirev.2017.08.003.
- 2044 Malkowski, M.A., Sharman, G.R., Johnstone, S.A., Grove, M.J., Kimbrough, D.L., and Graham,
2045 S.A., 2019, Dilution and propagation of provenance trends in sand and mud:
2046 Geochemistry and detrital zircon geochronology of modern sediment from central
2047 California (U.S.A.): *American Journal of Science*, v. 319, p. 846–902,
2048 doi:10.2475/10.2019.02.
- 2049 Mamedov, A.V., 1973, Geological structure of the Mid-Kura Depression (in Russian): Baku, Elm.
- 2050 Martín-Fernández, J.A., Barceló-Vidal, C., and Pawlowsky-Glahn, V., 2003, Dealing with zeros and
2051 missing values in compositional data sets using nonparametric imputation:
2052 *Mathematical Geology*, v. 35, p. 253–278.
- 2053 Mayringer, F., Treloar, P.J., Gerdes, A., Finger, F., and Shengelia, D.M., 2011, New age data from
2054 the Dzirula Massif, Georgia: Implications for the evolution of the Caucasian Variscides:
2055 *American Journal of Science*, v. 311, p. 404–441.
- 2056 McKenzie, D., Jackson, J., and Priestley, K., 2019, Continental collisions and the origin of
2057 subcrustal continental earthquakes: *Canadian Journal of Earth Sciences*, v. 56, p. 1101–
2058 1118, doi:10.1139/cjes-2018-0289.
- 2059 Messenger, E., Lordkipanidze, D., Delhon, C., and Ferring, C.R., 2010a, Palaeoecological
2060 implications of the Lower Pleistocene phytolith record from the Dmanisi Site (Georgia):
2061 *Palaeogeography, Palaeoclimatology, Palaeoecology*, v. 288, p. 1–13,
2062 doi:10.1016/j.palaeo.2010.01.020.
- 2063 Messenger, E., Lordkipanidze, D., Kvavadze, E., Ferring, C.R., and Voinchet, P., 2010b,
2064 Palaeoenvironmental reconstruction of Dmanisi site (Georgia) based on palaeobotanical
2065 data: *Quaternary International*, v. 223–224, p. 20–27.
- 2066 Morton, A.C., Allen, M.B., Simmons, M., Spathopoulos, F., Still, J., Hinds, D.J., Ismail-Zadeh, A.,
2067 and Kroonenberg, S.B., 2003, Provenance patterns in a neotectonic basin: Pliocene and
2068 Quaternary sediment supply to the South Caspian: *Basin Research*, v. 15, p. 321–337.
- 2069 Morton, A.C., and Yaxley, G., 2007, Detrital apatite geochemistry and its application in
2070 provenance studies, *in* Arribas, J., Critelli, S., and Johnsson, M.J. eds., *Sedimentary
2071 provenance and petrogenesis: Perspectives from petrography and geochemistry*, p.
2072 319–344.
- 2073 Mosar, J., Kangarli, T., Bochud, M., Glasmacher, U.A., Rast, A., Brunet, M.-F., and Sosson, M.,
2074 2010, Cenozoic-Recent tectonics and uplift in the Greater Caucasus: a perspective from
2075 Azerbaijan, *in* Sosson, M., Kaymakci, N., Stephenson, R.A., Bergerat, F., and Starostenko,

- 2076 V.I. eds., *Sedimentary Basin Tectonics from the Black Sea and Caucasus to the Arabian*
2077 *Platform*, London, Geological Society, v. 340, p. 261–280.
- 2078 Mumladze, T., Forte, A.M., Cowgill, E., Trexler, C.C., Niemi, N.A., Yikilmaz, M.B., and Kellogg,
2079 L.H., 2015, Subducted, detached, and torn slabs beneath the Greater Caucasus:
2080 *GeoResJ*, v. 5, p. 36–46, doi:10.1016/j.grj.2014.09.004.
- 2081 Nagel, S., Castelltort, S., Garzanti, E., Lin, A.T., Willett, S.D., Mouthereau, F., Limonta, M., and
2082 Adatte, T., 2014, Provenance Evolution During Arc-Continent Collision: Sedimentary
2083 Petrography of Miocene To Pleistocene Sediments In the Western Foreland Basin of
2084 Taiwan: *Journal of Sedimentary Research*, v. 84, p. 513–528, doi:10.2110/jsr.2014.44.
- 2085 Nesbitt, H.W., and Young, G.M., 1982, Early Proterozoic climates and plate motions inferred
2086 from major element chemistry of lutites: *Nature*, v. 299, p. 715–717.
- 2087 Ogg, J.G., 2020, Geomagnetic Polarity Time Scale, *in* Gradstein, F.M., Ogg, J.G., Schmitz, M.D.,
2088 and Ogg, G.M. eds., *Geologic Time Scale*, Elsevier, v. 1, p. 159–192.
- 2089 Palcu, D.V., Vasiliev, I., Stoica, M., and Krijgsman, W., 2019, The end of the Great Khersonian
2090 Drying of Eurasia: Magnetostratigraphic dating of the Maeotian transgression in the
2091 Eastern Paratethys: *Basin Research*, v. 31, p. 33–58, doi:10.1111/bre.12307.
- 2092 Panaiotu, C.E., Vasiliev, I., Panaiotu, C.G., Krijgsman, W., and Langereis, C.G., 2007, Provenance
2093 analysis as a key to orogenic exhumation: a case study from the East Carpathians
2094 (Romania): *Terra Nova*, v. 19, p. 120–126.
- 2095 Pawlowsky-Glahn, V., and Egozcue, J.J., 2006, Compositional data and their analysis: an
2096 introduction, *in* Buccianti, A., Mateu-Figueras, G., and Pawlowsky-Glahn, V. eds.,
2097 *Compositional data analysis in the geosciences: From theory to practice*, London,
2098 Geological Society, v. 264, p. 1–10.
- 2099 Pe-Piper, G., Triantafyllidis, S., and Piper, D.J.W., 2008, Geochemical identification of clastic
2100 sediment provenance from known sources of similar geology: The Cretaceous Scotian
2101 Basin, Canada: *Journal of Sedimentary Research*, v. 78, p. 595–607.
- 2102 Perkins, M.E., Nash, W.P., Brown, F.H., and Fleck, R.J., 1995, Fallout tuffs of Trapper Creek,
2103 Idaho—A record of Miocene explosive volcanism in the Snake River Plain volcanic
2104 province: *Geological Society of America Bulletin*, p. 23.
- 2105 Philip, H., Cisternas, A., Gvishiani, A., and Gorshkov, A., 1989, The Caucasus: an actual example
2106 of the initial stages of continental collision: *Tectonophysics*, v. 161, p. 1–21.
- 2107 Popov, S.V., Antipov, M.P., Zastroshnov, A.S., Kurina, E.E., and Pinchuk, T.N., 2010, Sea-level
2108 fluctuations on the northern shelf of the eastern Paratethys in the Oligocene-Neogene:
2109 *Stratigraphy and Geological Correlation*, v. 18, p. 200–224.

- 2110 Popov, S.V., Shcherba, I.G., Ilyina, L.B., Neveeskaya, L.A., Paramonova, N.P., Khondkarian, S.O.,
2111 and Magyar, I., 2006, Late Miocene to Pliocene palaeogeography of the Paratethys and
2112 its relation to the Mediterranean: Palaeogeography, Palaeoclimatology, Palaeoecology,
2113 v. 238, p. 91–106.
- 2114 Raines, K.M., Hubbard, S.M., Kukulski, R.B., Leier, A.L., and Gehrels, G.E., 2013, Sediment
2115 dispersal in an evolving foreland: Detrital zircon geochronology from Upper Jurassic and
2116 lowermost Cretaceous strata, Alberta Basin, Canada: Geological Society of America
2117 Bulletin, doi:10.1130/B30671.1.
- 2118 Reilinger, R. et al., 2006, GPS constraints on continental deformation in the Africa-Arabia-
2119 Eurasia continental collision zone and implications for the dynamics of plate
2120 interactions: Journal of Geophysical Research, v. 111, p. doi:10.1029/2005JB004051-
2121 doi:10.1029/2005JB004051.
- 2122 Reynolds, A.D. et al., 1998, Implications of Outcrop Geology for Reservoirs in the Neogene
2123 Productive Series: Apsheron Peninsula, Azerbaijan: American Association of Petroleum
2124 Geologists Bulletin, v. 82, p. 25–49.
- 2125 Richards, K., van Baak, C.G.C., Athersuch, J., Hoyle, T.M., Stoica, M., Austin, W.E.N., Cage, A.G.,
2126 Wonders, A.A.H., Marret, F., and Pinnington, C.A., 2018, Palynology and
2127 micropalaeontology of the Pliocene - Pleistocene transition in outcrop from the western
2128 Caspian Sea, Azerbaijan: Potential links with the Mediterranean, Black Sea and the Arctic
2129 Ocean? Palaeogeography, Palaeoclimatology, Palaeoecology, v. 511, p. 119–143,
2130 doi:10.1016/j.palaeo.2018.07.018.
- 2131 Roe, G.H., Whipple, K.X., and Fletcher, J.K., 2008, Feedbacks among climate, erosion, and
2132 tectonics in a critical wedge orogen: American Journal of Science, v. 308, p. 815–842,
2133 doi:10.2475/07.2008.01.
- 2134 Rolland, Y., Sosson, M., Adamia, Sh., and Sadradze, N., 2011, Prolonged Variscan to Alpine
2135 history of an active Eurasian margin (Georgia, Armenia) revealed by ⁴⁰Ar/³⁹Ar dating:
2136 Gondwana Research, v. 20, p. 798–815, doi:10.1016/j.gr.2011.05.007.
- 2137 Roman, D.C., Campisano, C., Quade, J., DiMaggio, E., Arrowsmith, J.R., and Feibel, C., 2008,
2138 Composite tephrostratigraphy of the Dikika, Gona, Hadar, and Ledi-Geraru project
2139 areas, northern Awash, Ethiopia, *in* The Geology of Early Humans in the Horn of Africa,
2140 Geological Society of America, doi:10.1130/2008.2446(05).
- 2141 Roser, B.P., and Korsch, R.J., 1986, Determination of tectonics setting of sandstone-mudstone
2142 suites using SiO₂ and K₂O/Na₂O ratio: The Journal of Geology, v. 94, p. 635–650.
- 2143 Roser, B.P., and Korsch, R.J., 1988, Provenance signatures of sandstone-mudstone suites
2144 determined using discriminant function analysis of major-element data: Chemical
2145 Geology, v. 67, p. 119–139.

- 2146 Safonova, I., Maruyama, S., Hirata, T., Kon, Y., and Rino, S., 2010, LA ICP MS U-Pb ages of
2147 detrital zircons from Russia largest rivers: Implications for major granitoid events in
2148 Eurasia and global episodes of supercontinent formation: *Journal of Geodynamics*, v. 50,
2149 p. 134–153.
- 2150 Saintot, A., Brunet, M.-F., Yakovlev, F., Sebrier, M., Stephenson, R.A., Ershov, A.V., Chalot-Prat,
2151 F., and McCann, T., 2006, The Mesozoic-Cenozoic tectonic evolution of the Greater
2152 Caucasus, *in* Gee, D.G. and Stephenson, R.A. eds., *European Lithosphere Dynamics*,
2153 London, Geological Society, v. 32.
- 2154 Saylor, J.E., and Sundell, K.E., 2016, Quantifying comparison of large detrital geochronology
2155 data sets: *Geosphere*, v. 12, p. 203–220, doi:10.1130/GES01237.1.
- 2156 Shcherbakov, V., Bindeman, I., and Gazeev, V., 2022, Geochemical, Isotopic and Petrological
2157 Constraints on the Origin and Evolution of the Recent Silicic Magmatism of the Greater
2158 Caucasus: *Minerals*, v. 12, p. 105, doi:10.3390/min12010105.
- 2159 Shengelia, D., Shubitidze, L., Chung, S.-L., Chiu, H.-Y., and Treloar, P., 2012, New Data on the
2160 Formation and Age of Orthoclase Gabbro of the Dzirula Crystalline Massif (Georgia): v. 6.
- 2161 Shikalibeily, E.Sh., Abdullayev, R.N., and Ali-Zade, Ak.A., 1988, Geological results from the Saatly
2162 superdeep drillhole: *International Geology Review*, v. 30, p. 1272–1277.
- 2163 Shimodaira, H., 2004, Approximately unbiased tests of regions using multistep-multiscale boot-
2164 strap resampling: *Annals of Statistics*, v. 32, p. 2616–2641.
- 2165 Sinclair, H.D., 1997, Flysch to molasse transition in peripheral foreland basins: The role of the
2166 passive margin versus slab breakoff: *Geology*, v. 25, p. 1123–1126.
- 2167 Skolbeltsyn, G., Mellors, R., Gök, R., Türkelli, N., Yetirmishli, G., and Sandvol, E., 2014, Upper
2168 mantle S wave velocity structure of the East Anatolian-Caucasus region: *Tectonics*, v. 33,
2169 p. 207–221, doi:10.1002/2013TC003334.
- 2170 Smosna, R., Bruner, K.R., and Burns, A., 1999, Numerical analysis of sandstone composition,
2171 provenance, and paleogeography: *Journal of Sedimentary Research*, v. 69, p. 1063–
2172 1070.
- 2173 Sobornov, K.O., 1996, Lateral variations in structural styles of tectonic wedging in the
2174 northeastern Caucasus: *Bulletin of Canadian Petroleum Geology*, v. 44, p. 385–399.
- 2175 Sobornov, K., 2021, STRUCTURE AND EVOLUTION OF THE TEREK-CASPIAN FOLD-AND-THRUST
2176 BELT: NEW INSIGHTS FROM REGIONAL SEISMIC DATA: *Journal of Petroleum Geology*, v.
2177 44, p. 259–286, doi:10.1111/jpg.12793.

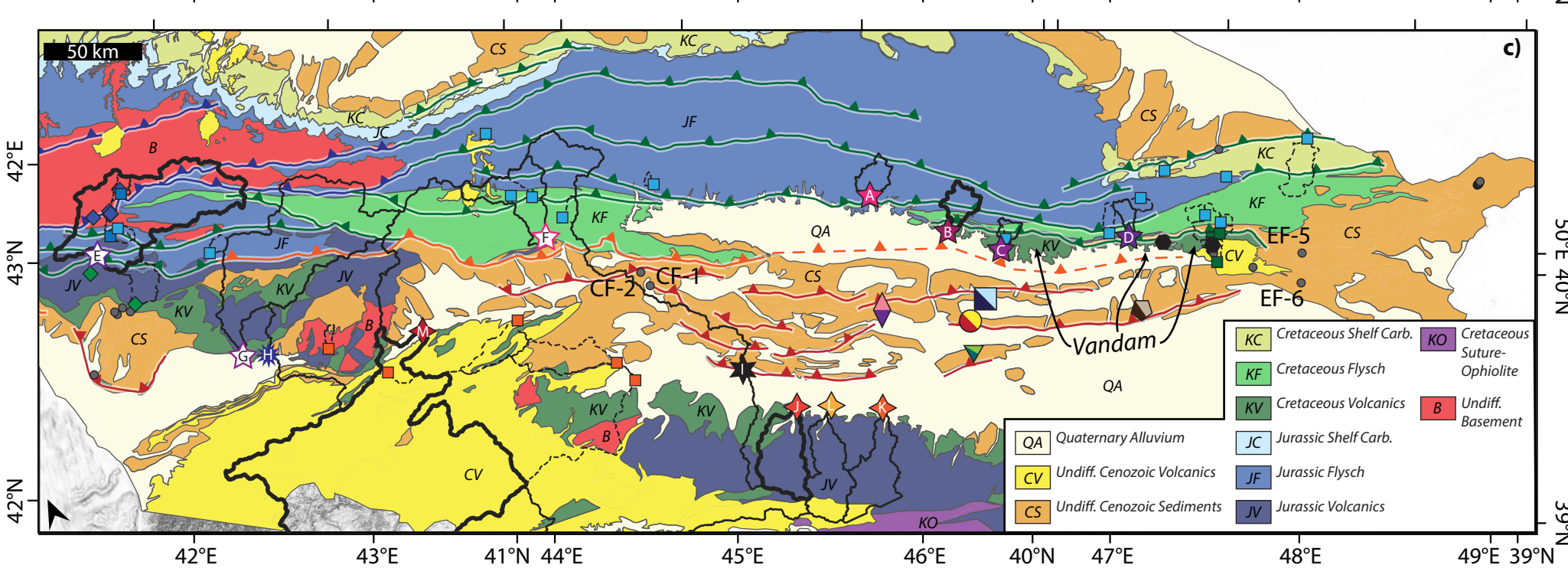
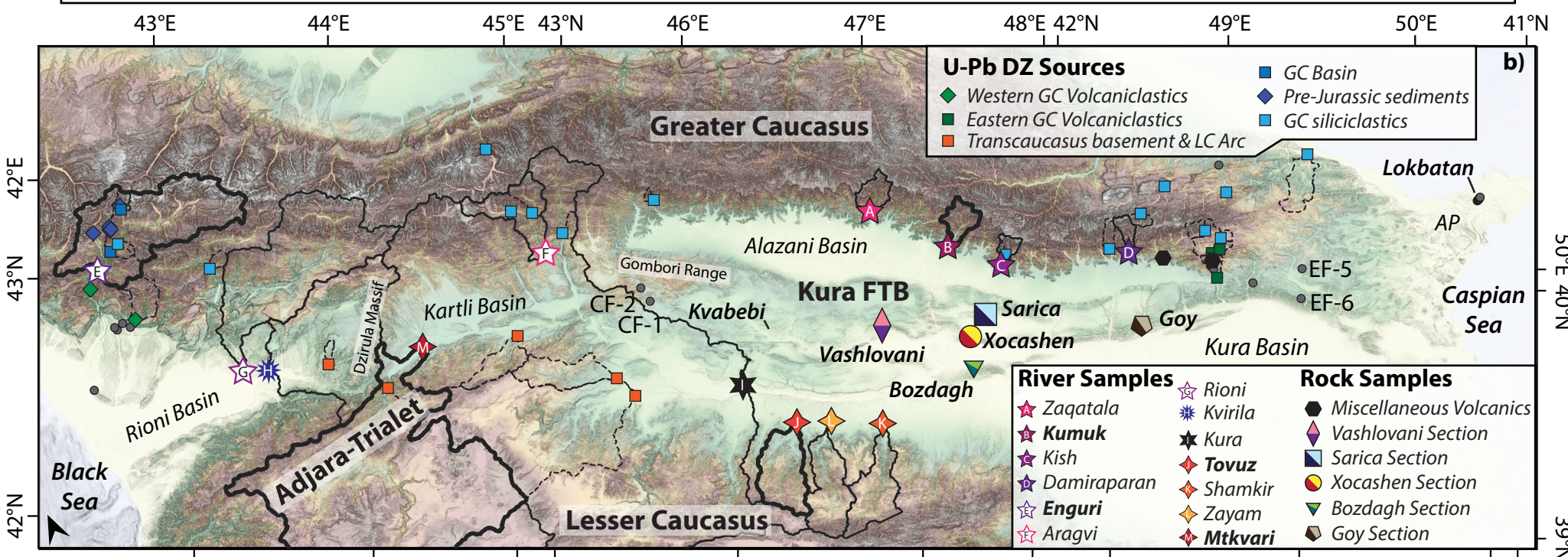
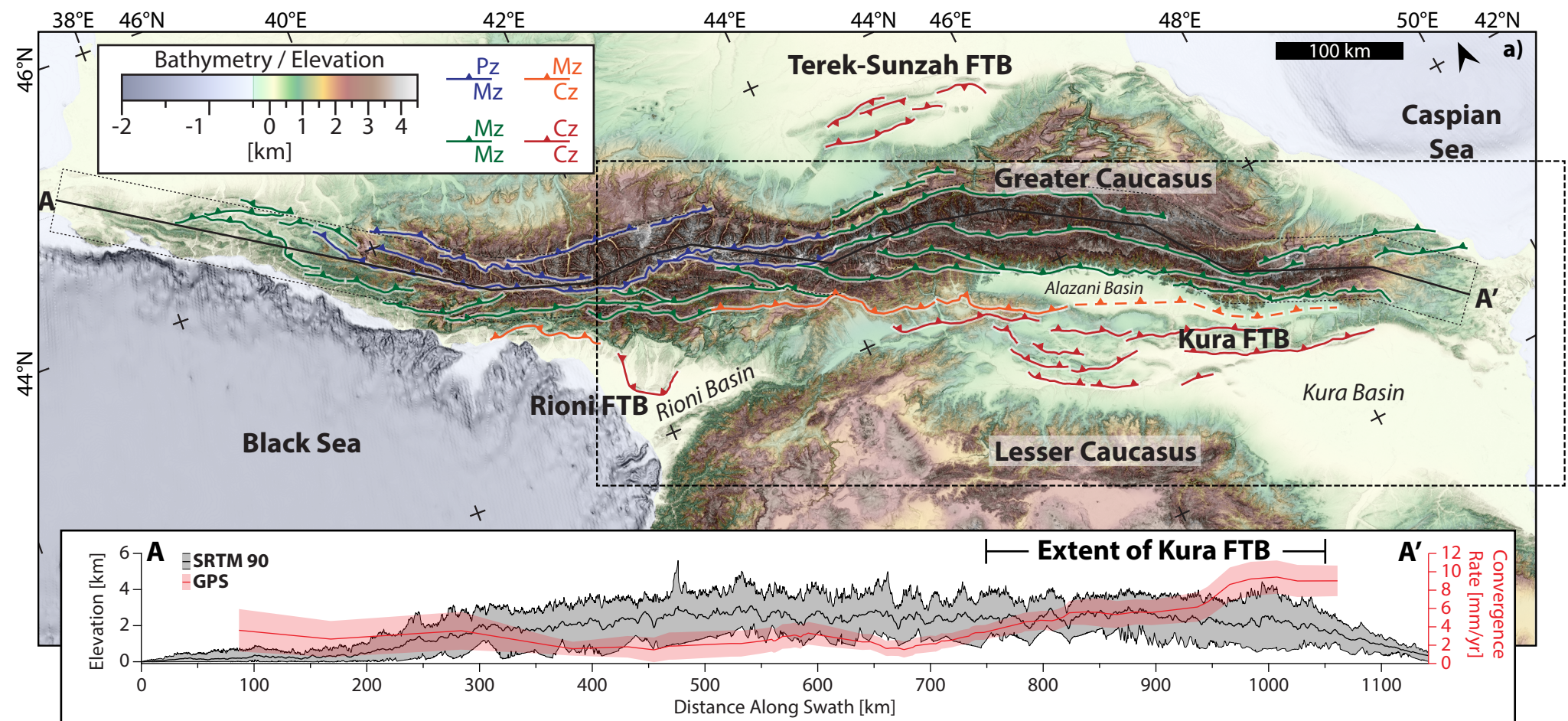
- 2178 Sobornov, K.O., 1994, Structure and petroleum potential of the Dagestan thrust belt,
2179 northeastern Caucasus, Russia: *Bulletin of Canadian Petroleum Geology*, v. 42, p. 352–
2180 364.
- 2181 Somin, M.L., 2011, Pre-Jurassic Basement of the Greater Caucasus: Brief Overview: *Turkish*
2182 *Journal of Earth Sciences*, v. 20, p. 546–610.
- 2183 Spencer, C.J., Kirkland, C.L., Nicholas, M.W., and Spencer, C.J., 2018, Implications of erosion and
2184 bedrock composition on zircon fertility; examples from South America and Western
2185 Australia: *Terra Nova*, v. 30, p. 289–295, doi:10.1111/ter.12338.
- 2186 Stolar, D.B., Willett, S.D., and Roe, G.H., 2006, Climatic and tectonic forcing of a critical orogen,
2187 *in* Willett, S.D., Hovius, N., Brandon, M.T., and Fisher, D. eds., *Tectonics, climate, and*
2188 *landscape evolution*, Geological Society of America, v. 398, p. 241–250.
- 2189 Sukhishvili, L., Forte, A.M., Merebashvili, G., Leonard, J., Whipple, K.X., Javakhishvili, Z.,
2190 Heimsath, A., and Godoladze, T., 2021, Active deformation and Plio-Pleistocene fluvial
2191 reorganization of the western Kura fold–thrust belt, Georgia: implications for the
2192 evolution of the Greater Caucasus Mountains: *Geological Magazine*, v. 158, p. 583–597,
2193 doi:10.1017/S0016756820000709.
- 2194 Sundell, K., and Saylor, J.E., 2017, Unmixing detrital geochronology age distributions:
2195 *Geochemistry, Geophysics, Geosystems*, v. 18, p. 2872–2886,
2196 doi:10.1002/2016GC006774.
- 2197 Suzuki, R., and Shimodaira, H., 2009, pvclust: Hierarchical Clustering with P-values via
2198 Multiscale Bootstrap Resampling; <http://www.is.titech.ac.jp/~shimo/prog/pvclust/>.
- 2199 Team, R.D.C., 2010, R: A language and environment for statistical computing; [http://www.r-](http://www.r-project.org)
2200 [project.org](http://www.r-project.org).
- 2201 Tibaldi, A., Babayev, G., Bonali, F.L., Pasquaré Mariotto, F., Russo, E., Tsereteli, N., and Corti, N.,
2202 2021, Active Kinematics of the Greater Caucasus from Seismological and GPS Data: A
2203 Review, *in* Bonali, F.L., Pasquaré Mariotto, F., and Tsereteli, N. eds., *Building Knowledge*
2204 *for Geohazard Assessment and Management in the Caucasus and other Orogenic*
2205 *Regions*, Dordrecht, Springer Netherlands, NATO Science for Peace and Security Series
2206 C: Environmental Security, p. 33–57, doi:10.1007/978-94-024-2046-3_4.
- 2207 Tibaldi, A., Bonali, F.L., Russo, E., and Pasquaré Mariotto, F.A., 2018, Structural development
2208 and stress evolution of an arcuate fold-and-thrust system, southwestern Greater
2209 Caucasus, Republic of Georgia: *Journal of Asian Earth Sciences*, v. 156, p. 226–245,
2210 doi:10.1016/j.jseaes.2018.01.025.
- 2211 Tibaldi, A., Russo, E., Bonali, F.L., Alania, V., Chabukiani, A., Enukidze, O., and Tsereteli, N., 2017,
2212 3-D anatomy of an active fault-propagation fold: A multidisciplinary case study from

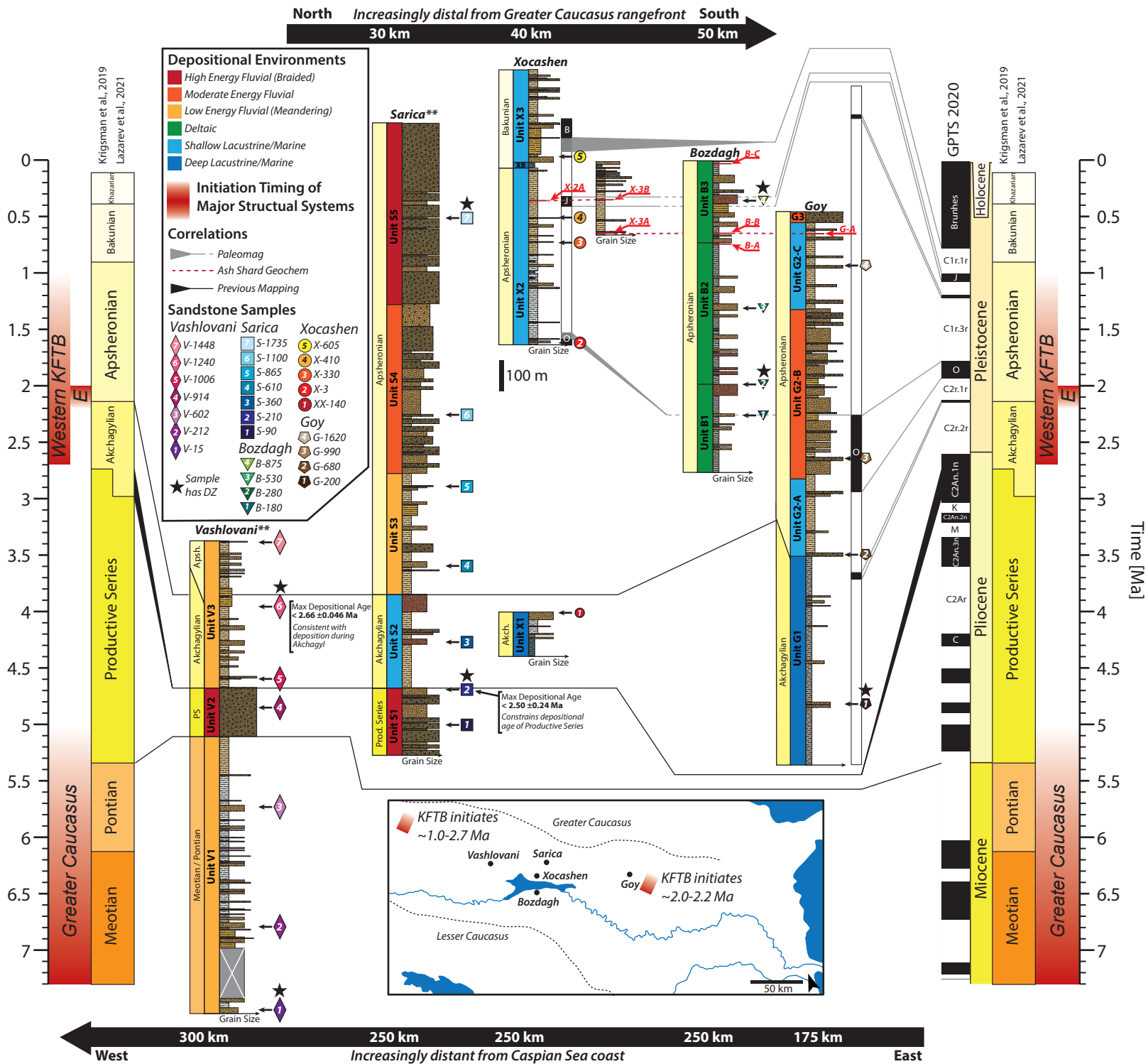
- 2213 Tsaishi, western Caucasus (Georgia): *Tectonophysics*, v. 717, p. 253–269,
2214 doi:10.1016/j.tecto.2017.08.006.
- 2215 Totten, M.W., Hanan, M.A., and Weaver, B.L., 2000, Beyond whole-rock geochemistry of shales:
2216 The importance of assessing mineralogic controls for revealing tectonic discriminants of
2217 multiple sediment sources for the Ouachita Mountain flysch deposits: *Geological Society
2218 of America Bulletin*, v. 112, p. 1012–1022.
- 2219 Trexler, C.C., Cowgill, E.S., Niemi, N.A., Vasey, D.A., and Godoladze, T., 2022,
2220 Tectonostratigraphy and major structures of the Georgian Greater Caucasus:
2221 Implications for structural architecture, along-strike continuity, and orogen evolution:
2222 *Geosphere*, doi:10.1130/GES02385.1.
- 2223 Trexler, C.C., Cowgill, E., Spencer, J.Q.G., and Godoladze, T., 2020, Rate of active shortening
2224 across the southern thrust front of the Greater Caucasus in western Georgia from
2225 kinematic modeling of folded river terraces above a listric thrust: *Earth and Planetary
2226 Science Letters*, v. 544, p. 116362, doi:10.1016/j.epsl.2020.116362.
- 2227 Trexler, C.C., Cowgill, E.S., Vasey, D.A., and Niemi, N.A., 2023, Total Shortening Estimates Across
2228 the Western Greater Caucasus Mountains from Balanced Cross Sections and Area
2229 Balancing: *Tektonika*, v. 1, doi:10.55575/tektonika2023.1.2.50.
- 2230 Tsereteli, N., Tibaldi, A., Alania, V., Gventsadse, A., Ehlukidze, O., Varazanashvili, O., and Müller,
2231 B.I.R., 2016, Active tectonics of central-western Caucasus, Georgia: *Tectonophysics*, v.
2232 691, p. 328–344, doi:10.1016/j.tecto.2016.10.025.
- 2233 Tye, A.R., Niemi, N.A., Cowgill, E., Kadirov, F.A., and Babayev, G.R., 2022, Diverse Deformation
2234 Mechanisms and Lithologic Controls in an Active Orogenic Wedge: *Structural Geology
2235 and Thermochronometry of the Eastern Greater Caucasus: Tectonics*, v. 41,
2236 doi:10.1029/2022TC007349.
- 2237 Tye, A.R., Niemi, N.A., Safarov, R.T., Kadirov, F.A., and Babayev, G.R., 2020, Sedimentary
2238 response to a collision orogeny recorded in detrital zircon provenance of Greater
2239 Caucasus foreland basin sediments: *Basin Research*, p. bre.12499,
2240 doi:10.1111/bre.12499.
- 2241 Tye, A.R., Wolf, A.S., and Niemi, N.A., 2019, Bayesian population correlation: A probabilistic
2242 approach to inferring and comparing population distributions for detrital zircon ages:
2243 *Chemical Geology*, doi:10.1016/J.CHEMGEO.2019.03.039.
- 2244 Van Baak, C.G.C., Stoica, M., Grothe, A., Aliyeva, E., and Krijgsman, W., 2016, Mediterranean-
2245 Paratethys connectivity during the Messinian salinity crisis: The Pontian of Azerbaijan:
2246 *Global and Planetary Change*, v. 141, p. 63–81, doi:10.1016/j.gloplacha.2016.04.005.
- 2247 Vasey, D.A., Cowgill, E., and Cooper, K.M., 2021, A Preliminary Framework for Magmatism in
2248 Modern Continental Back-Arc Basins and Its Application to the Triassic-Jurassic Tectonic

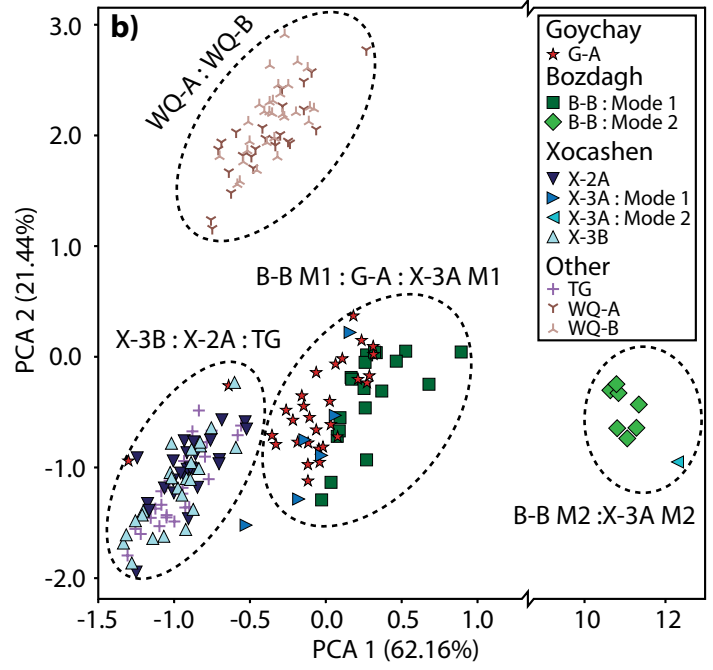
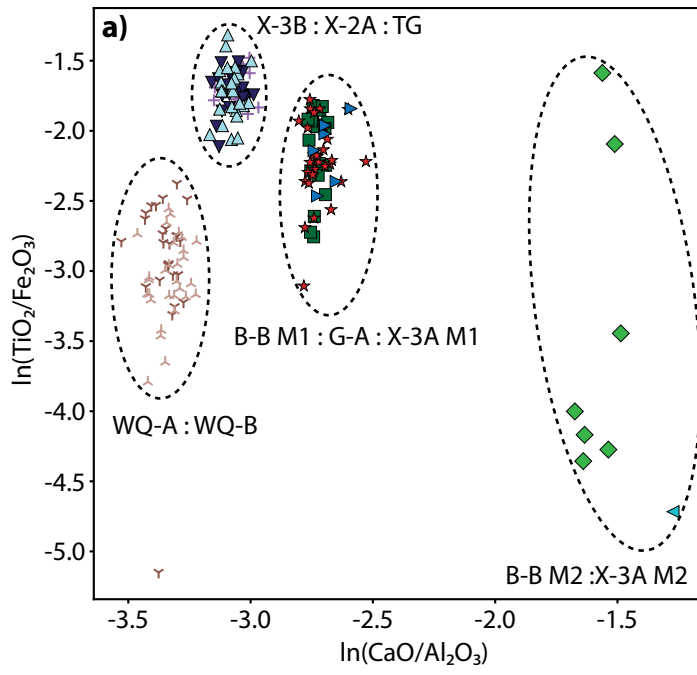
- 2249 Evolution of the Caucasus: Geochemistry, Geophysics, Geosystems, v. 22,
2250 doi:10.1029/2020GC009490.
- 2251 Vasey, D.A., Cowgill, E., Roeske, S.M., Niemi, N.A., Godoladze, T., Skhirtladze, I., and Gogoladze,
2252 S., 2020, Evolution of the Greater Caucasus Basement and Formation of the Main
2253 Caucasus Thrust, Georgia: Tectonics, v. 39, doi:10.1029/2019TC005828.
- 2254 Vasey, D.A., Garcia, L., Cowgill, E., Trexler, C.C., and Godoladze, T., 2024, Episodic evolution of a
2255 protracted convergent margin revealed by detrital zircon geochronology in the Greater
2256 Caucasus: Basin Research, v. 36, p. e12825, doi:10.1111/bre.12825.
- 2257 Vasiliev, I. et al., 2022, Biomarkers reveal two paramount Pliocene-Pleistocene connectivity
2258 events in the Caspian Sea Basin: Palaeogeography, Palaeoclimatology, Palaeoecology, v.
2259 587, p. 110802, doi:10.1016/j.palaeo.2021.110802.
- 2260 Vasiliev, I., Iosifidi, A.G., Khramov, A.N., Krijgsman, W., Kuiper, K.F., Langereis, C.G., Popov, V.V.,
2261 Stoica, M., Tomsha, V.A., and Yudin, S.V., 2011, Magnetostratigraphy and radio-isotope
2262 dating of upper Miocene-lower Pliocene sedimentary successions of the Black Sea Basin
2263 (Taman Peninsula, Russia): Palaeogeography, Palaeoclimatology, Palaeoecology, v. 310,
2264 p. 163–175.
- 2265 Venables, W.N., and Ripley, B.D., 2002, Modern Applied Statistics with S: New York, Springer-
2266 Verlag, 495 p.
- 2267 Vermeesch, P., 2013, Multi-sample comparison of detrital age distributions: Chemical Geology,
2268 v. 341, p. 140–146, doi:10.1016/j.chemgeo.2013.01.010.
- 2269 Vermeesch, P., 2012, On the visualization of detrital age distributions: Chemical Geology, v.
2270 312–313, p. 190–194.
- 2271 Vezzoli, G., Garzanti, E., Limonta, M., and Radeff, G., 2020, Focused erosion at the core of the
2272 Greater Caucasus: Sediment generation and dispersal from Mt. Elbrus to the Caspian
2273 Sea: Earth-Science Reviews, v. 200, p. 102987, doi:10.1016/j.earscirev.2019.102987.
- 2274 Vezzoli, G., Garzanti, E., Vincent, S.J., Ando, S., Carter, A., and Resentini, A., 2014, Tracking
2275 sediment provenance and erosional evolution of the western Greater Caucasus: Earth
2276 Surface Processes and Landforms, doi:10.1002/esp.3567.
- 2277 Vincent, S.J., Braham, W., Lavrishchev, V.A., Maynard, J.R., and Harland, M., 2016, The
2278 formation and inversion of the western Greater Caucasus Basin and the uplift of the
2279 western Greater Caucasus: Implications for the wider Black Sea region: Tectonics, v. 35,
2280 p. 2948–2962, doi:10.1002/2016TC004204.
- 2281 Vincent, S.J., Davies, C.E., Richards, K., and Aliyeva, E., 2010, Contrasting Pliocene fluvial
2282 depositional systems within the rapidly subsiding South Caspian Basin; a case study of
2283 the palaeo-Volga and palaeo-Kura river systems in the Surakhany Suite, Upper

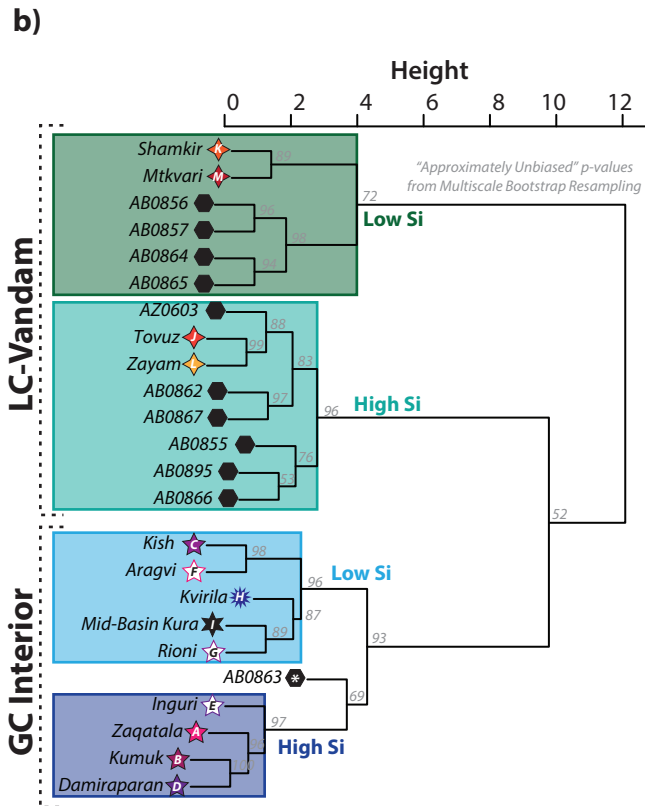
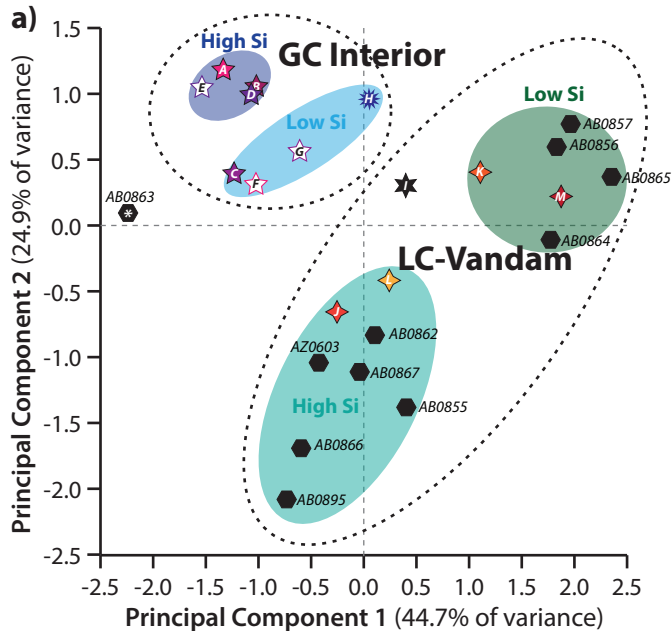
- 2284 Productive Series, onshore Azerbaijan: *Marine and Petroleum Geology*, v. 27, p. 2079–
2285 2106.
- 2286 Vincent, S.J., Hyden, F., and Braham, W., 2014, Along-strike variations in the composition of
2287 sandstones derived from the uplifting western Greater Caucasus: causes and
2288 implications for reservoir quality prediction in the Eastern Black Sea, *in* Scott, R.A.,
2289 Smyth, H.R., Morton, A.C., and Richardson, N. eds., *Sediment Provenance Studies in*
2290 *Hydrocarbon Exploration and Production*, London, Geological Society, p. 11–127,
2291 doi:10.1144/SP386.15.
- 2292 Vincent, S.J., Morton, A.C., Carter, A., Gibbs, S., and Teimuraz, G.B., 2007, Oligocene uplift of
2293 the Western Greater Caucasus: an effect of initial Arabia-Eurasia collision: *Terra Nova*, v.
2294 19, p. 160–166.
- 2295 Vincent, S.J., Morton, A.C., Hyden, F., and Fanning, M., 2013, Insights from petrography,
2296 mineralogy and U-Pb zircon geochronology into the provenance and reservoir potential
2297 of Cenozoic siliciclastic depositional systems supplying the northern margin of the
2298 northern margin of the Eastern Black Sea: *Marine and Petroleum Geology*, v. 45, p. 331–
2299 348.
- 2300 Vincent, S.J., Saintot, A., Mosar, J., Okay, A.I., and Nikishin, A.M., 2018, Comment on “Relict
2301 basin closure and crustal shortening budgets during continental collision: An example
2302 from Caucasus sediment provenance” by Cowgill et al (2016): *Tectonics*, v. 37, p. 1006–
2303 1016, doi:10.1002/2017TC004515.
- 2304 Vincent, S.J., Somin, M.L., Carter, A., Vezzoli, G., Fox, M., and Vautravers, B., 2020, Testing
2305 Models of Cenozoic Exhumation in the Western Greater Caucasus: *Tectonics*, v. 39,
2306 doi:10.1029/2018TC005451.
- 2307 Von Eynatten, H., 2003, Petrography and chemistry of sandstones from the Swiss Molasse
2308 Basin: an archive of the Oligocene to Miocene evolution of the Central Alps:
2309 *Sedimentology*, v. 50, p. 703–724, doi:10.1046/j.1365-3091.2003.00571.x.
- 2310 Von Eynatten, H., Barceló-Vidal, C., and Pawlowsky-Glahn, V., 2003, Composition and
2311 discrimination of sandstones: A statistical evaluation of different analytical methods:
2312 *Journal of Sedimentary Research*, v. 73, p. 47–57.
- 2313 Wang, C.Y., Campbell, I.H., Stepanov, A.S., Allen, C.M., and Burtsev, I.N., 2011, Growth rate of
2314 the preserved continental crust: II. Constraints from Hf and O isotopes in detrital zircons
2315 from Greater Russian Rivers: *Geochimica et Cosmochimica Acta*, v. 75, p. 1308–1345.
- 2316 Whipple, K.X., and Meade, B., 2004, Controls on the strength of coupling among climate,
2317 erosion, and deformation in two-sided, frictional orogenic wedges at steady state:
2318 *Journal of Geophysical Research*, v. 109, p. F01011–F01011, doi:10.1029/2003JF000019.

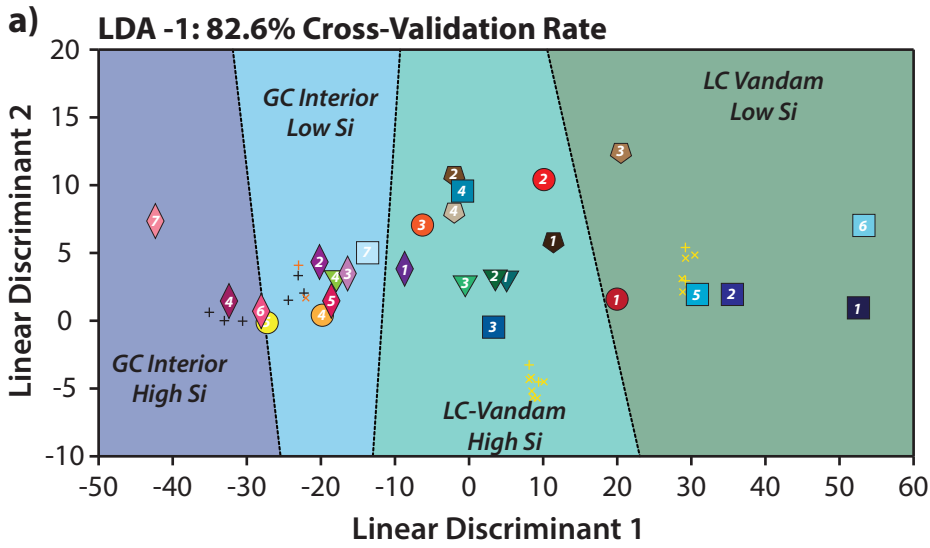
- 2319 Whipple, K.X., and Meade, B., 2006, Orogen response to changes in climatic and tectonic
2320 forcing: *Earth and Planetary Science Letters*, v. 243, p. 218–228.
- 2321 Žák, J., Svojtka, M., Hajná, J., and Ackerman, L., 2020, Detrital zircon geochronology and
2322 processes in accretionary wedges: *Earth-Science Reviews*, v. 207, p. 103214,
2323 doi:10.1016/j.earscirev.2020.103214.
- 2324 Zakariadze, G., Karpenko, S., Bazylev, B., Solov'eva, N., Lyalikov, A., Adamia, S.A., and
2325 Oberhänsli, R., 1998, Petrology, geochemistry, and Sm-Nd age of the pre-Late Hercynian
2326 paleoceanic complex of the Dzirula salient, Transcaucasian Massif: *Petrology*, v. 6, p.
2327 388–408.
- 2328 Zonenshain, L.P., and Le Pichon, X., 1986, Deep basins of the Black Sea and Caspian Sea as
2329 remnants of Mesozoic back-arc basins: *Tectonophysics*, v. 123, p. 181–211.
- 2330 Zubakov, V.A., and Borzenkova, I.I., 1990, *Global palaeoclimate of the Late Cenozoic:*
2331 *Amsterdam, Elsevier.*
- 2332











Sarica

- 7 S-1735
- 6 S-1100
- 5 S-865
- 4 S-610
- 3 S-360
- 2 S-210
- 1 S-90

Goy

- 4 G-1620
- 3 G-990
- 2 G-680
- 1 G-200

Vashlovani

- 7 V-1448
- 6 V-1240
- 5 V-1006
- 4 V-914
- 3 V-602
- 2 V-212
- 1 V-15

Xocashen

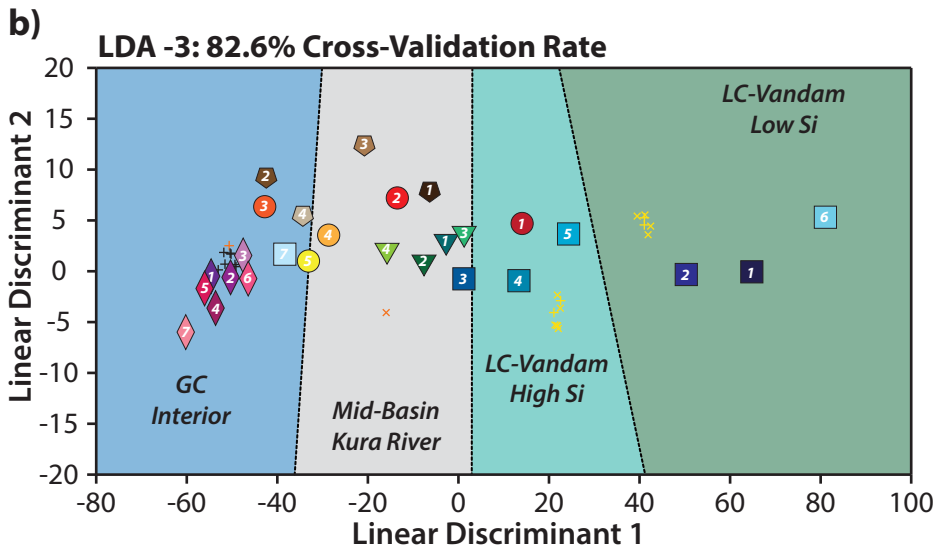
- 5 X-605
- 4 X-410
- 3 X-330
- 2 X-3
- 1 XX-140

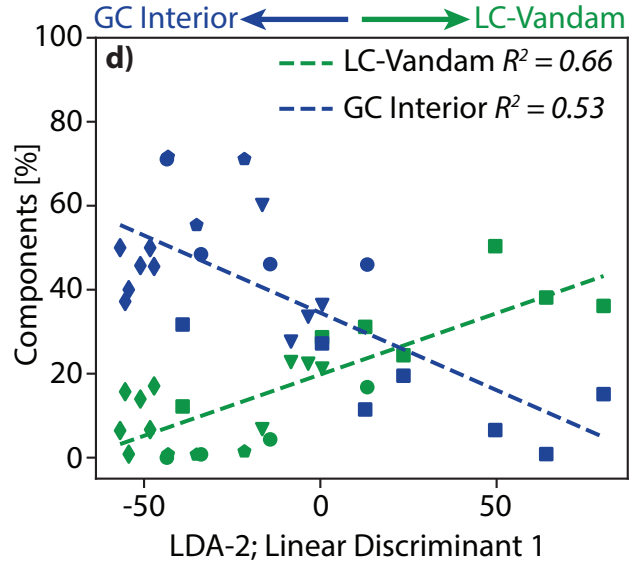
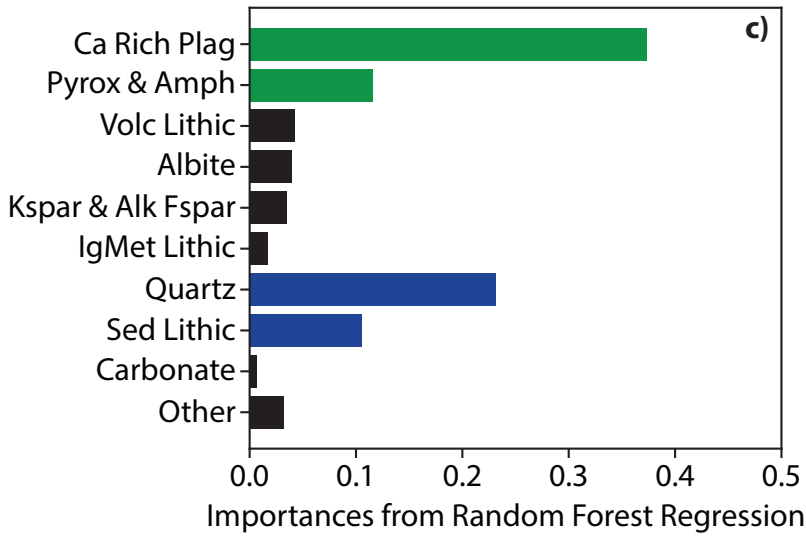
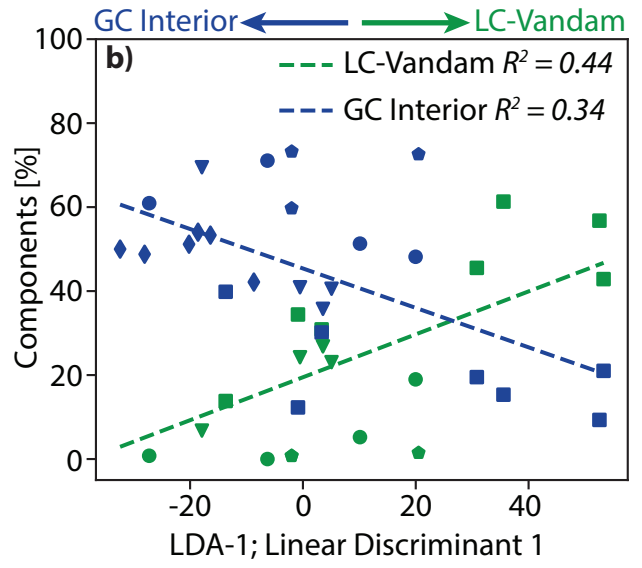
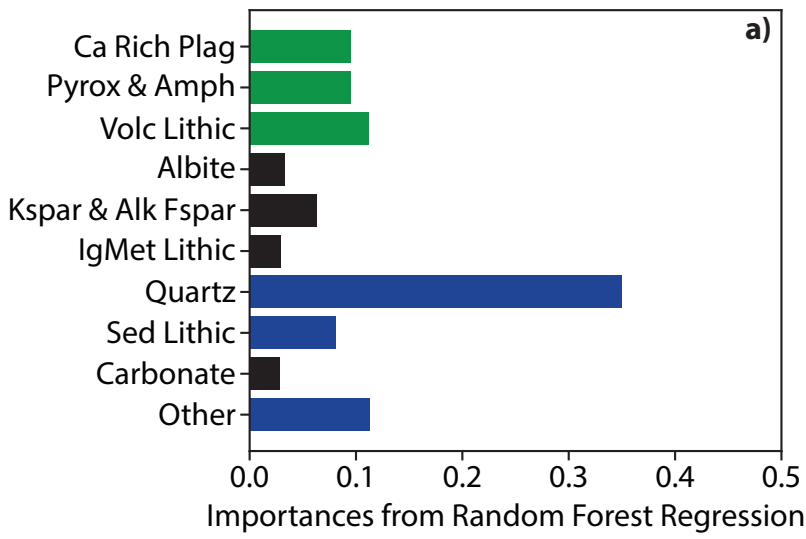
Bozdagh

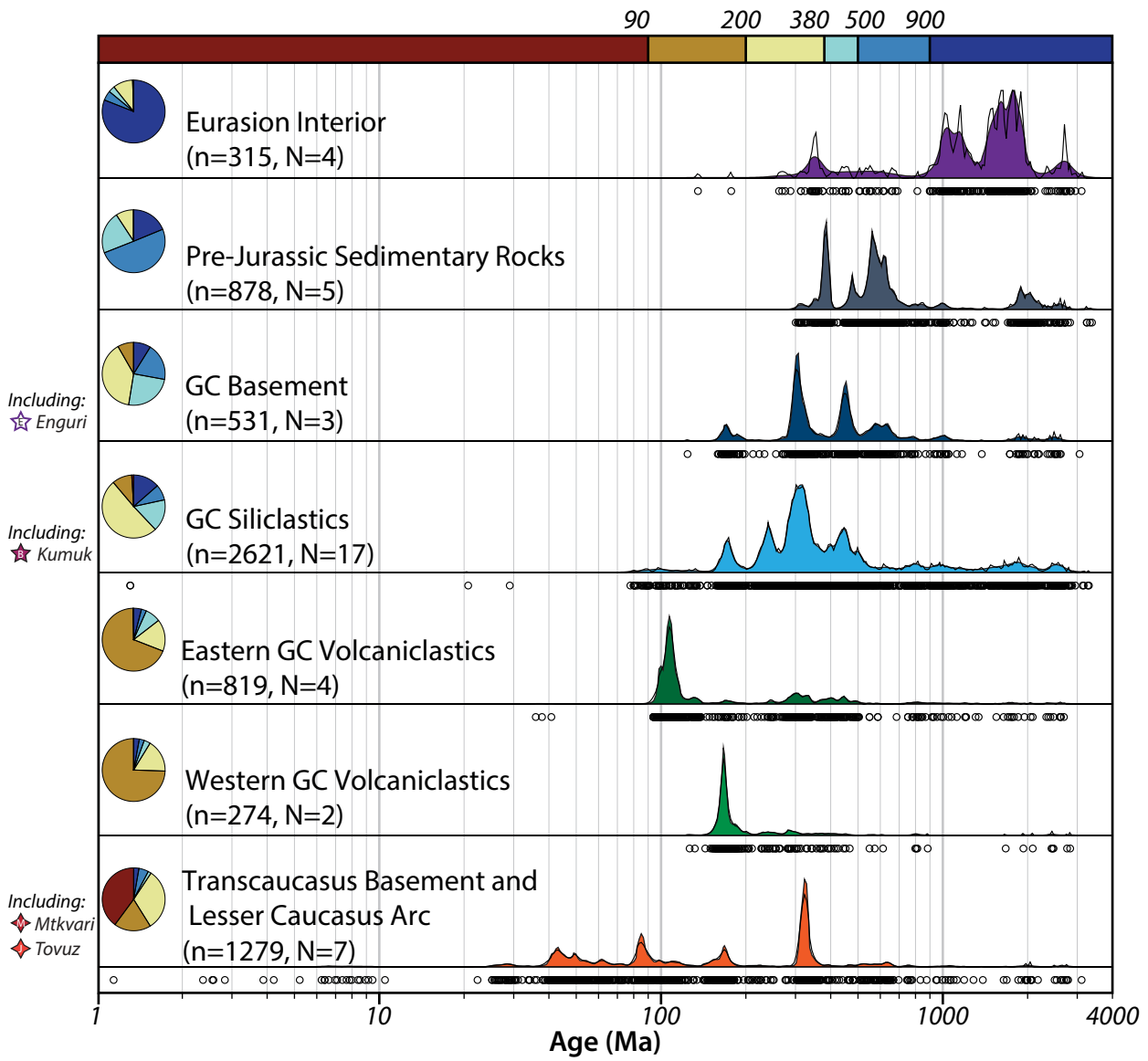
- 4 B-875
- 3 B-530
- 2 B-280
- 1 B-180

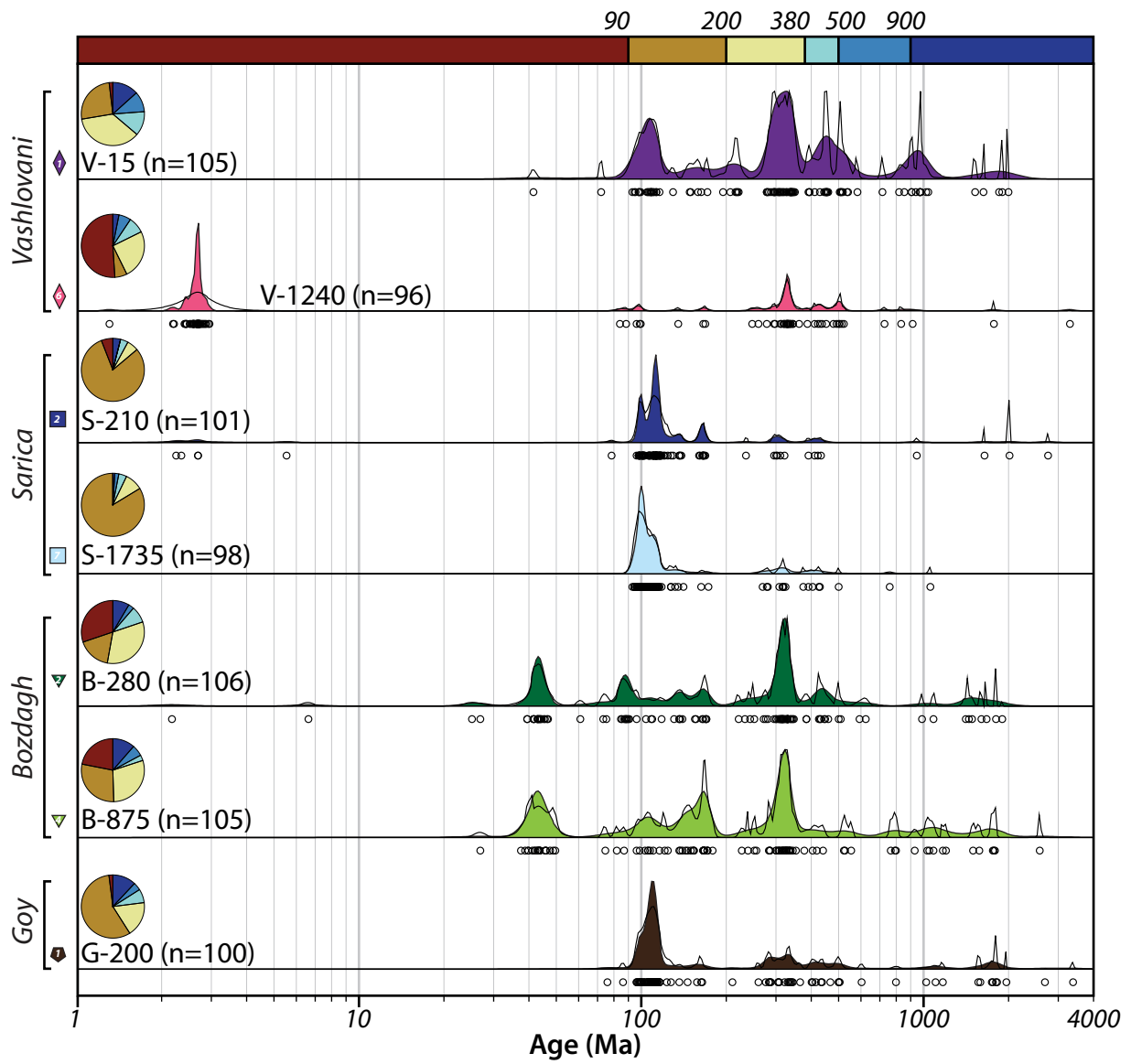
Sources

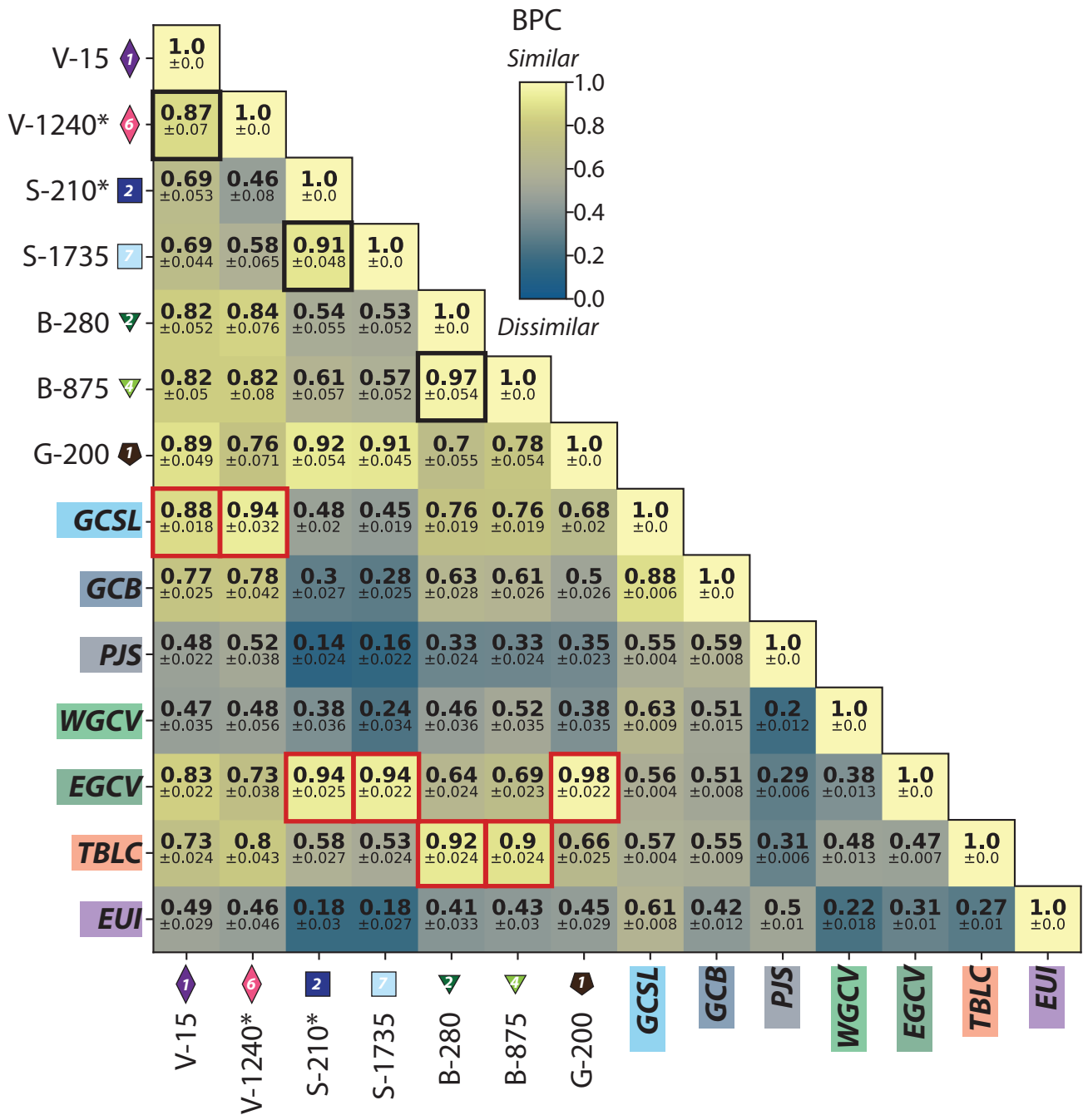
- + GC Rivers
- + LC Rivers
- × Vandam Bedrock
- + Dzirula River
- × Mid-Basin Kura River

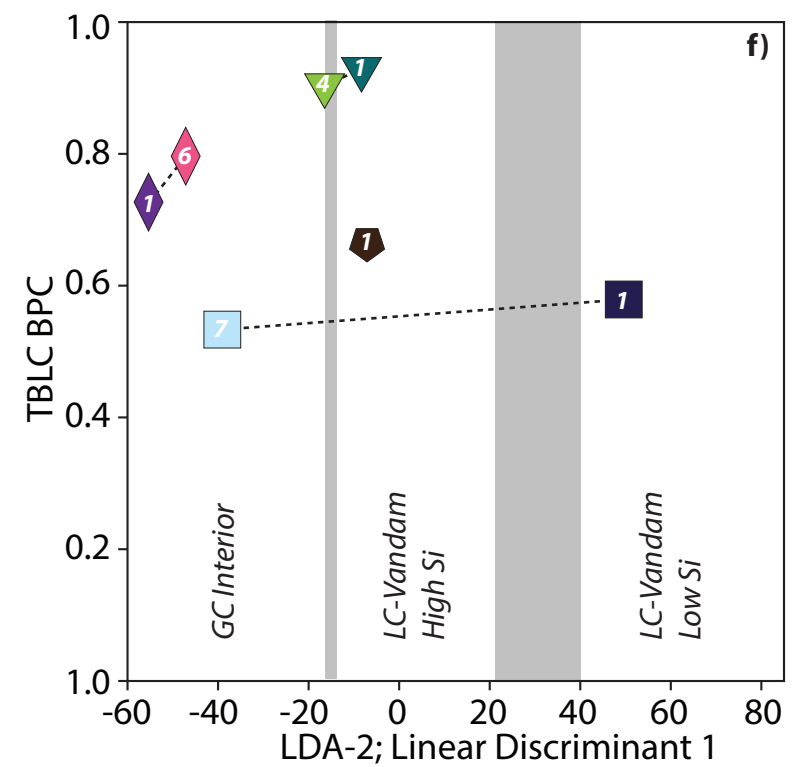
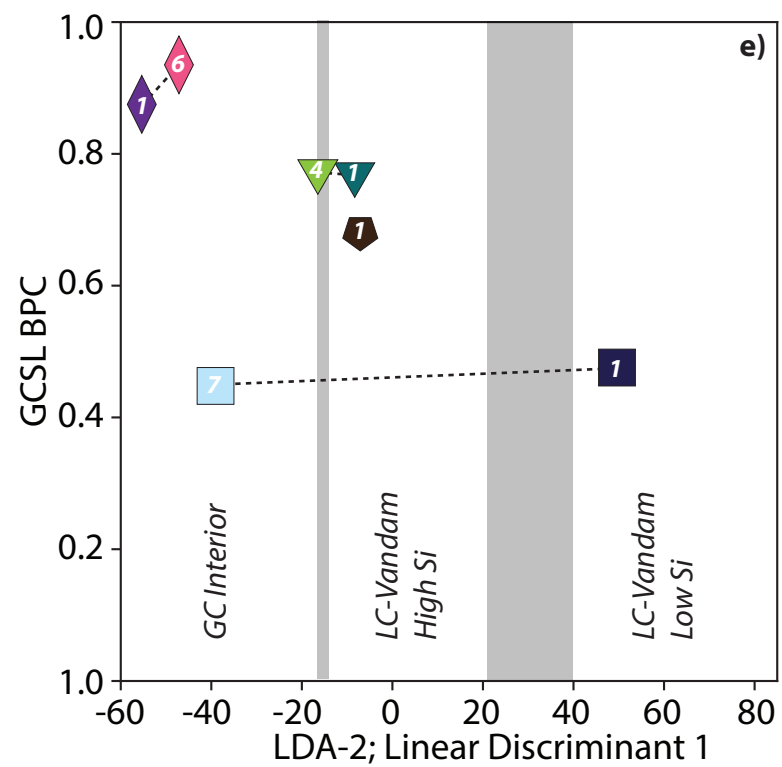
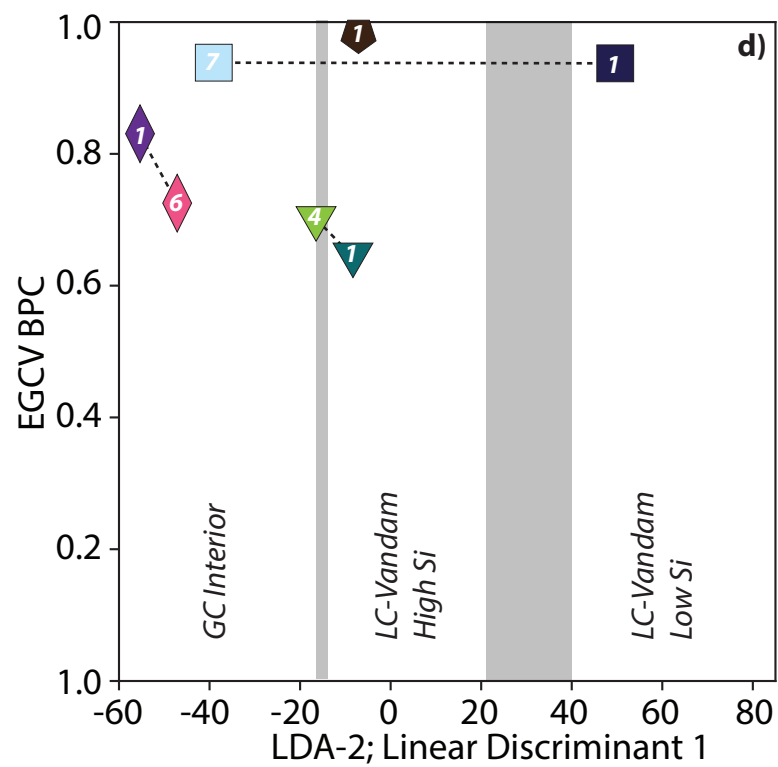
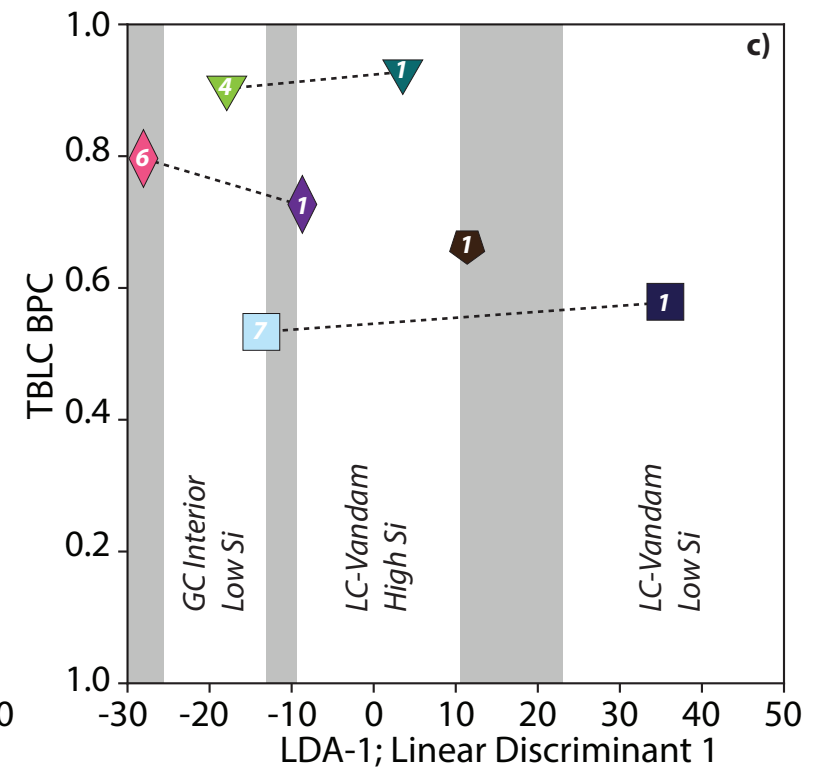
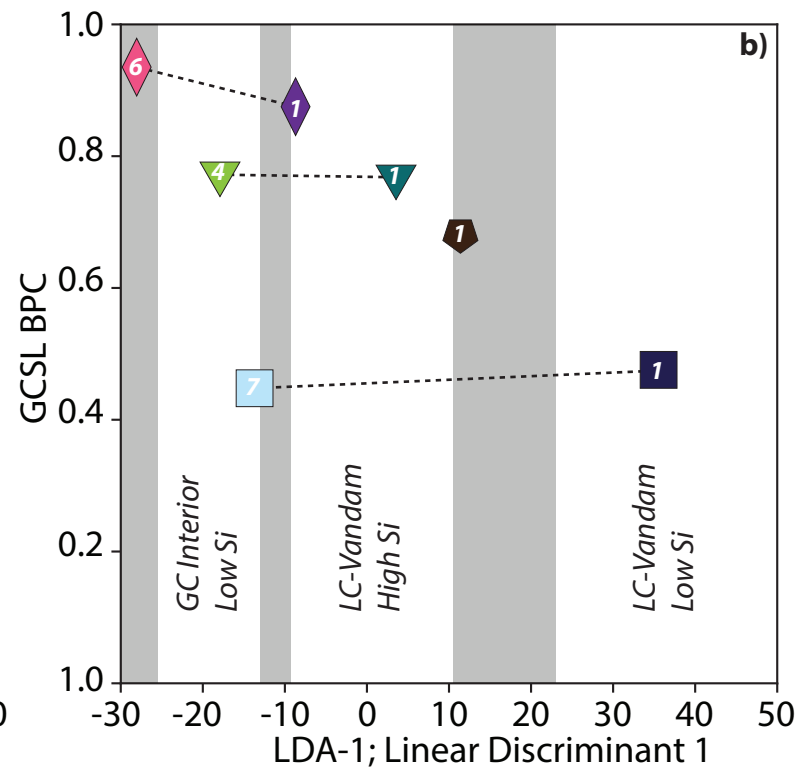
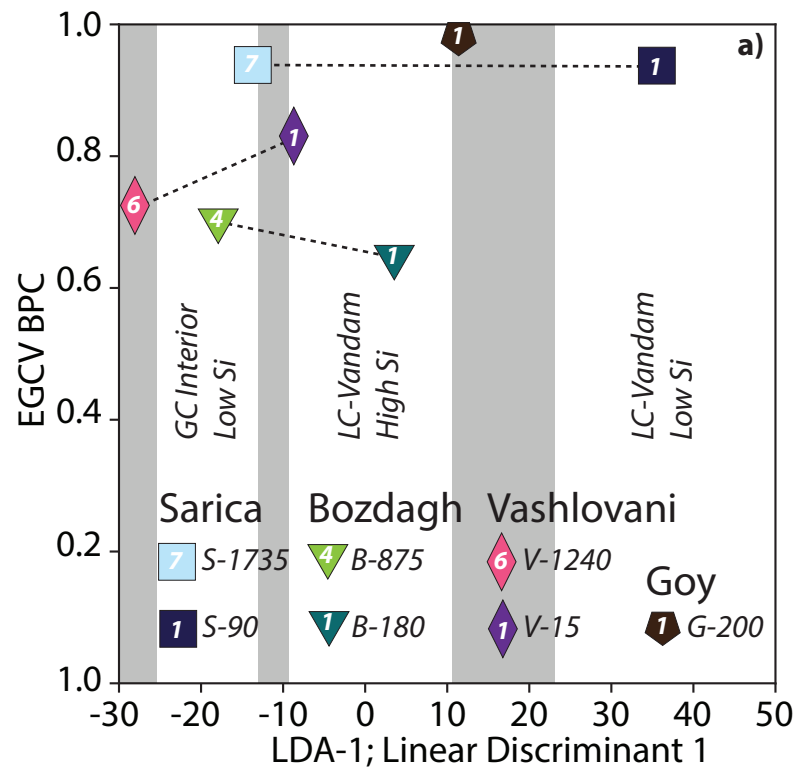




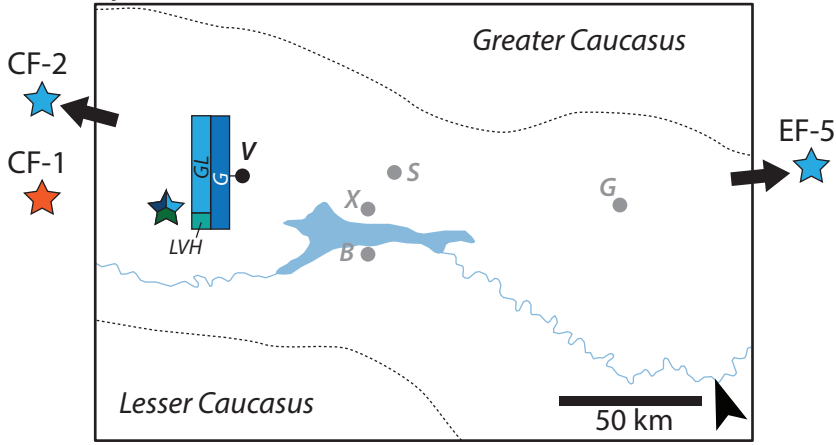




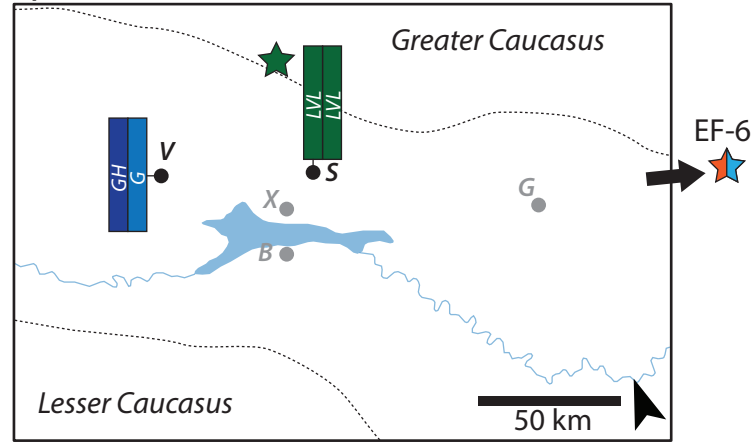




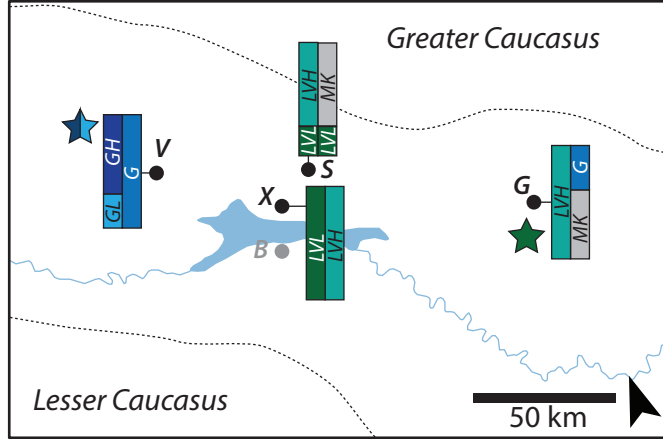
a) Meotian-Pontian



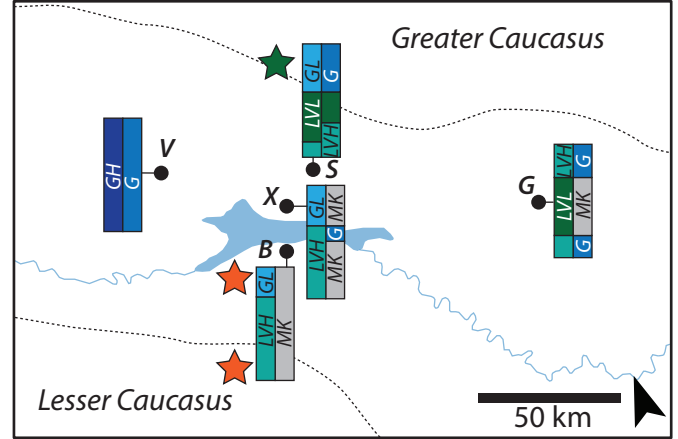
b) Productive Series



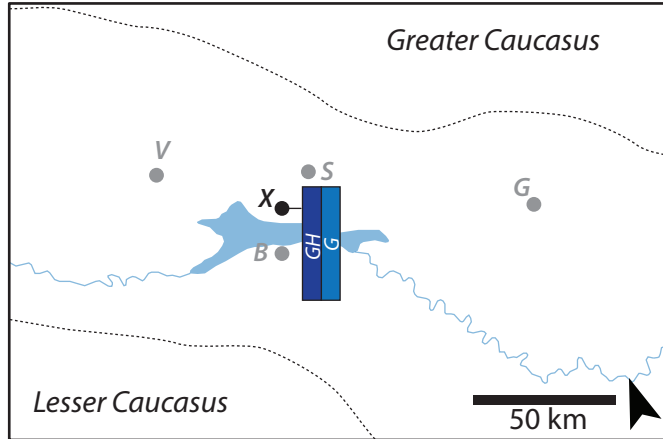
c) Akchagylian



d) Apsheronian



e) Bakunian

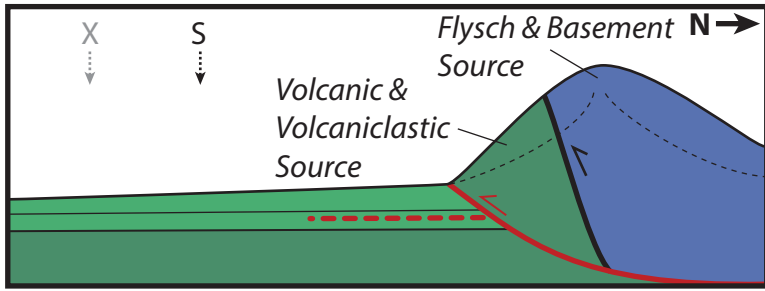


| LDA # | | |
|-------|-----|----------------------|
| 1 | 3 | |
| LVL | LVL | LC-Vandam Low Si |
| LVH | LVH | LC-Vandam High Si |
| GH | | GC Interior High Si |
| GL | | GC Interior Low Si |
| G | | GC Interior |
| | MK | Mid-Basin Kura River |

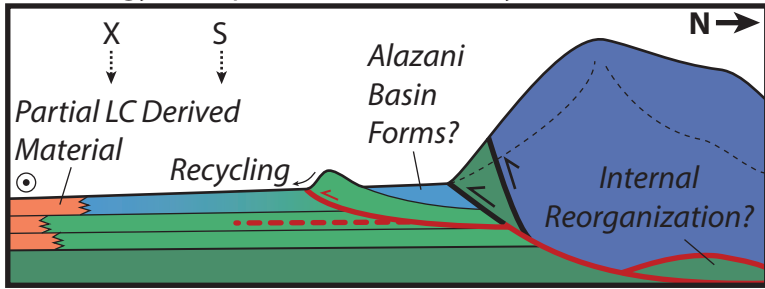
Dominant DZ Source

- ★ GC Siliciclastics
- ★ GC Basement
- ★ Eastern GC Volcaniclastics
- ★ Transcaucasus Basement and LC Arc

a) Productive Series



b) Akchagylian-Apsheronian Boundary



c) Apsheronian-Bakunian Boundary

